

University of Alberta

**Feasibility of Normalized Mutual Information Registration of CT and 1.5T MR
Images for Prostate Seed Implant Dosimetry**

by

Sandra Vidakovic



A thesis submitted to the Faculty of Graduate Studies and Research in partial
fulfillment of the requirements for the degree of Master of Science

in

Medical Physics

Department of Physics

Edmonton, Alberta

Fall 2006



Library and
Archives Canada

Bibliothèque et
Archives Canada

Published Heritage
Branch

Direction du
Patrimoine de l'édition

395 Wellington Street
Ottawa ON K1A 0N4
Canada

395, rue Wellington
Ottawa ON K1A 0N4
Canada

Your file Votre référence

ISBN: 978-0-494-22398-7

Our file Notre référence

ISBN: 978-0-494-22398-7

NOTICE:

The author has granted a non-exclusive license allowing Library and Archives Canada to reproduce, publish, archive, preserve, conserve, communicate to the public by telecommunication or on the Internet, loan, distribute and sell theses worldwide, for commercial or non-commercial purposes, in microform, paper, electronic and/or any other formats.

The author retains copyright ownership and moral rights in this thesis. Neither the thesis nor substantial extracts from it may be printed or otherwise reproduced without the author's permission.

AVIS:

L'auteur a accordé une licence non exclusive permettant à la Bibliothèque et Archives Canada de reproduire, publier, archiver, sauvegarder, conserver, transmettre au public par télécommunication ou par l'Internet, prêter, distribuer et vendre des thèses partout dans le monde, à des fins commerciales ou autres, sur support microforme, papier, électronique et/ou autres formats.

L'auteur conserve la propriété du droit d'auteur et des droits moraux qui protègent cette thèse. Ni la thèse ni des extraits substantiels de celle-ci ne doivent être imprimés ou autrement reproduits sans son autorisation.

In compliance with the Canadian Privacy Act some supporting forms may have been removed from this thesis.

Conformément à la loi canadienne sur la protection de la vie privée, quelques formulaires secondaires ont été enlevés de cette thèse.

While these forms may be included in the document page count, their removal does not represent any loss of content from the thesis.

Bien que ces formulaires aient inclus dans la pagination, il n'y aura aucun contenu manquant.


Canada

Abstract

The suitability of two algorithms for 3D rigid-body semi-automatic registration of post-implant CT and 1.5T MR prostate images was investigated by application to several simulated and three clinical datasets. The two algorithms tested were: normalized mutual information (NMI) and a novel hybrid approach that involved parallelization of straight lines fit to corresponding features running primarily in the Z direction in CT and MR volumes, and the subsequent application of NMI. The NMI algorithm alone was not able to reliably register either the simulated or clinical images. The hybrid algorithm registered the simulated images with an accuracy of <1mm (translations) and <1° (rotations), while 3D RMS errors for clinical volumes were <1.5mm provided no motion artifact was apparent. RMS errors were slightly lower than corresponding values obtained independently from registration with a landmark-based algorithm. The hybrid algorithm shows good potential for fast, semi-automatic registration of clinical CT and MR prostate images.

Acknowledgements

“Word Physics stems from the Greek word Φύσις, which means nature”. These words, deeply engraved in my memory, marked the beginnings of my eternal passion and love for this beautiful science. I remember, as if it were yesterday, my dearest teacher, the late Lazar Negic, dictating these words to a class of frightened 6-graders among which was a girl in whom teacher Lazo had a great faith. *“She will be a scientist...”* he would proclaim proudly smiling at me. I am so happy that his prophecy came true and I hope that he is smiling at me just as proudly, from the heavens above, right now. My beloved teacher Lazo, my guardian angel, you have a special place in my heart and my memory of you will never fade away.

Reflecting back, I see the faces of many other people that have been a part of this journey of mine. I am everything I am because they believed in me, loved me and supported me, in their own ways throughout my life and I would like to thank them all from the bottom of my heart.

My only son Stefan, my buddy, I cannot tell you how much I value your faith and pride in me. Your approval and respect motivate me evermore to reach further, do better, every day. I admire your exceptional perceptiveness, and your ability to say the right things at the right time. Your ingenious sense of humor has brightened many of my gloomy days, and I sincerely thank you for that. Watching you grow into a brilliant, genuine, and adorable young man is a priceless experience and I deeply cherish every moment of it. Mom’s unconditional love keeps growing with you, dude. Nenad, you’ve been my toughest critic, but also someone who shared all my ups and downs with me. I appreciate your perseverance and your (im)patience. One of these days, I will probably understand your strange ways of actually supporting me in what I do. I know you are a well-meaning companion and friend, and knowing me better than anyone else, you usually have the best advice for me; if only you gave it in a slightly softer way, and if only I were not so defiant to take it... But we’ll get it right, yet.

Mom, you are my heroine. Your endless optimism has taught me to persevere through anything to accomplish my goals. Thank you for your everlasting love and support, and for giving me the confidence to pursue my dreams. You are an infinite

fountain of inspiration and courage, and I love you with all my heart. My lovely sisters, Mira and Milijana, thank you for being my true friends that I could always count on and for sharing your lives with me. I feel truly blessed that we have that special, trustworthy relationship that is impossible to explain in words and can only be understood at a much deeper level. Your big sis loves you both, immensely. Of course, my immeasurable love goes to my adorable nieces Angela and Magdalena, whose picture on the background of my computer monitor brings joy to my heart and a smile to my face each and every day. My dearest aunty Smilja, I will never be able to thank you enough for everything you've done for me. Your goodness and generosity gave me courage to change the course of my life, and for that I will forever be in debt to you. There are no words that can convey how grateful I am to my dearest Father George and his wife Olga. Your selfless love and affection provided a safe haven for both Nenad and me when we needed it the most. Father, I will always remember your warm embrace – a secure cradle of unconditional love, encouragement and approval. Thank you for nurturing my personal and spiritual growth. I will forever cherish everything that you have taught me about what a true Christian should be. Also many thanks to Branka, Dragana, Slavko, Goran and Mike for babysitting and the care they took of Stefan while I was busy hitting my head off the wall trying to solve problems from Jackson, or other similarly impossible ones.

My undergraduate career in the Department of Physics at the University of Regina was ever so enjoyable thanks to a group of very enthusiastic and friendly people who made me feel welcome, respected and loved from day one. I will always have that *warm, fuzzy feeling* when I think about my dear SPARRO's: Edward, George, Zisis and Garth, and of course the real boss, Carol. Thank you for enriching my knowledge by generously sharing yours and for all the experience you provided to help me get polished into a true physicist. My world is a better place because of you...

Completion of my graduate work would not have been possible were it not for my supervisor, Dr. Ron Sloboda, to whom I would like to express my deepest gratitude for his guidance, help and support during the past two years. I truly admire his professionalism and graceful ways in which he redirected me onto the right path whenever I strayed away from it. Special thanks to Dr. Don Robinson, who generously extended his helping hand whenever I asked for it. Thank you for making

me feel comfortable and welcome to discuss many of my conundrums with you. Also, many thanks to Dr. Gino Fallone who works so diligently and tirelessly to provide an inspiring, professional and friendly environment for all of us to work in; I applaud your endeavors and accomplishments. Besides these three gentlemen I would also like to thank the fourth member of my graduate committee, Dr. Richard Marchand, for the time and effort they put in reviewing my thesis.

And of course, there are my fellow students and other staff at CCI that I would like to thank; I will start with the one that I feel most indebted to. Hans, I commend your expertise in image processing and cannot thank you enough for numerous in-depth advices and your contribution to my work. Also, thank you for sharing your life stories and offering useful life suggestions. Many thanks to Laura for her help with programming. Lesley thank you for sharing many happy, but also occasional tearful moments with me. Tara thanks for being a good listener and for your honest say-it-to-ones-face attitude. Amr thanks for your thoughtfulness and for beautiful presents from Egypt. Steven, thank you for being such a caring and kind-hearted person. I've never met anyone else quite as capable of using his wit and sense of humor to turn everything into a laughing matter. I will miss your ear-to-ear smile and your happy-camper personality. Ryan, you've been such a gentleman, yet a very cool guy. I always felt safe and comfortable in your company. Thank you for your instructive help and advice, and for all the laughter and sincerity. Alasdair thanks for being so considerate and encouraging. Many times, conversations with you helped me hang in there. In vain are your attempts to hide a truly sincere lad under that sarcastic mask; we all gotcha buddy!!! Thanks to Charlie, Stephen and Brad for being friendly and caring office mates/neighbours. I would also like to thank Heather Warkentin for being a patient, understanding and very helpful supervisor with my QA project. Many thanks go to machine shop guys Gary and Ken and of course to friendly and helpful secretaries Maureen, Debbi and Sarah for all their hard work. I am especially grateful to Cheryl Erickson who went out of her way, many, many times, to accommodate my requests; I truly appreciate your approachability and your effort.

I feel blessed to have known all of you and many other people that I did not mention here...

...and the journey continues...

To my son,

Stefan

Table of Contents

CHAPTER 1	1
1 INTRODUCTION	1
1.1 Cancer and Types of Treatment	1
1.2 Radiation Therapy	2
1.2.1 Teletherapy	3
1.2.2 Brachytherapy	4
1.2.2.1 Prostate Brachytherapy	5
1.2.2.3 High Dose Rate Prostate Implants	6
1.2.2.3 Low Dose Rate Prostate Implants	7
1.2.2.3.1 Post – Implant Dosimetry	9
1.3 Image Registration	11
1.3.1 Clinical Applications	11
1.3.2 Problem Classification	13
1.3.3 Image Registration Algorithms	15
1.3.4 Information Theory Techniques	17
1.3.4.1 Joint Entropy	18
1.3.4.2 Mutual Information	19
1.3.4.3 Normalized Mutual Information	20
1.4 Research Objective and Overview of Thesis	21
1.5 References	25
CHAPTER 2	28
2 IMAGE REGISTRATION FOR PROSTATE IMPLANTS	28
2.1 Prostate Implant Visualization	28
2.2 Landmark-Based Registration – Procrustes Algorithm	30
2.2.1 Procrustes Algorithm in VariSeed 7.1	32
2.3 Normalized Mutual Information Registration	32
2.3.1 Information Measures	33
2.3.2 NMI Algorithm as Implemented in Analyze 5.0	34
2.3.2.1 Preliminary Tests of NMI Algorithm – Phantom Studies	36
2.3.2.2 CT-CT Registration	36
2.3.2.3 CT-MR Registration	37
2.4 References	47

CHAPTER 3.....	48
3 POST-IMPLANT CT AND MR IMAGES USED FOR DOSIMETRIC EVALUATION.....	48
3.1 CT Image Volumes	48
3.1.1 Principles of CT Imaging	48
3.1.2 CT Image Acquisition	51
3.1.3 Image Features.....	52
3.1.4 Post-implant Dosimetry	53
3.2 MR Image Volumes	53
3.2.1 Principles of MR Imaging	53
3.2.2 MR Image Acquisition	56
3.2.3 Image Features.....	57
3.2.4 Post-implant Dosimetry	57
3.3 Image Distortion.....	58
3.3.1 Seed Phantom	58
3.3.2 Image Analysis and Results	59
3.3.3 Discussion.....	61
3.3.4 Conclusions	63
3.4 References	81
CHAPTER 4.....	83
4 REGISTRATION APPROACHES FOR CT - MR PROSTATE IMPLANT IMAGES	83
4.1 Introduction	83
4.2 Methods and Materials	85
4.2.1 Simulated Datasets	86
4.2.2 Clinical Datasets.....	86
4.2.3 Normalized Mutual Information (NMI) Algorithm.....	87
4.2.4 Feature Lines Method	87
4.2.5 Registration of Simulated Datasets	90
4.2.6 Feature Lines Method Applied to Simulated Datasets...	91
4.2.7 Registration of Clinical Datasets Using a Novel Hybrid Algorithm.....	92
4.2.8 Registration Accuracy	94
4.3 Results.....	95
4.3.1 Simulated Datasets	95
4.3.2 Assessment of Feature Lines Method with Simulated Datasets.....	96
4.3.3 Registration of Clinical Datasets	97
4.3.4 Error Analysis.....	98
4.4 Discussion	98
4.4.1 Simulated Datasets	99
4.4.2 Clinical Volumes.....	100

4.5	Conclusion.....	103
4.6	References	118
CHAPTER 5.....		120
5	SUMMARY AND FUTURE DIRECTIONS.....	120
5.1	Summary	120
5.2	Future Directions	123
5.3	References	125
BIBLIOGRAPHY.....		126

List of Tables

Table 1.1	Physical properties of radionuclides used brachytherapy.....	23
Table 3.1	In-plane distances between adjacent seeds in the CT image volume.....	65
Table 3.2	Distances between collinear seeds in the two seed planes in the CT image volume.....	66
Table 3.3	In-plane distances between adjacent seeds in the T2-weighted MR image volume.....	67
Table 3.4	Distances between collinear seeds in the two seed planes in the T2-weighted MR image volume.....	68
Table 3.5	In-plane distances between adjacent seeds in the B-FFE MR image volume.....	69
Table 3.6	Distances between collinear seeds in the two seed planes in the B-FFE MR image volume.....	70
Table 3.7	Sup-inf (Z direction) distances between seeds in ribbons (slice volume effects absent) measured in the B-FFE MR image volume.....	71
Table 3.8	Distance between the Lucite plates holding the seed ribbons measured in the B-FFE MR image volume.....	72
Table 4.1	Simulated implant image data – structure intensities.....	105
Table 4.2	Results of 6 DOF registration of simulated datasets with and without restrictions on search parameters. Restrictions placed on X and Y translation ranges and X, Y, and Z rotation ranges are described in Section 4.2.5.....	106

Table 4.3	Results of 4 DOF registration of simulated datasets with and without Poisson noise. X and Y rotations were not allowed and restrictions were placed on X and Y translation and Z rotation search ranges as described in Section 4.2.5.....	106
Table 4.4	Comparison of applied rotations with those calculated by the feature lines method for simulated datasets: a) T2-weighted MR dataset; b) CT dataset.....	107
Table 4.5	Relative rotation angles for three feature line pairs in the clinical image volumes for: a) patient A; b) patient B; and c) patient C.....	108
Table 4.6	RMS distances between X, Y and Z coordinates of corresponding points (seed/seed voids) in registered clinical CT and MR volumes: a) for patient A; b) for patient B; and c) for patient C.....	109
Table 4.7	Comparison of RMS distances calculated for clinical volumes registered by the hybrid and Procrustes algorithms	110

List of Figures

Figure 1.1	Transperineal ultrasound-guided permanent implant technique.....	24
Figure 2.1	a) Axial CT image of permanent prostate implant; b) Axial T2-weighted MR image of implanted prostate.....	39
Figure 2.2	Left-handed Cartesian coordinate system used in this work.....	40
Figure 2.3	Information content H of a binary image consisting of foreground (f) and background (b) with probabilities $p(f)$ and $p(b)$, respectively, where $p(f) = 1 - p(b)$	41
Figure 2.4	The information content in a combined image: a) is higher with poorly aligned base and match images; b) is minimized with well aligned base and match images.....	42
Figure 2.5	A photograph of the water-filled cylindrical container used to hold different phantom inserts utilized in our experiments.....	43
Figure 2.6	A photograph showing an ensemble of inserts made of different density materials used in our phantom studies.....	44
Figure 2.7	3D CT-CT registration of images of a water phantom containing inserts: a) reference volume; b) displaced volume; c) unrestricted registration; d) registration after thresholding; e) registered volumes displayed using a window highlighting low intensities to show the CT couch.....	45
Figure 2.8	CT-MR registration of the water phantom: a) CT - reference image; b) MR image positioned similarly to the reference image, with a registration VOI outlined; c) correctly registered volumes.....	46

Figure 3.1	Typical spin-echo MR imaging timing diagram, illustrating the relationship between spin flip pulses, the FID signal, and the imaging gradients.....	73
Figure 3.2	CT slice of a prostate implant near the base of the prostate gland. Note the difference in intensities of structures imaged: bones and implanted seeds appear brightest, air in the rectum darkest.....	74
Figure 3.3	CT image volume of a prostate implant: a) caudal slice, b) mid-gland slice, c) cranial slice.....	74
Figure 3.4	a) Axial slice from T2-weighted MR image volume depicting post-implant prostate near mid-gland; b) corresponding axial slice from B-FFE MR image volume.....	75
Figure 3.5	A photograph of the phantom insert consisting of two collinear seed grids separated by ~50 mm.....	76
Figure 3.6	a) Sketch of the water-filled phantom used for spatial distortion measurements (note the orientation of the seed phantom insert); b) Grid illustrating seed locations in the two planes.....	77
Figure 3.7	Graphical representation of the algorithm used for finding centroid locations of seeds in the grid inserted into the water phantom.....	78
Figure 3.8	Photograph of a seed ribbon insert consisting of two parallel plastic tubes, containing evenly spaced seeds, used for assessing the partial volume effect along the MR scanning axis.....	79
Figure 3.9	Sketch of the cylindrical container containing the seed ribbon insert immersed in the water background (note the orientation of the seeds with respect to the scanner axis).....	80

Figure 4.1	Volume rendering of a simulated CT prostate implant dataset.....	111
Figure 4.2	a) Axial slice of T2-weighted MR volume set of post-implant prostate; b) corresponding axial slice of B-FFE MR volume set	112
Figure 4.3	Orientation of a feature line in 3D space: a) rotation of a needle track about the Y – axis; b) θ_y , angle of rotation in the X – Z plane.....	113
Figure 4.4	Examples of linear fits to simulated CT and MR image volume feature coordinates.....	114
Figure 4.5	Sample plots used in graphical analysis for determination of θ_x and θ_y for a pair of feature lines in the set of clinical image volumes for patient A.....	115
Figure 4.6	Sample plots used in graphical analysis for determination of θ_x and θ_y for a pair of feature lines in the set of clinical image volumes for patient B.....	116
Figure 4.7	Clinical B-FFE axial MR slices of the prostate near mid-gland illustrating the dependence of image quality on the presence of motion artifact: a) no noticeable motion artifact present – image features appear sharp; b) considerable amount of motion artifact present – image features appear blurred.....	117

List of Symbols

B_0	Applied magnetic field strength
C_i	Curie
c_i	Spatial coordinates of point i
^{60}Co	Cobalt-60
$D_{i,\text{plane}}$	2D distance between a seed and the center of the seed grid
$D_{i,\text{vol}}$	3D distance between a seed and 3D centroid of the volume
D_x, D_y	In plane distances between neighbouring seeds along x and y axis, respectively
D_{90}	Dose delivered to 90% of the target volume
Gy	Grey
H	Shannon-Wiener entropy
$H(A)$	Marginal entropy for image A
$H(A,B)$	Joint entropy for images A and B
HU	Hounsfield units (measuring pixel intensities in CT images)
^{192}Ir	Iridium-192
^{125}I	Iodine-125
K	Scaling factor equal to 1000 HU
MeV	Mega electron-Volt
N	Number of transmitted photons
$\text{NMI}(A,B)$	Normalized mutual information measure for images A and B
N_0	Number of incident photons
p_i	Probability of occurrence of value i
$p_A^{\tau}(a)$	Marginal probability distribution function for image A
$p_{A,B}^{\tau}(a,b)$	Joint probability distribution function for images A and B
^{103}Pd	Palladium-103
$R_i(\theta_i)$	Rotation matrix applying a rotation θ_i about axis i
s_i	Scaling factor along the i -axis

T	Tesla (unit for magnetic field strength)
TE	MR RF pulse echo time
TR	MR RF pulse repetition time
t_i	Translation along the i-axis
$T(\vec{r})$	Transformation matrix applied to a point described by a vector \vec{r}
T1, T2, T2*	Tissue specific relaxation times
V_{100}	Volume receiving 100% of the prescribed dose
$\{x_i\}$	Point set
α, β, γ	Angles of rotation around x, y and z axis, respectively
δc_i	Uncertainty in spatial coordinates of point i
Δ_{\max}	Maximum difference between measured and physical distances
γ	Gyromagnetic ratio
μ	Linear attenuation coefficient
θ_i	Angle of rotation about i-axis
ω_0	Larmor frequency

List of Abbreviations

AAPM	American Association of Physicists in Medicine
ABS	American Brachytherapy Society
B-FFE	Balanced Fast Field Echo
CT	Computed Tomography
DOF	Degrees of Freedom
EPID	Electronic Portal Imaging Device
FOV	Field of View
FRE	Fiducial Registration Error
HDR	High Dose Rate
HI-ART	Highly Integrated Adaptive Radiation Therapy
HU	Hounsfield Units
ICRU	International Commission on Radiation Units and Measurements
IMRT	Intensity Modulated Radiation Therapy
LDR	Low Dose Rate
MRI	Magnetic Resonance Imaging
NMI	Normalized Mutual Information
OAR	Organs at Risk
PDF	Probability Distribution Function
PSA	Prostate Specific Antigen
ROI	Region of Interest
RMS	Root Mean Square
TG	Task Group
TPS	Treatment Planning System
US	Ultra Sound
VOI	Volume of Interest
1D	One Dimensional
2D	Two Dimensional
3D	Three Dimensional

CHAPTER 1

1 INTRODUCTION

1.1 Cancer and Types of Treatment

Normally functioning body cells have a well-defined life cycle during which cells form, reproduce and stop reproducing in an orderly fashion. The development of cancer is driven by gene damage that causes uncontrolled proliferation of cells hence disrupting the balance in rates of new cell growth and old cell death. Abnormally growing cells form tumors that can be either benign (non-cancerous) or malignant (cancerous) which may invade and destroy surrounding normal tissues. In addition, the cancerous cells may break away from the original site and spread to other organs by traveling through the bloodstream or lymphatic system. Often these cells continue to divide forming a new tumor referred to as a metastasis. The goal of cancer therapy is to remove or destroy all the cancerous cells in a patient's body, or to prevent their proliferation and hence the further spread of disease.

There are several different treatment options available to cancer patients, which include:

1. Surgery: the most direct removal of a solid tumor from a specific area.
2. Chemotherapy: a treatment that uses anticancer drugs to destroy cancer cells or stop their proliferation. The drugs, taken orally or by injection directly into a vein or muscle, enter the bloodstream and can reach cancer cells throughout the body. Often this is the only method of treating disseminated or widespread disease.

3. Biotherapy or Immunotherapy: a treatment that uses the patient's immune system to fight disease by stimulating the body's natural defenses with substances made either in the body or in a laboratory.
4. Radiation therapy: a cancer treatment that utilizes high-energy x-rays or other types of ionizing radiation to destroy cancer cells or damage them enough to prevent their proliferation.
5. Hormone therapy: a treatment where drugs, surgery, or radiation are used to reduce the production of hormones or block their action. This in turn kills cancer cells or slows their growth.

The most effective treatment or combination of treatments for each individual patient is chosen depending on the type of cancer, the extent of the disease, the treatment side effects, and the quality of life afterwards.

1.2 Radiation Therapy

Radiation therapy, also called radiotherapy, can be used to treat various types of cancers in almost any part of the body. In radiation therapy the disease is treated with penetrating, highly energetic ionizing particles or waves, such as x-rays, γ -rays, α -particles and β -particles. Although radiation therapy can be used in combination with other cancer treatments, for many cancer patients it is the only form of therapy required. Some of the cancers commonly treated with radiotherapy are: non-Hodgkin's lymphomas, early stage Hodgkin's disease, some head and neck tumors, and localized cancers of the breast, lung, prostate, cervix, bladder, testes, thyroid and brain. Radiation therapy is a local treatment that kills and damages cancer cells only in the irradiated part of the body. Inevitably, however, some of the surrounding normal cells are also affected but, unlike cancer cells, many of them are able to successfully recover from damaging radiation effects. The goal of radiotherapy is to successfully treat the disease with minimal damage to normal cells. To accomplish this goal, various techniques such as shielding,

limiting doses received by nearby organs at risk, and spreading the dose delivery over an extended period of time, are used to protect normal tissue. Radiotherapy can be implemented at long or short distances and is accordingly divided into teletherapy (“tele” – Greek for “far”) using external beams, and brachytherapy (“brachios” – Greek for “short”) using sealed sources.

1.2.1 Teletherapy

More commonly known as external beam radiation therapy, teletherapy is a form of radiotherapy in which high-energy beams of ionizing radiation, coming from specialized therapy machines, are directed at the treatment volume within the patient's body. Photons, γ -rays, electrons, protons, neutrons, and pions have all be used in external beam therapy. However, the production of protons, neutrons, and pions requires expensive subatomic physics laboratory set-up, and hence these particles are not widely available for cancer treatment. On the other hand, photon and electron beams are produced by linear accelerators (linacs), while γ -rays are obtained from ^{60}Co units. These treatment units do not require a great deal of space, are relatively inexpensive and easy to operate, and as such they are commonly found in cancer treatment centers throughout the world. Megavoltage electron beams are used to treat superficial tumors, while photon beams of various energies are used for treatment of deeply seated tumors. The more energetic the photon beam, the deeper it can penetrate inside the body and therefore, photon beam energy is chosen according to the depth of the tumor site. Imaging modalities, such as computed tomography (CT) and magnetic resonance imaging (MRI), are used to guide delineation of a tumor volume in the treatment planning process.

There are several techniques that can be used to deliver a desired dose of radiation to the tumor while minimizing the dose to normal tissue. In

conventional therapy, static radiation beams directed at the tumor volume are shaped with collimators built into the treatment unit and secondary custom beam blocks, while beam parameters, such as beam weight, direction, shape, etc. are adjusted manually [Van Dyk, 1999]. Alternatively, in conformal therapy, the high dose volume is shaped using dynamic wedges and multi-leaf collimators that are controlled remotely by computer. Two types of conformal therapy of current interest are:

- Intensity Modulated Radiation Therapy (IMRT): where advanced computer-based treatment planning methods and multi-leaf collimators on conventional linear accelerators enable more precise dose distribution shaping in three dimensions via spatial intensity modulation of the radiation beams directed at the tumor.
- TomoTherapy Highly Integrated Adaptive Radiation Therapy (HI-ART): which delivers an integrated form of IMRT that combines treatment planning, patient positioning, and radiation dose delivery from a continuously rotating specialized linac gantry into one sophisticated system.

1.2.2 Brachytherapy

As its name suggests, brachytherapy is a type of radiation therapy where cancer treatment is done with sealed radioactive sources placed in the immediate vicinity of, or within, cancerous tissue. Source placement can be tailored so that a desired dose is delivered to a tumor while dose to surrounding healthy tissue is minimized. Depending on the method of placement with respect to body tissues, the radioactive source configuration can be categorized as a surface application, interstitial implant, or intracavitary insertion. The source placement can be either permanent – for some low dose rate (LDR) brachytherapy, or temporary – for both LDR and high dose rate (HDR) brachytherapy.

Although many solid, soft tissue cancers can be treated with brachytherapy, this type of treatment is most suitable for treating highly localized disease at easily accessible sites, such as prostate cancer, cancers of the pelvis (cervical, ovarian, vaginal, rectal), and head and neck cancers. Brachytherapy can be used as either primary treatment or as adjuvant treatment following surgical removal of the tumor or external beam therapy. General attributes of brachytherapy are that it is typically less invasive than surgery, and in many cases has fewer side effects than either surgery or external beam therapy.

1.2.2.1 Prostate Brachytherapy

Prostate cancer has the highest incidence rate and second highest mortality rate of any cancer in North American men [Chan, *et al.*, 2004]. Prior to the development of prostate-specific antigen (PSA) testing, prostate tumors were usually discovered in their advanced stages, which limited the likelihood of treating this disease successfully. The introduction of PSA testing has allowed diagnosis at an earlier stage, giving patients more treatment options and a better chance for a positive treatment outcome. An effective treatment for localized prostate cancer is brachytherapy, in which radioactive sources are implanted directly into the prostate gland. This method of treatment ensures a high dose concentration within the tumor while keeping irradiation of the normal tissues at risk to a minimum. Brachytherapy side effects are generally milder and easier to manage than side effects of other therapies [Khan, 2003]. In addition, the implantation procedure is performed on an outpatient basis and recovery time is typically a few days. Such benefits make brachytherapy a treatment of choice for many prostate cancer patients. The type of brachytherapy used for treatment is frequently chosen according to the stage of disease. If disease is found at an early stage, it is usually treated with

a LDR permanent implant, while HDR brachytherapy is mostly used in combination with external beam therapy to treat more advanced disease [Lee, *et al.*, 2003].

1.2.2.3 High Dose Rate Prostate Implants

HDR brachytherapy for prostate cancer can be used either as an adjuvant treatment to external beam radiotherapy for patients with advanced prostate cancer, or as the only treatment method (monotherapy) for early stage disease. According to ICRU Report 38 [ICRU, 1985] HDR is classified as irradiation at a dose rate of 20 cGy/min or higher, which is at least 10x higher than LDR. As such, HDR brachytherapy is performed in adequately shielded hospital rooms (vaults) using remote afterloading devices, which ensures minimal exposure risk to medical personnel and the public.

HDR prostate brachytherapy is performed using temporary implants in which a computer-controlled afterloader moves a single radioactive source in predetermined steps within hollow guide needles. The needles are previously inserted into the prostate gland transperineally under the guidance of a transrectal US probe. The source most commonly used in HDR brachytherapy is Iridium-192. Because of its high specific activity, ^{192}Ir is suitable for manufacturing ~10 Ci sources occupying an active volume of ~1 mm³, which makes it ideal for HDR interstitial brachytherapy. A ^{192}Ir line source of dimensions between 0.3 and 0.6 mm in diameter and 3.5 to 5 mm in length, welded to the end of a flexible drive cable, is housed in a shielded safe inside the remote afterloading HDR unit [Khan, 2003]. During the treatment the guide needles are connected to flexible transfer tubes that in turn are connected to the HDR unit, allowing the radioactive source to move from the afterloader into the needles and back again. The length of time that the radiation source spends in each of the needles, as well as the length of time

that it dwells at each position within a needle, is controlled by a computer and specified according to a treatment plan. After the prescribed dose is delivered, the source is pulled back into its housing.

HDR treatment is delivered in a few fractions each lasting several minutes. The number of treatment fractions that a patient receives, as well as the time between fractions, depends on whether HDR is used as monotherapy or as adjuvant therapy. In either case a patient must stay hospitalized until the whole treatment is completed to avoid repetitive needle insertion. One of the advantages of HDR brachytherapy is that the uniformity of the dose distribution is more easily controllable during the treatment, as planning is done after needle insertion and so dwell positions and dwell times can be modified to minimize inhomogeneities in dose distribution.

1.2.2.3 Low Dose Rate Prostate Implants

Treatment of early stage prostate cancer with LDR brachytherapy is achieved with permanent implants placed within the prostate gland, with a prescribed dose of 145 Gy [Yu *et al.*, 1999] delivered at an initial dose rate ranging from 0.5 to 2.0 cGy/min. Radioactive sources are commercially available in the form of small cylindrical seeds 4.5 mm long and 0.8 mm in diameter [Khan, 2003]. These seeds consist of radioisotope and substrate encapsulated in titanium [Heintz, *et al.*, 2001]. Radioisotopes most commonly used for interstitial LDR brachytherapy are ^{125}I and ^{103}Pd . Both radioisotopes emit low energy photons and have relatively short half-lives, see Table 1.1. These sources are left in the patient permanently and deliver the radiation treatment continuously, with 97% of the dose deposited within a period of 5 half-lives. Low energy radiation emitted by these sources is absorbed locally and poses little risk to other people or surrounding organs within the patient [Khan, 2003].

Prostate implants were first performed in the early 1970s at Memorial – Sloan Kettering Cancer Center [Khan, 2003]. The implantation procedure involved a major surgery where needles loaded with seeds were passed through an incision made in the abdomen and placed into the gland guided only by touch. This technique often resulted in an inadequate dose distribution due to inhomogeneous seed placement, and the treatment results were often disappointing.

In the 1980s the retropubic technique was replaced with a modern transperineal implantation procedure illustrated in Figure 1.1, which utilizes a transrectal ultrasound (US) probe and perineal template for guiding seed placement [Khan, 2003]. The transperineal implant procedure is less invasive than the retropubic procedure, and simultaneous visualization of the prostate and the needle being inserted into it allows for more accurate seed placement, which consequently has led to better treatment outcomes [Peschel, *et al.*, 2003, Ragde, *et al.*, 2000]. A complete implantation procedure consists of four essential steps:

- Volume study: where the patient is placed in the lithotomy position and transverse images of the prostate are acquired in increments of 5 mm (from base to apex) using a transrectal US probe. An oncologist determines the location of the prostate gland on all images by outlining the prostate contour. A grid corresponding to the implant template coordinates is superimposed on each image.
- Treatment planning: where the volume study is transferred to a treatment planning system (TPS) and a customized plan is generated for the patient. The TPS allows the user to adjust seed strength and modify seed placement to achieve optimal isodose coverage of the planning target volume (PTV), which consists of the prostate plus a margin. Based on an approved computer plan, a worksheet is prepared specifying the number of needles, seeds in each needle, and corresponding template coordinates [Khan, 2003].

- Seed implantation: where the patient is put under either general or spinal anesthesia in the lithotomy position and needles preloaded with seeds and spacers are inserted through the patient's perineum and into the prostate gland. The template coordinates determined by the treatment plan are used to guide needle placement, which is monitored with US. Once a needle has been positioned in a planned location, it is slowly pulled back while holding the needle stylette fixed in place, thereby depositing seeds along the path of needle retraction. The distribution of implanted seeds is assessed through sequential viewing of the US images.
- Post-implant evaluation: where CT images of the pelvis, typically acquired about one month after the implant, are used for post-implant dosimetry to determine the implant quality. Considering that the seeds may not be in their intended positions, this evaluation is necessary to ensure that the target volume is receiving an adequate dose.

Variations on this common implantation procedure include: obtaining the volume study data by rotation of the US probe configured for imaging in the longitudinal plane, using a Mick applicator [Kunos, *et al.*, 2004] instead of preloaded needles to deposit the seeds, and performing the post-implant dosimetry on the day of the implant. In some centers the volume study, treatment plan and implantation are done within the span of a few hours in a process referred to as intra-operative planning [Stone, *et al.*, 2003].

1.2.2.3.1 Post – Implant Dosimetry

Post-implant dosimetric evaluation is the standard contemporary method for assessing permanent implant quality and determining the dose received by the prostate and organs at risk over the course of the treatment. Due to post-implant edema and seed placement errors intrinsic to the

permanent implant procedure, the post-implant dose distribution may be significantly different from that planned prior to the implant. Radiation dose coverage, as assessed using post-implant dosimetry, is strongly correlated with treatment outcome and hence, it is important that the dose distribution is assessed accurately [Yu *et al.*, 1999]. Information obtained from post-implant dosimetry is instructive for assessing the need for supplemental therapy, improving implant techniques, and optimizing patient care. In addition, post-implant dosimetry data provides a means for comparison of clinical trials performed at different institutions.

Historically, post-implant dosimetry was performed using various techniques that utilized conventional radiographic images. However, these techniques are not very reliable because neither the prostate nor the critical structures can be visualized on the radiographs, and so the minimum peripheral dose is nearly always overestimated. In addition, due to the lack of a 3-D spatial relationship between the target and implant volumes, dose-volume information for the prostate and surrounding normal tissues is not available [Roy, *et al.*, 1993].

To address these problems, CT-based 3D post-implant dosimetry utilizing cross-sectional image data was first recommended by the American Endocurietherapy Society in 1991 and soon afterwards applied to prostate implants by Roy *et al.*, at Memorial Sloan-Kettering Cancer Center in 1993 [Roy, *et al.*, 1993]. This dosimetric technique allows more precise localization of seeds with respect to the target volume and therefore the assessment of dose distribution is more reliable. The American Brachytherapy Society (ABS) currently recommends that post-implant dosimetric analysis utilizing CT images be mandatory for all patients undergoing transperineal permanent prostate brachytherapy [Nag, *et al.*, 2000]. An important limitation of this method, however, is poor visualization of the prostate boundary on CT images and consequently, it has been reported that CT images overestimate the prostate size [Dubois, *et al.*, 1998]. This overestimation leads to inaccurate

measurement of clinically significant dosimetric indices such as D90 (the minimum dose received by 90% of the prostate gland) and V100 (the volume of prostate gland receiving at least 100% of the prescribed dose), or equivalently to inaccurate determination of the dose delivered to the target and to the organs at risk (OAR). As it allows better appreciation of soft tissue anatomy and hence the prostate contour, MR imaging has been considered as a tool for performing post-implant dosimetry [Dubois *et al.*, 1997]. However, the visibility of the radioactive seeds in MR images is insufficient to allow its use as the only means of evaluating the treatment. Various approaches may be used to combine CT and MR imaging techniques to optimize the information available for the post-implant analysis [Nag, *et al.*, 2000].

1.3 Image Registration

The process of finding a transformation that establishes the spatial correspondence between two images or between an image and physical space is referred to as image registration [Hajnal, *et al.*, 2001]. Image registration is a two-step process:

1. Spatial transformation: where data sets are brought into accurate spatial alignment.
2. Fusion: integration of the data for the purpose contemplated.

The goal of image registration is to achieve the proper integration of complementary information contained in different data sets to yield additional useful information not available from the individual sets alone.

1.3.1 Clinical Applications

Image registration is playing an increasingly important role in medical imaging. As the availability and capability of different imaging modalities

increases, so does the application of image registration in a variety of medical circumstances in both biomedical research and healthcare. Image registration has become especially useful in the clinical environment where it is used to:

- combine information from images obtained by either the same or different imaging modalities;
- relate a patient's anatomy to computer models or a standardized atlas;
- help in the delineation of anatomical and pathological features;
- monitor changes in function, size and shape of various structures over time; and
- guide therapeutic procedures.

Specific applications of image registration in clinical medicine include [Maintz & Viergever, 1998, Hajnal, *et al.*, 2001]:

- Treatment planning and verification;
- Motion correction during treatment;
- Monitoring growth or regression of disease;
- Dynamic contrast-enhanced angiography;
- Monitoring patient growth and development;
- Image-guided surgical procedures;
- Follow-up studies.

As an integral part of post-implant dosimetry for permanent prostate implants, co-registration of corresponding CT and MR images could be used to determine the spatial relationship between the radioactive seeds and the target volume more accurately than is currently possible using CT alone. This is expected to improve the accuracy in measuring clinically significant indices useful for outcome assessment, such as D90 and V100.

1.3.2 Problem Classification

Image registration problems can be categorized according to nine basic criteria, which are further subdivided into different levels [Maintz, *et al.*, 1998]. Specifically, classification is based on:

1. Dimensionality

- a. Spatial dimensions only: where two images of either the same or different spatial dimensions are registered and no time component is involved.
- b. Time series with spatial dimensions: where registered images are acquired over long or short time intervals for the purpose of monitoring growth, healing, drug effects, etc.

2. Nature of registration basis

- a. Extrinsic: where registration is based on artificial objects placed on the patient.
- b. Intrinsic: method that relies on image information originating from the patient only.
- c. Non-image based: where the basis for registration is the coordinate systems of the scanners involved, which have been previously related to each other.

3. Nature of transformation

- a. Rigid: where the relative distances between spatial points are preserved, the transformation matrix consists of translations and rotations only; no distortions are involved and the actual shape and size of the image remain the same.
- b. Affine: where parallelism and proportions are preserved, but angles and lengths may not be.
- c. Projective: where linearity is preserved but parallelism is not.

- d. Non-linear: where linearity is not preserved, straight lines map into curves and the image is deformed.

4. Domain of transformation

- a. Local: where different transformations are defined for different subsections of the image.
- b. Global: where the same transformation is applied to the entire image.

5. Interaction

- a. Interactive: where the user, assisted by software, performs the registration manually.
- b. Semi-automatic: where the user either initializes and/or steers the registration process.
- c. Automatic: where registration is done automatically by the software and required user interaction is minimal.

6. Optimization procedure

- a. Parameters computed: where transformation parameters are computed directly from the available data.
- b. Parameters searched: where optimization of some mathematical function is used to determine the parameters.

7. Modalities involved

- a. Monomodal: where registered images are acquired with a single imaging modality.
- b. Multimodal: where registered images originate from different imaging modalities.
- c. Modality to model: where a single image from some imaging modality is registered to a mathematical model.

- d. Patient to modality: where registration is used to help position the patient for treatment.

8. Subject

- a. Intrasubject: where images to be registered come from the same patient.
- b. Intersubject: where registration is performed using images acquired from different patients.
- c. Atlas: where an image from a single patient is registered to an image created from an image database.

9. Object

- a. Head (brain, eye, dental)
- b. Thorax (entire, cardiac, breast)
- c. Abdomen (general, kidney, liver)
- d. Pelvis and perineum
- e. Limbs (general, femur, humerus, hand)
- f. Spine and vertebrae

1.3.3 Image Registration Algorithms

Registration algorithms compute image transformations that establish correspondence between points or regions within images, or between physical space and images [Hajnal, *et al.*, 2001]. Depending on the nature of the problem at hand and the type of transformation involved, one can choose to apply a registration algorithm most suitable for the required computation. Algorithms available for rigid transformations can be categorized as landmark-based, surface-based, and voxel-based.

Landmark-based registration algorithms make use of corresponding fiducial points in the two corresponding image sets. The point landmarks can be either external (fixed to the patient) or internal (anatomical). For rigid structures, the algorithm requires only three noncollinear points to establish the transformation between two image volumes. However, it is desirable to have more points to minimize the transformation error associated with identifying the points. Once all the points in both image sets are picked, the algorithm computes the landmarks centroid for each set. The difference between the two centroids indicates the translational component of the overall transformation that has to be applied to one of the sets iteratively until the sum of squared distances between related points is minimized [Hajnal, *et al.*, 2001]. An example of a landmark-based algorithm is the Procrustes algorithm, which uses isomorphic scaling, translations, and rotations to establish the transformation between two 3D image sets.

Surface-based algorithms outline corresponding surfaces in two images and use them for registration. Similarly to the landmark-based approach, these algorithms compute a transformation that minimizes the distance between the two surfaces. The two most commonly used techniques are the “head and hat” algorithm and the iterative closest point algorithm [Hajnal, *et al.*, 2001]. Although these algorithms use more available image data than the landmark-based algorithms, they have a tendency to fail when the surfaces show symmetries to rotations, which leads to poorly defined transformation constraints.

Voxel-based algorithms require neither identification nor delineation of corresponding structures but instead compute the transformation using voxel intensities alone. The transformation is determined through an iterative process, where some voxel similarity measure obtained directly from the voxel values is optimized. Registration using voxel similarity measures generally

works well for intramodality registration, however, the voxel intensity values of intermodality images cannot be related by a simple arithmetic operation, and so preprocessing is sometimes required to make the images more alike. More recently developed algorithms, based on ideas of image entropy and information theory, are applicable to both intermodality and intramodality registration and frequently do not require any preprocessing. These algorithms include ratio image uniformity, correlation techniques, minimizing intensity difference, partition intensity uniformity, and information theory techniques [Hajnal, *et al.*, 2001].

While both affine and projective transformations can be computed using algorithms similar to those described above, other non-rigid transformations require different methods such as basis functions, splines, and finite element modeling. The latter algorithms will not be described here, as they are outside of the scope of the research described in this thesis.

1.3.4 Information Theory Techniques

Voxel-based image registration can be described as maximizing the amount of information shared between two images, or equivalently as minimizing the amount of information in the combined image, which implies using a measure of information to gauge registration accuracy. Originating from communication theory developed in the 1940's, the measure of information most commonly used in image processing is the Shannon-Wiener entropy [Hajnal, *et al.*, 2001] given by:

$$H = -\sum_i p_i \log p_i \quad 1.1$$

where H is the average information supplied by a set of i symbols whose probabilities of occurrence are given by $p_1, p_2, p_3, \dots, p_i$. As such, entropy measures the dispersion of a probability distribution of voxel intensity values. Therefore, a single image containing many voxels of the same intensity will have low entropy, or equivalently convey little information, while an image containing approximately equal portions of a large number of different intensities will have high entropy, and hence convey much more information.

1.3.4.1 Joint Entropy

Similarly to using entropy as an information measure for a single image, one can use joint entropy to measure the amount of information in two overlapping images A and B , where the two values at each overlapping voxel location can be used to evaluate a proposed registration transformation τ between the images. Joint entropy can be described using a feature space, or two-dimensional histogram of voxel intensities, for corresponding points in each of the images. Normalizing the joint histogram to the total number of voxels in the overlapping regions of the images yields a joint probability distribution function, $p_{A,B}^\tau$, of voxel intensity values in images A and B , and therefore the joint entropy $H(A, B)$ is given by:

$$H(A, B) = - \sum_{a,b} p_{A,B}^\tau(a, b) \log p_{A,B}^\tau(a, b) \quad 1.2$$

where a and b are voxel intensity values in images A and B respectively.

Based on the assumption [Woods, *et al.*, 1993] that voxels corresponding to the same anatomical structures have correlated intensity values in both images, the feature space will show clusters for the gray values of those structures when the images are registered correctly [Pluim, *et al.*,

2003]. On the contrary, misregistration of the images will manifest as a dispersion of the signal and a decreased intensity of the clusters. Therefore, registration of the images A and B can be achieved in principle by finding the transformation τ that minimizes their joint entropy.

However, an important limitation of joint entropy as a measure of registration is that it favours transformations for which either the background or structures of interest dominate in the image overlap region [Studholme, *et al.*, 1999]. Considering that the background tends to occupy the lower value intensity bins, a joint entropy minimization algorithm could favour the solution that maximizes the amount of background in the overlap region, which would lead to a complete misalignment while still yielding a low entropy value.

1.3.4.2 Mutual Information

To overcome this limitation of the joint entropy algorithm, in addition to the joint information one has to consider the information contributed to the overlap domain by each individual image. That is, one needs to include the marginal entropies $H(A)$ and $H(B)$ of images A and B, respectively, as well as their joint entropy. Mutual information, $I(A,B)$, is an information theory metric that measures joint entropy with respect to the marginal entropies. Collignon and colleagues, and Viola and Wells introduced the mutual information measure independently and simultaneously in the mid 1990's [Pluim, *et al.*, 2003]. In a qualitative sense, mutual information can be understood as a means of demonstrating how well one image explains the other. There are three different forms that one can use to express mutual information as used in image registration. The form most closely related to joint entropy is

$$I(A,B) = H(A) + H(B) - H(A,B) \quad 1.3$$

indicating that maximizing the mutual information is equivalent to minimizing the joint entropy. The marginal entropies in Equation 1.3 are simply those of the overlapping portions of images A and B, given by [Hajnal, *et al.*, 2001]:

$$H(A) = -\sum_a p_A^T(a) \log p_A^T(a) \quad 1.4$$

$$H(B) = -\sum_b p_B^\tau(b) \log p_B^\tau(b) \quad 1.5$$

where p_A^T and p_B^τ are the marginal probability distributions for sets a and b of intensity values in images A and B, and correspond to transformations T and τ , respectively. The marginal entropies will have low values when the overlapping regions consist of background only, and high values when they contain structures of interest, thus maximizing mutual information when the alignment of anatomical structures is good.

1.3.4.3 Normalized Mutual Information

Although mutual information is less sensitive to inappropriate changes in the overlap region than joint entropy, it does not entirely solve the overlap problem. In particular, the mutual information measure favours the solution where the relative volumes of structures of interest and background in the overlap region are equal [Studholme, *et al.*, 1999], which may lead to an incorrect solution. To overcome this problem, Studholme *et al.* introduced a new measure, normalized mutual information (NMI) – which is independent of changes in the marginal entropy values in the overlap region. The form of NMI

proposed by Studholme *et al.*, given in Equation 1.6, implies that NMI – based registration algorithms prefer a solution where the joint entropy is minimized with respect to the marginal entropies.

$$NMI(A, B) = \frac{H(A) + H(B)}{H(A, B)} \quad 1.6$$

Employing the normalized mutual information measure for registration of multimodality images is currently being widely investigated [Pluim, *et al.*, 2003].

1.4 Research Objective and Overview of Thesis

The main aim of the research program of which this project forms a part is to develop, implement and evaluate new clinical visualization methods that will allow for a better assessment of permanent prostate implant quality and more accurate post-implant dosimetry. Considering that image registration appears to provide a promising means to improve post-dosimetry accuracy, our primary objective here is to investigate the suitability of the NMI registration approach for automatic registration of clinical CT and MR image volumes.

A record of the investigations done in this research is organized into four chapters that follow. Chapter 2 describes preliminary testing of an NMI algorithm performed using images of a simple water phantom and presents important observations drawn from these experiments. In Chapter 3 we provide the details about acquisition of clinical CT and MR images and their salient characteristics. In Chapter 4, we introduce and describe a novel hybrid approach to registration of clinical prostate implant images. We also report the registration results obtained for simulated and clinical images, and from these

draw conclusions concerning the clinical applicability of the hybrid method. Finally, Chapter 5 provides the thesis summary and some suggestions for future work in this field.

Isotope	Half-life [days]	Gamma Energy [MeV]	Half-value Layer [mm lead]	Source Form
I-125	59.4	0.0274 (avg)	0.025	seed
Pd-103	17	0.020 - 0.023	0.008	seed

Table 1.1 Physical properties of radionuclides used in brachytherapy
[Khan, 2003]

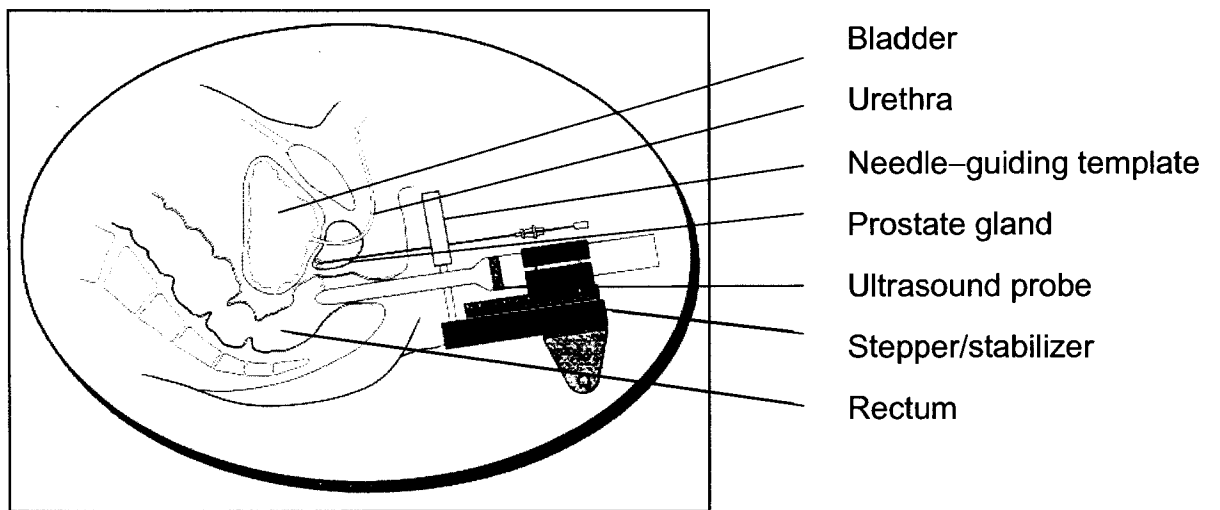


Figure 1.1 Transperineal ultrasound-guided permanent implant technique

1. 5 References

1. Chan J. M., Jou R. M., Carrol P. R., The relative impact and future burden of prostate cancer in the United States, *The Journal of Urology*, 172, S13-S17 (2004)
2. Dubois D. F., Prestidge B. R., Hotchkiss L. A., Bice W. S., Prette J. J., Source localization following permanent transperineal prostate interstitial brachytherapy using magnetic resonance imaging, *International Journal of Radiation Oncology, Biology, Physics*, 39(5), 1037-1041 (1997)
3. Dubois D. F., Prestidge B. R., Hotchkiss L. A., Prette J. J., Bice W. S., Intraobserver and interobserver variability of MR-imaging and CT-derived prostate volumes after transperineal interstitial permanent prostate brachytherapy, *Radiology*, 207, 785-789 (1998)
4. Hajnal J. V., Hill D. L. G., Hawkes D. J., "Medical Image Registration" CRC Press, New York, (2001)
5. Heintz B. H., Wallace R. E., Havezi J. M., Comparison of I-125 sources used for permanent interstitial implants, *Medical Physics*, 28(4), 671-682 (2001)
6. ICRU, ICRU Report 38: Dose and volume specification for reporting intracavitary therapy in gynecology, (1985)
7. Khan F. M., "The Physics of Radiation Therapy" , Lippincott Williams & Wilkins, Philadelphia, (2003)

8. Kunos C. A., Resnick M. I., Kinsella T. J., Ellis R. J., Migration of implanted free radioactive seeds for adenocarcinoma of the prostate using a Mick applicator, *Brachytherapy*, 3(2), 71-77 (2004)
9. Lee W., Moughan J., Owen J., Zelefsky M., The 1999 patterns of care survey of radiation therapy in localized prostate cancer – A comprehensive survey of prostate brachytherapy in the United States, *International Journal of Radiation Oncology, Biology, Physics*, 57(2), S256 (2003)
10. Maintz J. B. A., Viergever M. A., A survey of medical imaging registration, *Medical Image Analysis*, 2(1), 1-36 (1998)
11. Nag S., Bice W., DeWyngaert K., Prestidge B., Stock R., Yu Y., The American Brachytherapy Society recommendations for permanent prostate brachytherapy postimplant dosimetric analysis, *International Journal of Radiation Oncology, Biology, Physics*, 46(1), 221-230 (2000)
12. Peschel R. E., Colberg J. W., Surgery, brachytherapy, and external-beam radiotherapy for early prostate cancer, *The Lancet Oncology*, 4(4), 233-241 (2003)
13. Pluim J. P. W., Maintz J. B. A., Viergever M. A., Mutual-information-based registration of medical images: a survey, *IEEE Transactions on Medical Imaging*, 22(8), 986-1004 (2003)
14. Ragde H., Korb L. J., Elgamal A. A., Grado G. L., Nadir B.S., Modern prostate brachytherapy. Prostate specific antigen results in 219 patients with up to 12 years of observed follow-up, *Cancer*, 89(1), 135-141 (2000)

15. Roy J. N., Wallner K. E., Harrington P. J., Ling C. C., Anderson L. L., A CT-based evaluation method for permanent implants: application to prostate, *International Journal of Radiation Oncology, Biology, Physics*, 26(1), 163-169 (1993)
16. Stone N. N., Hong S., Lo Y., Howard V., Stock R. G., Comparison of intraoperative dosimetric implant representation with postimplant dosimetry in patients receiving prostate brachytherapy, *Brachytherapy*, 2(1), 17-25 (2003)
17. Studholme C., Hill D. L. G., Hawkes D. J., An overlap invariant entropy measure of 3D medical image alignment, *Pattern Recognition*, 32(1), 71-86 (1999)
18. Van Dyk J., "The Modern Technology of Radiation Oncology", Medical Physics Publishing, Madison, (1999)
19. Woods R. P., Mazziotta J. C., Cherry S. R., MRI-PET registration with automated algorithm, *Journal of Computer Assisted Tomography*, 17(4), 536-546 (1993)
20. Yu Y., Anderson L. L., Li Z., L., Mellenberg D. E., Nath R., Schell M. C., Waterman F. M., Wu A., Blasko J. C., Permanent prostate seed implant brachytherapy: Report of the American Association of Physicists in Medicine Task Group No. 64, *Medical Physics*, 26(10), 2054-2073 (1999)

CHAPTER 2

2 IMAGE REGISTRATION FOR PROSTATE IMPLANTS

In this chapter we describe the specific problem dealt with in our research, as well as the methods and materials that we utilized in seeking a solution. We discuss how registration of CT and MR prostate implant image volumes can be used to address a problem with current post-implant dosimetry practice, and we describe, in detail, two registration algorithms that we used for CT-MR image registration and their software implementations.

2.1 Prostate Implant Visualization

As discussed previously in Section 1.2.2.3.1, post-implant dosimetry for permanent prostate implants plays an important role in assessing implant quality and treatment outcome. In order to perform accurate post-dosimetry calculations for permanent prostate implants, it is necessary to accurately outline the prostate volume and accurately determine the locations of all implanted seeds. As illustrated in Figure 2.1 a, the prostate contour is poorly visualized in the pelvic CT image, while the seeds are clearly visible. On the contrary, as we see in Figure 2.1 b, the MR image provides excellent soft tissue delineation, while the seeds are hard to distinguish from blood vessels and other signal voids. Considering that CT and MR images of the implanted prostate provide complementary information, it is natural to attempt to find a way to combine the benefits of the two modalities. This could be accomplished by image registration.

There are a variety of algorithms that could be used to attempt to perform image registration. In our research project we need to register a relatively small volume containing the prostate gland and immediately surrounding soft tissues for which there is little or no evidence of shape deformation, and therefore it is reasonable to apply a rigid-body transformation. Two image registration algorithms that have been used for rigid-body transformations in a variety of applications are:

1. Landmark-based registration, also known as the Procrustes algorithm, which is a well-established procedure, and
2. Normalized Mutual Information, whose applications to medical imaging are being increasingly investigated due to the potential for automation.

Rigid-body transformation involves translations and rotations only. In three dimensions this gives in total six degrees of freedom, which can be defined as translations t_x , t_y , and t_z along the X, Y, and Z axes respectively, and rotations α , β , and γ applied in a counterclockwise direction about the X, Y, and Z axes, respectively. In our image analysis we used the left-handed Cartesian coordinate system shown in Figure 2.2 (for compatibility with available image registration software). All translations and rotations are applied with respect to the center of the image volume, which is taken as the transformation origin. The translational and rotational components of a rigid-body transformation can be combined into a single 4x4 transformation matrix as follows,

$$T(\vec{r}) = \begin{pmatrix} s_x(\cos\beta\cos\gamma) & s_y(\cos\beta\sin\gamma) & s_z(-\sin\beta) & 0 \\ s_x(\sin\alpha\sin\beta\cos\gamma - \cos\alpha\sin\gamma) & s_y(\sin\alpha\sin\beta\sin\gamma + \cos\alpha\cos\gamma) & s_z(\sin\alpha\cos\beta) & 0 \\ s_x(\cos\alpha\sin\beta\cos\gamma + \sin\alpha\sin\gamma) & s_y(\sin\alpha\cos\alpha\sin\beta - \sin\alpha\cos\gamma) & s_z(\cos\beta\cos\alpha) & 0 \\ s_x t_x & s_y t_y & s_z t_z & 1 \end{pmatrix} \quad 2.1$$

where the transformation is applied using so-called homogeneous coordinates $\vec{r} = (x, y, z, \phi)$. s_x , s_y and s_z are scaling factors applied if the images being registered are not calibrated to the same spatial scale.

Considering the problem classification scheme discussed in Section 1.3.2, we can classify the prostate image registration problem at hand as:

- Multimodal – registering images from two modalities (CT and MR);
- Three-dimensional – registering volume datasets;
- Local – transformations are applied locally due to the mobility of the prostate gland with respect to bony structures and other pelvic organs;
- Rigid-body – registering volumes considered to be non-deformed;
- Semi-automatic (Procrustes) – initialization of the registration process is required;
- Automatic (NMI) – if registration can be done automatically and user interaction is minimal. Otherwise, classification is semi-automatic;
- Intrasubject – registering images coming from the same subject; and
- Intrinsic – no external fiducial markers are used.

2.2 Landmark-Based Registration – Procrustes Algorithm

Landmark-based registration is founded on identification of corresponding landmark points or so called fiducial points in two corresponding images.

In order for a landmark-based algorithm to establish the transformation between two 3D image volumes, the user must identify a set of at least three non-collinear points in each of the base (stable reference) and the match (transformed) images to be aligned. Each point representing some identifiable feature in the match image has a corresponding point representing the same feature in the base image. The greater the number of fiducial points identified, the smaller the influence of the error made in marking these points and the more accurate the registration is.

To perform the registration, the Procrustes algorithm determines the transformations required to align the corresponding fiducial points. To calculate these transformations, the algorithm first computes the centroids of each set of points. It then uses the difference between the centroids to determine the 3D translation that must be applied to the set of points in the match image. This translated point set is then rotated about its new centroid until the distance between corresponding points in the two images is minimized in the root-mean-square (RMS) sense. The RMS distance to be minimized is commonly termed the fiducial registration error (FRE), and the problem of landmark-based registration consists of finding a 3D translation t and a rotation R that minimize the FRE given by:

$$FRE^2 = \frac{1}{N} \sum_{i=1}^N |Rx_i + t - y_i|^2 \quad 2.2$$

where $\{x_i\}$ and $\{y_i\}$ are corresponding fiducial point sets, each containing N points [Fitzpatrick, *et al.*, 1998].

2.2.1 Procrustes Algorithm in VariSeed 7.1

VariSeed 7.1 (Varian Medical Systems Inc., Palo Alto, CA) is a commercial software package that is used for prostate brachytherapy treatment planning and evaluation. It provides tools to allow prostate treatment evaluation based on image volumes registered using the Procrustes algorithm. We will use this algorithm as a reference for the registration of clinical CT and MR volumes.

Once imported into VariSeed 7.1, CT and MR image files can be viewed simultaneously in a image fusion window. Using a cursor, a user can select 3 or more non-collinear data points on a primary image volume and corresponding points on a secondary image volume. Once the matching points are chosen, the algorithm proceeds to register the image volumes based on the selected fiducials. Using an image blending tool, a user can adjust the display of the fused images to visually assess registration quality. Quantitatively, registration accuracy can be assessed from the FRE reported by the algorithm. The software also provides tools that can be used to manually pick other pairs of corresponding points for which a user wants to calculate the RMS difference.

2.3 Normalized Mutual Information Registration

Although the landmark-based registration algorithm is an adequate reference standard for determination of rigid-body transformations, the identification of fiducial points requires user interaction, is usually a time consuming process, and may be inaccurate if corresponding fiducial points cannot be identified with certainty. On the contrary, voxel property-based algorithms do not require identification of corresponding structures, but instead

use a contiguous subset of the image content to perform registration. As such, voxel property-based algorithms such as NMI could be made automatic and should be more efficient. The formulation of the NMI metric that we used in this research was described by Studholme and colleagues in 1999, and is given in Equation 2.3 below. It is defined as the ratio between the sum of marginal entropies $H(A)$ and $H(B)$ of images A and B, respectively, and their joint entropy, $H(A,B)$, in the overlap region. As discussed earlier in Section 1.3.4, these entropies measure the information content in the images A and B and in the overlap region, respectively.

$$NMI(A, B) = \frac{H(A) + H(B)}{H(A, B)} \quad 2.3$$

2.3.1 Information Measures

According to Equation 2.3, one can quantify image alignment by measuring the information content in the pair of images being registered. The amount of information that an image contains is directly proportional to the number of possible voxel values occurring in it. The less certain we are about which value will occur in an image, the more information we gain from the image. This idea is described by the Shannon-Wiener entropy given by Equation 1.1 and is illustrated by varying the ratio between the foreground and background components in the simple 2D binary image shown in Figure 2.3. As the graph in Figure 2.3 shows, an image with similar numbers of each pixel value contains more information than an image where most of the pixels have the same value. We created the graph in Figure 2.3 based on ideas published by Studholme *et al.* in 1999.

In order to quantify the alignment between two images we need to determine the information content in the combined image in addition to

knowing the information content in each image separately. This is done by estimating the joint entropy in the region of overlap between the two images, where the information content will be minimized when the alignment is good. This is illustrated in Figure 2.4, displaying poorly aligned images in (a), and good alignment between the same images in (b). By visually inspecting these two images we can see that due to the duplication of image regions seen in (a), the amount of information in the combined image with poor alignment is greater than the amount of information in the combined image with good alignment in (b). The joint entropy of two images is minimized when the probability that certain pairs of values will occur together is highest. Therefore, to minimize the joint entropy of two images, we seek a registration transformation for which it is easiest to guess what pair of values a voxel will have in the overlap region of the combined image [Studholme, *et al.*, 1999].

2.3.2 NMI Algorithm as Implemented in Analyze 5.0

To register image datasets according to the NMI measure we utilized Analyze 5.0 (AnalyzeDirect Inc., Lenexa, KS), a commercially available software package. This software was created by the Biodynamic Research Unit at Mayo Clinic in Rochester MN and provides comprehensive, generic tools for visualization, processing, and quantitative analysis of biomedical images. It allows multiple image volumes to be simultaneously accessed and processed by different programs in a multi-window interface. For the purpose of this thesis we concentrate on describing the steps required to perform image registration and the operational basics of the registration algorithm in Analyze 5.0 [Camp & Robb, 1999].

In order to perform image registration one first needs to import the image sets of interest into the Analyze workspace. An image set can be imported as a series of individual 2D slices constituting a volume, or as a

single 3D dataset where the slices have been combined to create the image volume. The registration software allows a user to set some parameters which refine the selection and processing of the imported volumes prior to registration. More specifically, a user is able to:

- Define a region of interest that determines the extent of the image volume on which the transformations are to be performed;
- Set upper and lower intensity threshold levels to discard noise and image structures of no interest;
- Set limits on search parameters such as translational and rotational search ranges, to prevent the algorithm from exploring inappropriate regions of the transformation search space and from potentially finding a false maximum of the NMI function.

In addition, a user can apply specified transformations to the match image using a manual matrix tool. All of the changes made on an image volume can be saved for later use. Appropriate image pre-processing with the above tools can help to increase the robustness and efficiency of the image registration algorithm.

The normalized mutual information algorithm implemented in Analyze 5.0 uses extensive volume sub-sampling and a histogram preservation binning technique to perform automatic image registration [Camp & Robb, 1999]. Voxel values across an image are grouped into sixteen bins of unequal width, making the image less noisy. The registration process is performed using a progressive image resolution search approach [Pluim *et al.*, 2003] where translation and rotation steps become finer with each iteration. The cost function optimization process used during registration searches translational degrees of freedom first, followed by the rotational degrees of freedom. The order of translational degrees of freedom is X-Y-Z, while the order of rotational degrees of freedom is γ - β - α (see Figure 2.2). This search sequence occurs at

each resolution step during the optimization process, with the initial orientation of the match volume determined by the transformation obtained at the previous resolution level, and the search interval reduced at each subsequent step. Transformations are applied against a left-handed coordinate system where positive rotations are assumed to be right-handed (see Figure 2.2), and all rotations are specified about the center of the image volume.

2.3.2.1 Preliminary Tests of NMI Algorithm – Phantom Studies

In our early work with Analyze 5.0 we attempted automatic registration of CT and MR image volumes of a cylindrical water phantom containing inserts made of materials of different density. This investigation consisted of a couple of tests:

- Registration of two CT images of the phantom, with the match image in a different position than the reference image;
- Registration of CT and MR images of the same phantom with minimal change in the phantom position between two scans, as would be the situation for pelvic images of prostate implant patients.

The purpose of these exercises was to gain better insight into the basic requirements needed to achieve automatic registration with the NMI algorithm implemented in Analyze 5.0.

2.3.2.2 CT-CT Registration

The phantom used in this exercise was a large plastic water-filled cylindrical object containing six cylindrical inclusions of various densities, as illustrated in Figures 2.5 and 2.6. CT image sets were acquired with a Picker PQ-5000 CT scanner (Philips Medical Systems, Bothell, WA) performing an axial scan. Image sets consisted of fifteen slices, each 3 mm thick with no

inter-slice gap. The phantom long axis in the reference CT image set was aligned with the axis of the CT scanner bore. The phantom was then rotated counter-clockwise by 25° and translated vertically by 23 mm with respect to the reference position, and the second image set was obtained. Both image sets were imported into the Analyze 5.0 workspace to perform registration.

Attempts to register the two image sets automatically without any restrictions on search parameters failed, as illustrated in Figure 2.7. Using image pre-processing tools provided by the Analyze 5.0 software, we found that at very low intensities our image volumes contained a considerable amount of information coming from the CT table. The algorithm was consequently misguided, and registration was performed based on irrelevant information, which resulted in the irrelevant structure (CT table) being perfectly aligned while the structures of interest (inserts in the phantom) were not. We used a threshold tool to discard the low intensity values associated with the CT table and repeated the registration. This time registration was successful and the structures of interest were well matched. See Figure 2.7.

2.3.2.3 CT-MR Registration

We further tested the capabilities of the NMI algorithm by attempting registration of CT and MR images of the same water phantom. Before scanning the water phantom was filled with CT and MR contrast agents (iodine-based for CT and copper-sulfate for MR). Solid cylindrical inclusions were replaced with cylindrical volumes containing different concentrations of contrast agents. The CT volume set was obtained using the same scanner and acquisition parameters as described in previous section. The MR image set was acquired using a Philips Gyroscan Intera 1.5T system (Philips Medical Systems, Bothell, WA) with a cardiac surface coil, employing a turbo spin echo sequence with echo time $TE = 105$ ms and repetition time $TR = 4401$ ms. The

slice thickness was 3 mm with no inter-slice gap. To minimize the difference in phantom position between the scans, the long axis of the water phantom was approximately aligned with the axes of the CT and MR scanner bores prior to imaging.

We attempted to perform unrestricted automatic registration of the CT and MR volumes, however, it was not successful. We examined the image sets acquired, and found that the CT couch was visible in the CT volume set, but provided no signal in the MR image volume. We postulated that the algorithm had failed due to the considerable difference in information content between the two image sets. To deal with this problem, we used an outlining tool to choose a volume of interest within the boundaries of the phantom in the MR (match) image, thereby excluding the region of signal void from consideration. Automatic registration performed on this VOI resulted in a good alignment of structures of interest (Figure 2.8).

Through the exercises described above, we observed that:

- It is important to minimize the change in object position between scans;
- The user must be aware of all the information that the image contains;
- Threshold tools can serve to guide the registration process;
- The VOI outlined in the match image (which defaults to the full match image volume) should not include structures present in only one of the image sets.

Having gained experience in applying the NMI algorithm to phantom images, we were better prepared to proceed to clinical images of implanted prostate glands. The characteristics of anatomical features visible in CT and MR images of the pelvis are described in the following chapter.



a



b

Figure 2.1 a) Axial CT image of permanent prostate implant; b) Axial T2-weighted MR image of implanted prostate.

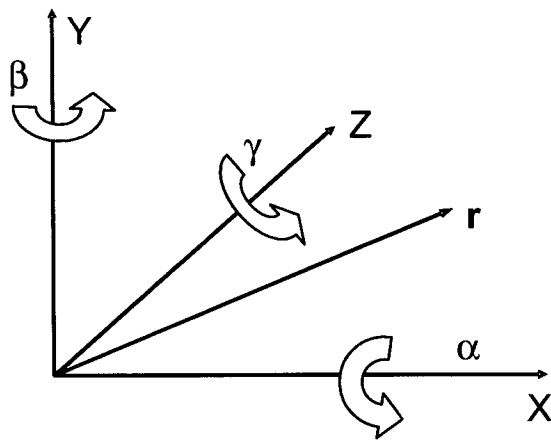


Figure 2.2 Left-handed Cartesian coordinate system used in this work.

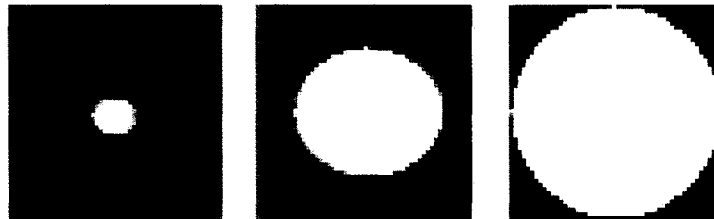
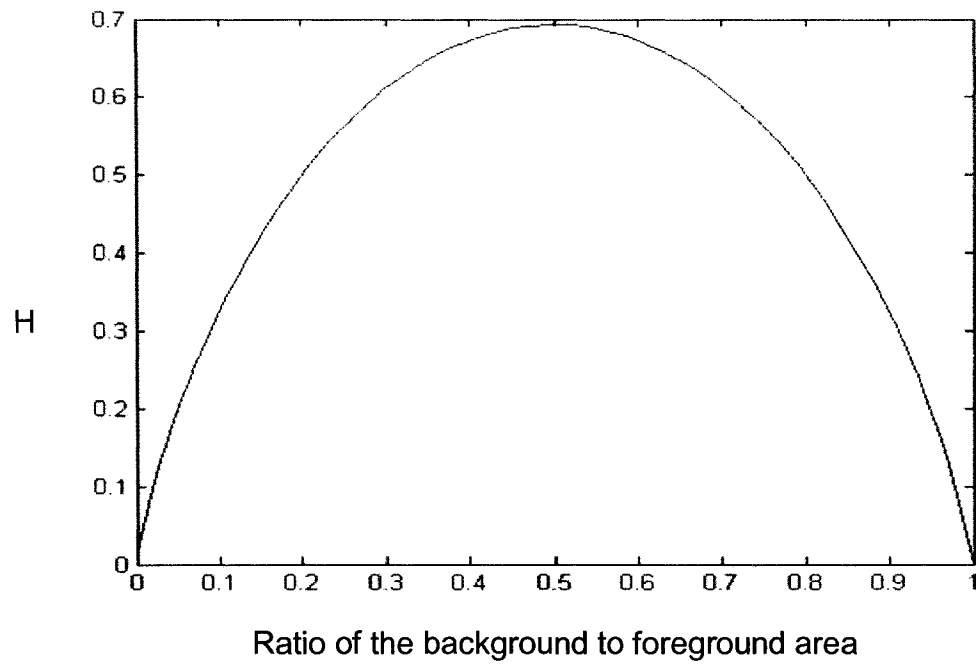


Figure 2.3 Information content H of a binary image consisting of foreground (f) and background (b) with probabilities $p(f)$ and $p(b)$, respectively, where $p(f) = 1 - p(b)$.

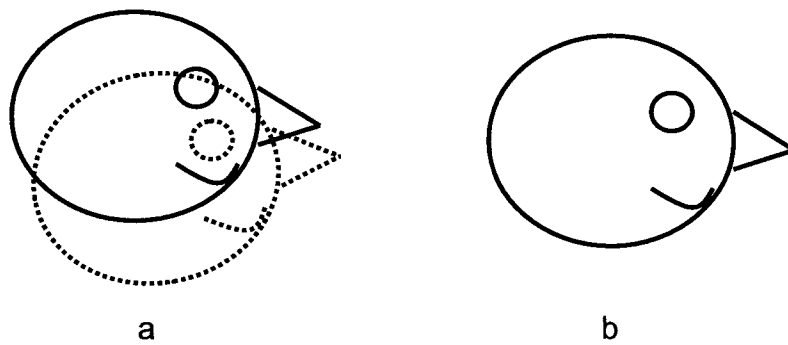


Figure 2.4 The information content in a combined image: a) is higher with poorly aligned base and match images; b) is minimized with well aligned base and match images.

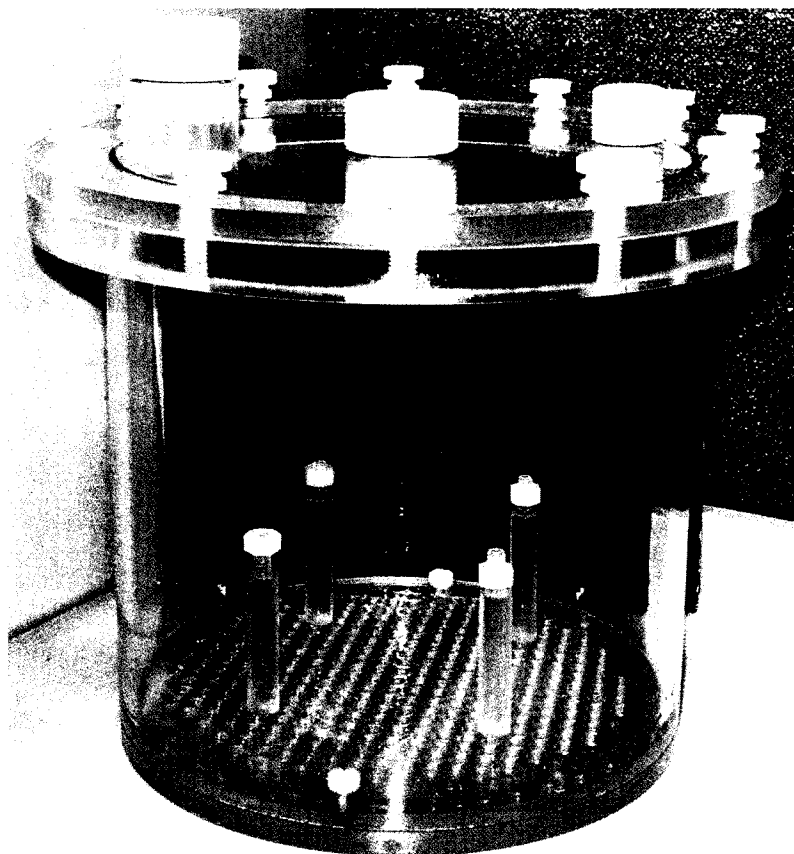


Figure 2.5 A photograph of the water-filled cylindrical container used to hold different phantom inserts utilized in our experiments.

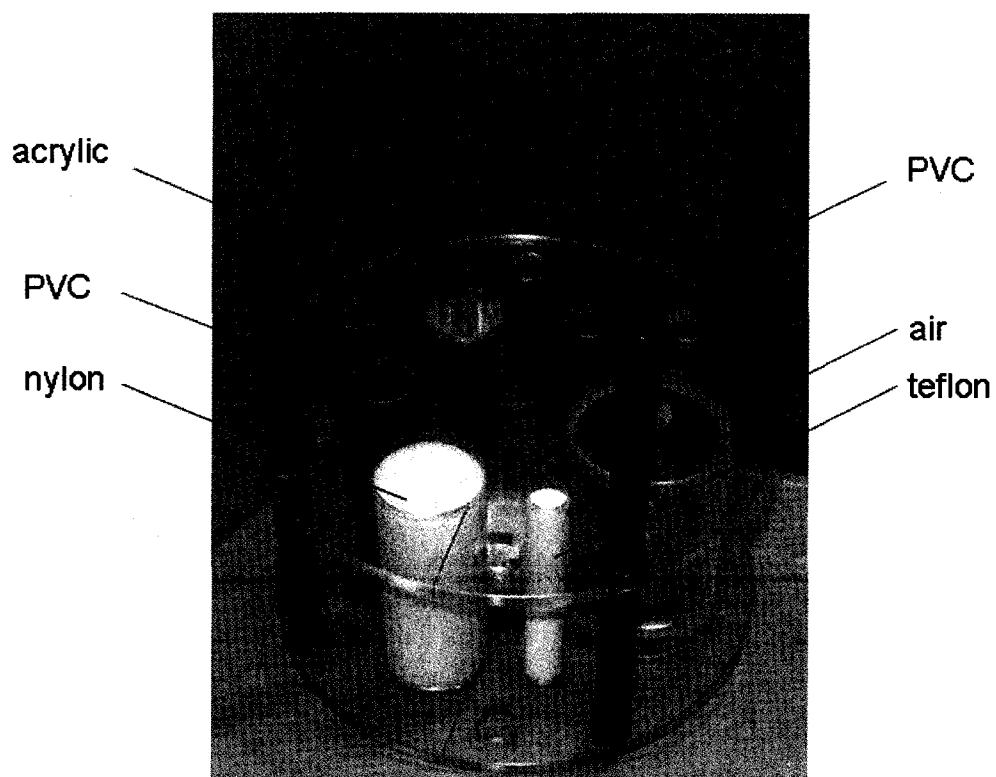


Figure 2.6 A photograph showing an ensemble of inserts made of different density materials used in our phantom studies.

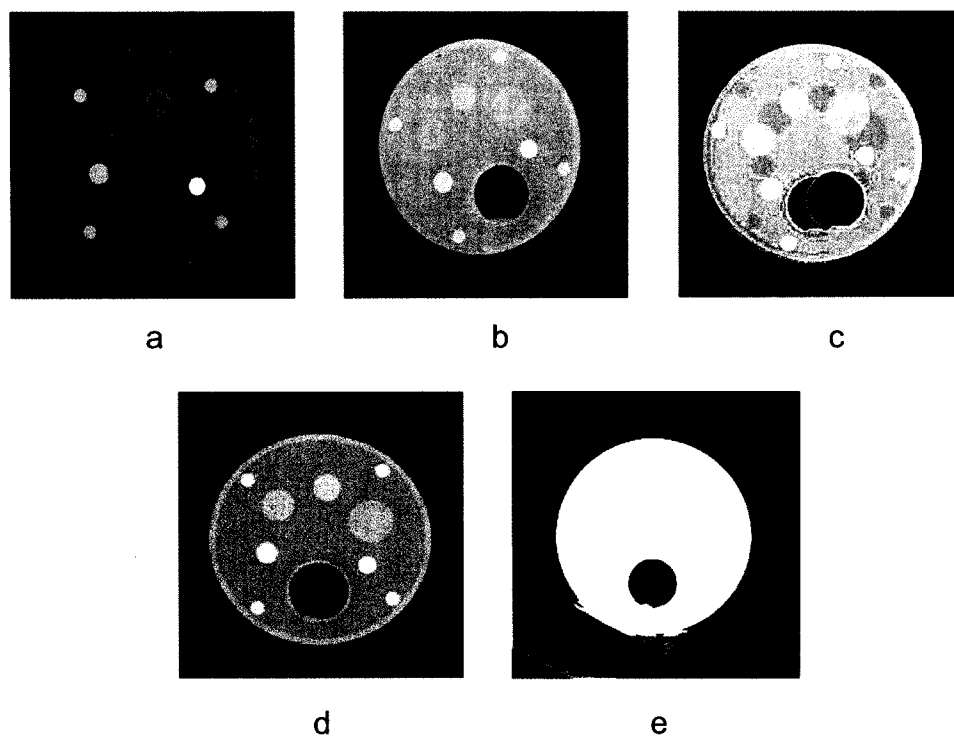


Figure 2.7 3D CT-CT registration of images of a water phantom containing inserts: a) reference volume; b) displaced volume; c) unrestricted registration; d) registration after thresholding; e) registered volumes displayed using a window highlighting low intensities to show the CT couch.

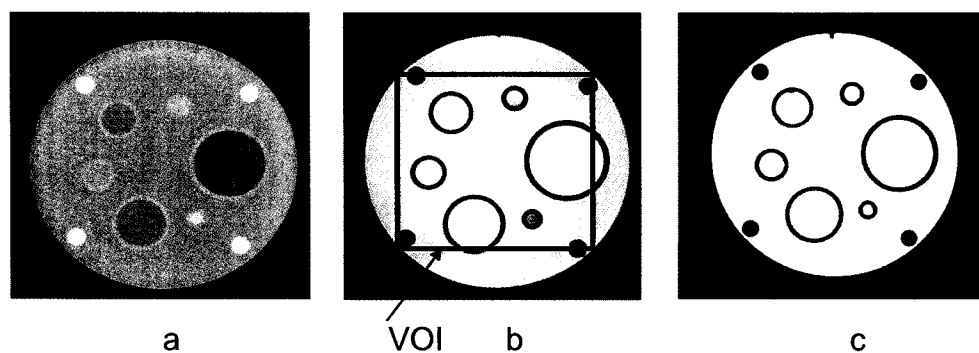


Figure 2.8 CT-MR registration of the water phantom: a) CT - reference image; b) MR image positioned similarly to the reference image, with a registration VOI outlined; c) correctly registered volumes.

2. 4 References

1. Camp J., Robb R. A., A novel binning method for improved accuracy and speed of volume image co-registration using normalized mutual information, *Proceedings SPIE – The International Society for Optical Engineering*, 3661, 24-31 (1999)
2. Fitzpatrick J. M., West J., Maurer C. Jr., Predicting error in rigid-body, point-based registration, *IEEE Transactions on Medical Imaging*, 17(5), 694-702 (1998)
3. Hajnal J. V., Hill D. L. G., Hawkes D. J., “Medical Image Registration” CRC Press, New York, (2001)
4. Pluim J. P. W., Maintz J. B. A., Viergever M. A., Mutual-information-based registration of medical images: a survey, *IEEE Transactions on Medical Imaging*, 22(8), 986-1004 (2003)
5. Studholme C., Hill D. L. G., Hawkes D. J., An overlap invariant entropy measure of 3D medical image alignment, *Pattern Recognition*, 32(1), 71-86 (1999)

CHAPTER 3

3 POST-IMPLANT CT AND MR IMAGES USED FOR DOSIMETRIC EVALUATION

Although CT-based dosimetric assessment of permanent prostate implants is presently the standard practice recommended professionally [Yu *et al.*, 1999 and Nag *et al.*, 2000], MR images contain valuable complementary information that, when combined with CT, promises to improve implant assessment accuracy. This chapter describes CT and MR image volume datasets useful for post-implant dosimetric assessment. The image acquisition protocol, appearance of anatomical features in the images, and image suitability for dose estimation in anatomical structures of interest are presented for one CT and two MR imaging techniques. Determining a means to combine the quantitative information contained in CT-MR image volumes via an efficient registration process is the primary focus of this thesis. For registration to yield meaningful results, however, the datasets being registered must represent the patient anatomy with acceptable geometric fidelity. As a consequence the latter portion of this chapter is devoted to measurements of the spatial distortion inherent to the three imaging techniques of interest.

3.1 CT Image Volumes

3.1.1 Principles of CT Imaging

Computed tomography refers to cross-sectional imaging of objects by transmission of X-rays from different orientations. A group of rays traversing an

object at the same orientation is called a projection. CT image volumes can be acquired using either:

- parallel beam geometry, in which all the rays in a projection are parallel to each other, or
- fan beam geometry, in which the rays diverge from a common point.

CT scanners perform either a conventional scan (slice-by-slice data acquisition), or a helical scan (volume data acquisition). In conventional scanning the X-ray tube rotates around the patient to collect the data from a single slice. The patient is then moved to a new position and the tube rotates again to scan the next slice. In the case of helical scanning, both the patient and the X-ray tube move continuously. The X-ray tube rotates around the patient while the couch is translated through the gantry of the scanner. These two motions create a net effect of the X-ray tube traveling in a helical path around the patient [Bushberg *et al.*, 2002].

The basic principle of CT imaging is the attenuation of the X-ray beam by the tissues along the beam path. Attenuation depends on tissue density, beam energy, tissue atomic number and tissue electron density. Attenuated X-ray signals are measured by collimated detectors that send digitized readings to a computer where axial image reconstruction from projections is performed. Reconstructed images can be viewed on a video monitor and subsequently saved on a disk for future reference [Seeram, 2001]. Each pixel in the reconstructed image represents the average X-ray attenuation properties of the tissue imaged. The amount of attenuation that occurs is indicated by the value of the linear attenuation coefficient μ . For a monochromatic beam traversing a given thickness of homogenous tissue:

$$N = N_0 e^{-\mu x} \quad 3.1$$

where N is the number of transmitted photons, N_0 is the number of incident photons, X is the thickness of the traversed tissue, and $\mu=(\mu_p + \mu_c)$ is the linear attenuation coefficient along the ray path, that consists of linear attenuation coefficients μ_p resulting from photoelectric absorption and μ_c resulting from Compton scattering. The tissues traversed by a clinical polychromatic X-ray beam in a patient have different attenuation properties as well as different thicknesses. Therefore, the total attenuation coefficient is calculated using the formula given by Equation 3.2

$$I = I_0 e^{-\int \mu(X) dX} \quad 3.2$$

where I is the beam intensity measured by the detector, I_0 is the beam intensity that enters the patient and $\mu(X)$ is the tissue attenuation coefficient at position X along the beam path.

The X-ray beam in clinical CT is polychromatic consisting of photons with a range of energies. Low energy photons do not contribute to CT image formation (they are mostly absorbed), while they do contribute to patient dose. Beam filtration is used to remove the low energy photons and make a more spatially uniform energy distribution over the radiation beam area. Typically, the mean energy of an unfiltered X-ray beam is about 1/3 of its peak value. In the case of clinical CT the average beam energy is increased due to beam hardening that occurs as a result of filtration. Therefore, the mean energy of a pencil beam at a characteristic diagnostic tube voltage of 130 kVp is ~60 keV (about 1/2 of the peak tube voltage). At such beam energies Compton scattering interactions dominate over the photoelectric effect, which implies that the electron density of the tissues traversed plays an important role in determining the attenuation measured in CT imaging.

Pixel intensities in the reconstructed CT image are assigned a CT number which is related to the linear attenuation coefficient of the tissue according to the following equation:

$$CT_{number} = \frac{\mu_t - \mu_w}{\mu_w} K \quad 3.3$$

where μ_t is the attenuation coefficient of the imaged tissue, μ_w is the attenuation coefficient of water and K is a scaling factor equal to 1000 HU (Hounsfield Units). This normalization relative to attenuation of water results in CT numbers ranging from -1000 (for air) to + 3000 (for bone, metal and other dense structures).

3.1.2 CT Image Acquisition

Appropriate timing of post-implant imaging for prostate brachytherapy is important because of the effect of postoperative edema on dosimetry. According to recommendations in the AAPM TG-64 report [Yu, *et al.*, 1999], ^{125}I implants should be imaged 4 weeks postoperatively, which gives enough time for the edema to typically subside to $\leq 12.5\%$ of its original value. Therefore, CT images used for post-implant dosimetry are commonly acquired at this time.

The CT volume sets used in our research were therefore acquired 4 weeks post-implant with a Picker PQ-5000 scanner (Philips Medical Systems, Bothell, WA) applying a standard, non-helical scan with a field of view (FOV) of 150 mm and a reconstructed image pixel pitch of ~ 0.3 mm. The image volume consisted of approximately 35 3.0 mm thick axial slices, with no gap between them, spanning the region from 20 mm cephalad to the base of prostate to 20 mm caudad to its apex. As such, the CT image volume encompasses the

whole prostate gland and immediately surrounding pelvic tissues and organs (bones, rectum, seminal vesicles, bladder, muscle tissue, etc.).

3.1.3 Image Features

Considering that the CT scan provides information about the attenuating properties of the tissues imaged, the densest structures such as bones and implanted seeds appear brightest in the CT images, while the air in the rectum is shown with the lowest intensity (see Figure 3.2).

Adjoining soft tissue structures are quite poorly defined in CT images, because of the lack of contrast at the boundaries between them; hence, outlining these features can involve a considerable degree of approximation. Figure 3.2 (a) shows a caudal slice of the prostate image volume, which contains ischial bones and fatty and muscle tissues surrounding just visible rectum walls. We can also see a few implanted seeds, but the prostate contour and the boundary between the gland and the rectum are not clearly distinguishable. The image in Figure 3.2 (b) illustrates the mid-gland region, with the prostate (containing implanted seeds) occupying the center of the image. Prostate and rectum (located just below the prostate gland) are blended with surrounding soft tissues, which makes it hard to determine their contours with accuracy. Pelvic bones and seeds however, are well distinguished from the surrounding tissues. In the cranial slice of the prostate volume shown in Figure 3.2 (c) it is possible to identify the bladder, seminal vesicles and rectum.

3.1.4 Post-implant Dosimetry

Post-implant dosimetry is an essential part of prostate brachytherapy. It provides an insight into implant quality via estimation of the actual dose delivered to the prostate gland and surrounding normal tissues. As discussed in Section 1.2.2.3.1, post-implant dosimetry is currently performed using CT image volumes. Post-dosimetric analysis consists of the following steps [Stock & Stone, 2002]:

- Contouring the prostate and critical structures on every CT slice;
- Localizing all the implanted seeds;
- Calculating dose distributions to target volume and organs at risk;
- Generating isodose curves;
- Generating dose-volume histograms for prostate and structures at risk.

In order to perform accurate post-dosimetric analysis it is necessary to contour structures of interest and determine seed locations relative to those structures precisely. CT provides excellent visualization of the sources, but, as illustrated in Figures 3.1 and 3.2, clear delineation of adjoining soft tissue boundaries is not feasible. Therefore, significant uncertainties can and do exist in the results of dosimetric analyses based on CT images only [Stock & Stone, 2002].

3.2 MR Image Volumes

3.2.1 Principles of MR Imaging

Magnetic resonance imaging is a tomographic imaging technique based on the principles of nuclear magnetic resonance (NMR). It exploits magnetic properties of the element nuclei to obtain the images of body tissues.

Considering its physiologic concentration and isotopic abundance, the most relevant nucleus in clinical MR imaging is the hydrogen nucleus (proton) [Bushberg *et al.*, 2002].

Spinning unpaired protons exposed to a fixed external magnetic field B_0 , produced by a permanent or superconducting magnet in the bore of the MRI system, get distributed into two energy states: a low-energy state with spins parallel to the applied field and a high-energy state with spins antiparallel to the applied field. The applied magnetic field causes the precession of spins about the field axis (Z-axis) at an angular frequency ω_0 proportional to the field strength B_0 . This relationship is given by the Larmor equation below:

$$\omega_0 = \gamma B_0 \quad 3.4$$

where γ is the gyromagnetic ratio – a constant unique to each element. The vector sum of all individual spins gives a net magnetization vector in the direction of the external magnetic field.

When perturbed with short radio wave pulses (emitted by an RF transmitter coil) at their resonance frequency, protons are capable of absorbing electromagnetic energy delivered by these waves. If an RF pulse is transmitted along the axis perpendicular to the magnetization vector, a weak (~50 mT) oscillating magnetic field B_1 associated with this pulse will cause the protons to start precessing around the axis of the B_1 field at frequency ω_1 . Simultaneous precession of the spins about the B_0 and B_1 field directions results in a spiral motion of the net magnetization vector in the X-Y plane. Emission of the absorbed energy by the nuclei as they subsequently return to their initial spin state is what provides the MR signal. More specifically, the oscillating magnetic field associated with each precessing proton induces a

current in the RF receiver coil. The current measured by the receiver constitutes the MR signal, otherwise known as a free induction decay (FID).

Received signal intensity is a complicated function that collectively depends on proton density within a tissue sample, tissue specific relaxation times T_1 and T_2 , and imaging sequence parameters echo time (TE) and repetition time (TR). T_1 and T_2 relaxation times are tissue parameters that determine the image contrast. T_1 relaxation time is related to the spin-lattice interaction and measures how quickly the spinning nuclei emit their absorbed energy into the surrounding tissue. In other words it is a measure of the time that it takes the component of the magnetization vector parallel to the main magnetic field to return to its initial value. In a T_2 -weighted imaging sequence the contrast between tissues is based on the T_2 relaxation time. This parameter is associated with the decay of the component of the magnetization vector perpendicular to the main magnetic field due to spin-spin interactions. In addition to spin-spin interactions, a loss of transverse magnetization (local spin dephasing) occurs due to external magnetic field inhomogeneities. FID decay resulting from the combination of these two effects is characterized by relaxation time T_2^* . T_2^* is always less than T_2 and therefore, the tissue contrast in T_2 -weighted images is actually based on T_2^* relaxation. TE and TR are selectable machine parameters and represent the time between two neighbouring spin-echo peaks in a signal, and the time between two applied RF pulses, respectively. Figure 3.1 illustrates the relationships between sequence parameters, relaxation times and the FID signal.

To construct an MR image, it is necessary to determine the spatial location of the FID signal received. This is done by applying linearly varying magnetic field gradients along the three Cartesian directions (x, y and z). Depending on their axis orientation, these gradients are called G_x , G_y , and G_z . By convention the G_z gradient is used for slice selection, while the G_y and G_x

gradients are most commonly used to perform phase encoding, and readout frequency encoding, respectively. As Figure 3.1 illustrates, the slice-selection gradient is applied at the same time as each RF pulse, the phase-encoding gradient is applied anywhere between 90° and 180° RF pulses, and the frequency encoding gradient is applied during the time the echo signal is received (during the readout).

Different body tissues provide different signals, allowing distinction between various organs imaged by different MRI sequences. Water has a very long T2 time (slow energy exchange between the spins) and therefore voxels representing tissues abundant in water are bright in a T2-weighted image. On the contrary, fat tissue, which has a very efficient energy exchange, has a relatively short T2 time and therefore appears dark in T2-weighted images. T2-weighting is achieved by choosing the machine parameters such that TR is greater than T1, and TE is less than T2 of the tissue of interest. For T1-weighted images TR is chosen to be less than T1 and TE less than T2. In balanced fast field echo (B-FFE) imaging [<http://www.mr-tip.com/serv1.php>], both longitudinal and transverse magnetizations are maintained, and hence both T1 and T2 contrasts are represented in these images. The signal is especially pronounced for fluids and tissues with long T2 times.

3.2.2 MR Image Acquisition

Two different pulse sequences were used to acquire post-implant MR image volumes: a T2-weighted sequence with TE = 91 ms and TR = 4750 ms, and a B-FFE sequence with TE/TR=9.6/4.8 ms. Both image volumes were obtained for a FOV of 150 mm using a Philips Gyroscan Intera 1.5 T MRI system (Philips Medical Systems, Bothell, WA) with cardiac coil. In each case axial slices were 3 mm thick (no gap) with a pixel pitch of ~0.3 mm. Similarly to the clinical CT imaging volume, the MR imaging volume spanned a region

starting cephalad to the prostate base and extending caudad to the prostate apex. Image volumes consisted of 30 axial slices depicting the implanted prostate and surrounding pelvic tissues.

3.2.3 Image Features

Figure 3.3 shows corresponding mid-gland axial slices from T2-weighted and B-FFE MR image volumes. Prostate and rectum are clearly visualized in the center of the field of view. The intensities of corresponding structures in the two images are similar, but intensity levels in the B-FFE image are higher relative to those in the T2-weighted image. Although both images provide good contrast between tissues, the B-FFE image is much less noisy and shows a better definition of soft tissue boundaries. In addition, the signal voids associated with needle tracks (along which the implanted seeds lie) are far more obvious in the B-FFE image. Due to preservation of both longitudinal and transverse magnetization in the B-FFE pulse sequence, the B-FFE image also provides more detail within imaged structures.

3.2.4 Post-implant Dosimetry

As discussed in Section 3.1.4, most post-implant dosimetry done today is CT based. However, T2-weighted MRI images have been considered for use in post-dosimetric evaluation as well [Dubois *et al.*, 1998] as they provide good soft tissue contrast. The ability to clearly visualize tissue structure contours in these images is an important asset for accurate calculation of dosimetric indices; however, difficulty in distinguishing between the radiation sources and blood vessels, which confounds source localization, means that T2-weighted MR images alone are inadequate for post-implant analysis [Dubois *et al.*, 1997]. B-FFE images provide better distinction between needle

tracks containing radioactive sources (larger diameter voids) and blood vessels (smaller diameter voids), however, due to the continuity along the scanning axis of the former throughout the volume set it remains difficult to determine source locations precisely. Furthermore, signal voids are seen along the needle path even if no seeds are deposited after needle insertion. Considering that CT and MR images provide complimentary information, combining the images from these two modalities should provide the most accurate information for the intended post-implant dosimetry application.

3.3 Image Distortion

3.3.1 Seed Phantom

To determine the amount of scanner related spatial distortion present in the CT and MR images, we designed a simple phantom insert, shown in Figure 3.4 consisting of two Lucite plates separated by about 50 mm and immersed in a water background (see the sketch in Figure 3.5 (a)). Each plate contains a $3 \times 3 \text{ cm}^2$ grid of sixteen inactive I^{125} seeds (model OncoSeed, Medi-Physics Inc., Arlington Heights, IL). Seeds are spaced 1 cm apart and partially embedded into the plates to a depth of 0.6 mm with their length oriented in the superior-inferior (z) direction along the scanner axis. Seeds in plane 1 are numbered 1-16, while seeds in plane two have numbers 17-32 (see Figure 3.5 (b)).

We acquired CT and T2-weighted and B-FFE MR scans of this phantom and utilized MATLAB programs to analyze the images. The CT scan was performed with a Picker PQ-5000 using a conventional scan with slice thickness 3.0 mm and no inter-slice gap. The MR image sets were obtained using a Philips Gyroscan Intera 1.5 T system with cardiac coil. A T2-weighted

sequence with TE/TR=91/4750 ms was employed to acquire both axial and sagittal images of the phantom. A B-FFE sequence with TE/TR=9.6/4.8 ms was used to obtain axial images only. The slice thickness was again 3.0 mm, with no inter-slice gap.

3.3.2 Image Analysis and Results

Our analysis consisted of determining the coordinates of the center of each seed imaged, and using these measurements to calculate the 3D centroid of the full seed distribution, the x and y distances between neighbouring seeds in each plate, and the z distances between corresponding seeds in the two plates.

The algorithm used for finding seed coordinates searches for the location of the centroid of the maximum (for CT) or minimum (for MR) image intensity in a region of interest surrounding the image of each seed visible in multiple slices. The x, y, and z coordinates associated with this location are presumed to represent the center of the seed in the image volume. The coordinates of the centroid of all seeds in the phantom are determined as averages of the x, y, and z coordinates of the individual seed centroids. For further detail and a flow chart please see Figure 3.6.

To find the relative seed distribution in a single plane, we computed distances x' and y' between each seed and the center of the seed grid as the difference between individual x and y seed coordinates and the average x and y coordinates of all seeds in the plane. The distance between each seed and the grid center was calculated from:

$$D_{i,plane} = \sqrt{x_i'^2 + y_i'^2} \quad 3.5$$

These values were used together with distances z_i' between the z coordinates of each seed and the centroid of the complete distribution of 32 seeds to determine the distance between each seed and the 3D centroid, as follows:

$$D_{i,vol} = \sqrt{D_{i,plane}^2 + z_i'^2} \quad 3.6$$

The average value of this distance was found to be $D_{i,vol} = (28.4 \pm 2.4)$ mm for the CT image set, $D_{i,vol} = (26.0 \pm 2.8)$ mm for the T2-weighted MR image set, and $D_{i,vol} = (25.9 \pm 2.8)$ mm for the B-FFE MR volume. Based on phantom geometry the expected value of this distance is $D_{i,vol} = (28.5 \pm 2.5)$ mm. Note that standard deviations associated with these values reflect both the measurement error and the variations in distance between individual seeds and the centroid.

To assess the amount of distortion in each Cartesian direction separately, we computed in-plane distances (D_x and D_y) between neighbouring seeds, as well as superior-inferior distances (D_z) between collinear seeds in the two planes. These distances were computed as differences between appropriate x , y , and z seed coordinates, respectively (see Figure 3.5).

We found that for the CT image data, the average values of these measurements agreed with direct physical measurement using digital calipers ($D_x = D_y = 14.1$ mm, and $D_z = 47.7$ mm) within one standard deviation. In plane 1 these values were $D_x = (14.2 \pm 0.5)$ mm, and $D_y = (14.0 \pm 0.2)$ mm. For measurements in plane 2 and detailed data see Table 3.1. The average distance between collinear seeds was $D_z = (47.7 \pm 0.6)$ mm (see Table 3.2). Maximum differences between individual measurements and the physical distances were $\Delta_{max} = 0.9$ mm, 0.5 mm, and 0.4 mm in the x , y , and z directions respectively.

In-plane distances measured from the MR image datasets also agreed with physical values within one standard deviation, average measurements in plane 1 being $D_x = (14.2 \pm 0.3)$ mm and $D_y = (14.2 \pm 0.2)$ mm for T2-weighted (Table 3.3) and $D_x = (14.1 \pm 0.3)$ mm and $D_y = (14.0 \pm 0.3)$ mm for B-FFE (Table 3.5) volumes. However, the average D_z distances computed from the MR volumes did not agree with that found from CT, or with the physical value within one standard deviation, but instead were $D_z = (41.7 \pm 0.1)$ mm for T2-weighted MR and $D_z = (41.6 \pm 0.1)$ mm for B-FFE MR (see Tables 3.4 and 3.6). Maximum differences between experimental measurements and physical distances for T2-weighted MR image data were $\Delta_{\max} = 0.7$ mm, 0.5 mm, and 6.2 mm in the x and y direction in plane 1, and the z direction, respectively. Similarly, these differences for B-FFE MR were $\Delta_{\max} = 0.5$ mm, 0.8 mm, and 6.4 mm.

3.3.3 Discussion

With the exception of the MR-based distance measurements made in the direction of the scanner axis (Z-axis), the data obtained for the three imaging techniques of interest collectively indicate that spatial image distortion inherent to the image acquisition process is minimal (< 1 mm) for image registration volumes relevant to prostate brachytherapy. The MR Z-axis data warranted careful re-examination and interpretation in light of physical processes in play for axial images in the out-of-plane direction. There are three different effects that together are thought to contribute to the observed discrepancy between the Z-axis values measured using MRI and the physical values. They are as follows:

Invisibility of the part of a seed embedded into the plastic plate

Because of the absence of MR signal from the Lucite plates, a portion of each seed is “invisible” to the seed finding algorithm, which effectively shortens the seeds and moves the planes containing their centers towards each other. Considering that the length of seed wedged into each plate is 0.6 mm, one can expect that the distance between the two seed planes is shortened by the same amount.

Slice volume averaging effect

Ideally, the geometrically defined surface of an axial slice should coincide with the plate/background boundary. In this case the whole slice volume would ideally contain the same signal strength coming from the seeds and the background as for slices at a greater distance from the plate. If, however, a scan slice extends into the plate, mixing of the seed/background signal with the signal void from the plate would cause a reduction in seed contrast in this particular slice. This volume averaging effect makes it more difficult for the search algorithm to determine the physical extent of the seed based on the intensity distribution, and leads to further shortening of the distance between seeds in the two planes.

Extension of signal void from the plate beyond the plate surface

Similarly to the slice volume effect, additional blurring of the seed signal void can be caused by “bleeding” of the signal void from the adjacent slice. This can influence seed visibility close to the plate where the signal void from the plate extends beyond the plate’s surface, effectively shortening the visible seed.

To test the hypothesis of seed signal void foreshortening, we designed a second phantom insert (see Figure 3.7) consisting of two thin plastic tubes each holding a string of eight inactive seeds spaced (10.0 ± 0.1) mm from

each other. The tubes were placed in our water-filled phantom with the seed axis oriented in the Z direction along the scanner axis (see Figure 3.8). No seed came in contact with the plastic plates. Considering that distortions for the two MR imaging techniques were similar and that the B-FFE image provided better signal to noise ratio, we decided to acquire only B-FFE MR images of this phantom. The B-FFE sequence described in Section 3.3.1 was applied and the same MATLAB program was used to analyze the images. The average distance between adjacent seeds computed from the image data agreed with the known physical distance within one standard deviation, and had a value of (10.2 ± 0.3) mm. We also measured the distances between more widely separated seeds, as well as the distance between the Lucite plates holding the tubes. We found that the difference between measured and physical distances were ≤ 0.8 mm in all cases. These results strongly suggest that the seed signal void foreshortening in the Z direction observed for our original phantom is due to the effects described above, and is not due to spatial distortion or miscalibration along the MR scanner axis. See Tables 3.7 and 3.8 for details.

3.3.4 Conclusions

Scanner related spatial distortions in both CT and MR images across the volume of interest in our phantom ($\sim 45 \text{ cm}^3$) are minimal. In-plane distances between neighbouring seeds and between each seed and the plane center determined from the MR and CT image sets are in good agreement with each other and with physical measurements, and have similar standard deviations. The seed separation measurement error observed with our original seed phantom in the sup-inf (scanner axis) direction in both T2-weighted and B-FFE MR images is most likely caused by a combination of the slice volume effect and signal void “bleeding” from the plate, resulting in an average discrepancy of about 10% in seed-to-seed and seed-to-centroid distances

between measured and physical values. A modification to the seed phantom made to avoid these effects subsequently yielded good agreement between image-derived and physical distances in the sup-inf direction.

Plane 1

seed #	Ypixel	Xpixel	Adj.seedsX	Dx[pix]	Dx[mm]	Adj.seedsY	Dy[pix]	Dy[mm]
1	262.3	226.0	s1-s5	18.0	14.1	s2-s3	18.2	14.2
2	253.5	235.5	s5-s12	17.0	13.3	s4-s5	18.0	14.1
3	271.7	234.3	s12-s16	19.0	14.8	s5-s6	18.0	14.1
4	245.0	244.0	s2-s8	18.0	14.1	s7-s8	17.5	13.7
5	263.0	244.0	s8-s14	18.0	14.1	s8-s9	18.5	14.4
6	281.0	243.0	s4-s11	19.0	14.8	s9-s10	18.0	14.0
7	237.0	254.0	s3-s9	17.7	13.8	s11-s12	18.0	14.0
8	254.5	253.5	s9-s15	18.0	14.1	s12-s13	17.7	13.8
9	273.0	252.0	s6-s13	18.3	14.3	s14-s15	18.0	14.1
10	291.0	252.0	average	18.1	14.1	average	18.0	14.0
11	246.0	263.0	σ	0.6	0.5	σ	0.3	0.2
12	264.0	261.0	$D_{x,physical}$	18.1	14.1	$D_{x,physical}$	18.1	14.1
13	281.7	261.3	Δ_{max}	1.1	0.9	Δ_{max}	0.6	0.5
14	255.0	271.5						
15	273.0	270.0						
16	265.0	280.0						

Plane 2

seed #	Ypixel	Xpixel	Adj.seedsX	Dx[pix]	Dx[mm]	Adj.seedsY	Dy[pix]	Dy[mm]
17	262.5	225.5	s17-s21	18.5	14.5	s18-s19	17.0	13.3
18	254.0	235.0	s21-s28	18.0	14.1	s20-s21	18.0	14.1
19	271.0	234.0	s28-s32	18.0	14.0	s21-s22	18.0	14.1
20	245.0	244.0	s18-s24	18.0	14.0	s23-s24	18.0	14.1
21	263.0	244.0	s24-s30	19.0	14.8	s24-s25	17.5	13.7
22	281.0	244.0	s20-s27	18.0	14.1	s25-s26	18.5	14.4
23	236.0	253.5	s19-s25	18.5	14.4	s27-s28	18.0	14.1
24	254.0	253.0	s25-s31	17.5	13.7	s28-s29	18.0	14.0
25	271.5	252.5	s22-s29	18.0	14.1	s30-s31	18.0	14.1
26	290.0	251.5	average	18.2	14.2	average	17.9	14.0
27	245.0	262.0	σ	0.4	0.3	σ	0.4	0.3
28	263.0	262.0	$D_{x,physical}$	18.1	14.1	$D_{x,physical}$	18.1	14.1
29	281.0	262.0	Δ_{max}	0.6	0.5	Δ_{max}	1.1	0.8
30	255.0	272.0						
31	273.0	270.0						
32	263.0	280.0						

Table 3.1 In-plane distances between adjacent seeds in the CT image volume.

Plane 1 seed #	Z [slice]	Plane 2 seed #	Z [slice]	Collinear seeds	Dz [pix]	Dz [mm]
1	7.0	17	22.5	s1-s17	15.5	46.6
2	6.5	18	22.5	s2-s18	16.0	48.1
3	7.0	19	22.5	s3-s19	15.5	46.6
4	6.5	20	22.5	s4-s20	16.0	48.1
5	6.5	21	22.5	s5-s21	16.0	48.1
6	7.0	22	22.5	s6-s22	15.5	46.6
7	6.5	23	22.5	s7-s23	16.0	48.1
8	6.5	24	22.5	s8-s24	16.0	48.1
9	6.5	25	22.5	s9-s25	16.0	48.1
10	6.5	26	22.5	s10-s26	16.0	48.1
11	6.5	27	22.5	s11-s27	16.0	48.1
12	6.5	28	22.5	s12-s28	16.0	48.1
13	7.0	29	22.5	s13-s29	15.5	46.6
14	6.5	30	22.5	s14-s30	16.0	48.1
15	6.5	31	22.5	s15-s31	16.0	48.1
16	6.5	32	22.5	s16-s32	16.0	48.1
average					15.9	47.7
σ					0.2	0.6
$D_{z, \text{physical}}$					15.9	47.7
Δ_{max}					0.1	0.4

Table 3.2 Distances between collinear seeds in the two seed planes in the CT image volume.

Plane 1

seed #	Xpixel	Ypixel	Adj.seedsX	Dx[pix]	Dx[mm]	Adj.seedsY	Dy[pix]	Dy[mm]
1	203.0	269.0	s1-s5	49.1	14.3	s2-s3	48.9	14.3
2	228.0	245.0	s5-s12	47.9	14.0	s4-s5	48.9	14.3
3	227.0	293.9	s12-s16	48.0	14.0	s5-s6	48.0	14.0
4	254.0	221.0	s2-s8	48.0	14.0	s7-s8	47.9	14.0
5	252.1	269.9	s8-s14	50.9	14.9	s8-s9	48.0	14.0
6	251.0	317.9	s4-s11	48.0	14.0	s9-s10	49.0	14.3
7	279.0	198.0	s3-s9	49.0	14.3	s11-s12	50.0	14.6
8	276.1	245.9	s9-s15	49.0	14.3	s12-s13	48.0	14.0
9	276.1	293.9	s6-s13	48.0	14.0	s14-s15	50.0	14.6
10	274.0	342.9	average	48.7	14.2	average	48.7	14.2
11	302.0	222.0	σ	1.0	0.3	σ	0.8	0.2
12	300.1	271.9	$D_{x,physical}$	48.4	14.1	$D_{x,physical}$	48.4	14.1
13	299.0	319.9	Δ_{max}	2.5	0.7	Δ_{max}	1.5	0.4
14	327.0	246.0						
15	325.1	296.0						
16	348.1	273.0						

Plane 2

seed #	Xpixel	Ypixel	Adj.seedsX	Dx[pix]	Dx[mm]	Adj.seedsY	Dy[pix]	Dy[mm]
17	204.0	268.0	s17-s21	48.1	14.0	s18-s19	48.0	14.0
18	229.0	244.0	s21-s28	47.0	13.7	s20-s21	50.9	14.9
19	227.0	292.0	s28-s32	49.0	14.3	s21-s22	47.0	13.7
20	254.0	218.0	s18-s24	49.0	14.3	s23-s24	50.0	14.6
21	252.1	269.0	s24-s30	47.0	13.7	s24-s25	46.9	13.7
22	251.0	315.9	s20-s27	48.0	14.0	s25-s26	49.0	14.3
23	278.0	196.0	s19-s25	49.1	14.3	s27-s28	47.9	14.0
24	278.0	246.0	s25-s31	48.0	14.0	s28-s29	49.0	14.3
25	276.1	292.9	s22-s29	49.1	14.3	s30-s31	49.0	14.3
26	274.0	341.9	average	48.3	14.1	average	48.6	14.2
27	302.0	222.0	σ	0.8	0.2	σ	1.3	0.4
28	299.1	269.9	$D_{x,physical}$	48.4	14.1	$D_{x,physical}$	48.4	14.1
29	300.1	318.9	Δ_{max}	1.4	0.4	Δ_{max}	2.5	0.7
30	325.0	246.0						
31	324.1	294.9						
32	348.1	272.0						

Table 3.3 In-plane distances between adjacent seeds in the T2-weighted MR image volume.

Plane 1 seed #	Z [slice]	Plane2 seed #	Z [slice]	Collinear seeds	Dz [pix]	Dz [mm]
1	5.9	17	19.8	s1-s17	13.9	41.8
2	5.9	18	19.8	s2-s18	13.9	41.7
3	5.9	19	19.8	s3-s19	13.9	41.8
4	5.9	20	19.8	s4-s20	13.9	41.6
5	5.9	21	19.8	s5-s21	13.9	41.7
6	5.9	22	19.8	s6-s22	13.9	41.8
7	6.0	23	19.8	s7-s23	13.9	41.6
8	5.9	24	19.8	s8-s24	13.9	41.7
9	5.9	25	19.8	s9-s25	13.9	41.7
10	5.9	26	19.8	s10-s26	13.9	41.8
11	6.0	27	19.8	s11-s27	13.9	41.6
12	6.0	28	19.8	s12-s28	13.8	41.5
13	5.9	29	19.8	s13-s29	13.9	41.7
14	6.0	30	19.8	s14-s30	13.9	41.6
15	6.0	31	19.8	s15-s31	13.9	41.6
16	6.0	32	19.8	s16-s32	13.8	41.5
average					13.9	41.7
σ					0.0	0.1
$D_{z,physical}$					15.9	47.7
Δ_{max}					2.1	6.2

Table 3.4 Distances between collinear seeds in the two seed planes in the T2-weighted MR image volume.

Plane 1

seed #	Xpixel	Ypixel	Adj.seedsX	Dx[pix]	Dx[mm]	Adj.seedsY	Dy[pix]	Dy[mm]
1	203.1	269.7	s1-s5	48.3	14.1	s2-s3	48.9	14.3
2	228.2	245.7	s5-s12	48.2	14.1	s4-s5	47.8	14.0
3	226.2	294.6	s12-s16	47.8	14.0	s5-s6	48.0	14.0
4	253.3	222.8	s2-s8	47.2	13.8	s7-s8	46.7	13.6
5	251.4	270.6	s8-s14	49.0	14.3	s8-s9	47.9	14.0
6	249.0	318.6	s4-s11	47.2	13.8	s9-s10	49.2	14.4
7	278.3	199.9	s3-s9	49.0	14.3	s11-s12	48.9	14.3
8	275.4	246.6	s9-s15	47.0	13.7	s12-s13	45.8	13.4
9	275.3	294.5	s6-s13	50.3	14.7	s14-s15	46.8	13.7
10	272.9	343.7	average	48.2	14.1	average	47.8	14.0
11	300.5	223.8	σ	1.1	0.3	σ	1.2	0.3
12	299.6	272.7	$D_{x,physical}$	48.4	14.1	$D_{x,physical}$	48.4	14.1
13	299.3	318.6	Δ_{max}	1.9	0.5	Δ_{max}	2.6	0.8
14	324.4	249.0						
15	322.2	295.7						
16	347.4	273.0						

Plane 2

seed #	Xpixel	Ypixel	Adj.seedsX	Dx[pix]	Dx[mm]	Adj.seedsY	Dy[pix]	Dy[mm]
17	203.1	266.9	s17-s21	48.3	14.1	s18-s19	48.0	14.0
18	228.1	243.9	s21-s28	48.1	14.0	s20-s21	48.7	14.2
19	227.1	291.8	s28-s32	48.1	14.0	s21-s22	47.0	13.7
20	253.1	219.9	s18-s24	48.3	14.1	s23-s24	47.7	13.9
21	251.4	268.6	s24-s30	48.0	14.0	s24-s25	47.2	13.8
22	250.2	315.6	s20-s27	48.1	14.1	s25-s26	47.5	13.9
23	277.1	197.9	s19-s25	48.4	14.1	s27-s28	47.7	13.9
24	276.4	245.7	s25-s31	48.1	14.1	s28-s29	48.8	14.2
25	275.5	292.9	s22-s29	49.3	14.4	s30-s31	47.7	13.9
26	273.0	340.4	average	48.3	14.1	average	47.8	14.0
27	301.2	221.8	σ	0.4	0.1	σ	0.6	0.2
28	299.5	269.6	$D_{x,physical}$	48.4	14.1	$D_{x,physical}$	48.4	14.1
29	299.5	318.3	Δ_{max}	0.9	0.3	Δ_{max}	1.5	0.4
30	324.4	246.8						
31	323.6	294.5						
32	347.5	271.9						

Table 3.5 In-plane distances between adjacent seeds in the B-FFE MR image volume.

Plane 1 seed #	Z [slice]	Plane2 seed #	Z [slice]	Collinear seeds	Dz [pix]	Dz [mm]
1	5.9	17	19.8	s1-s17	13.9	41.7
2	6.0	18	19.8	s2-s18	13.9	41.6
3	6.0	19	19.8	s3-s19	13.9	41.7
4	6.0	20	19.8	s4-s20	13.9	41.6
5	6.0	21	19.8	s5-s21	13.8	41.5
6	5.9	22	19.9	s6-s22	13.9	41.7
7	6.0	23	19.8	s7-s23	13.8	41.5
8	6.0	24	19.9	s8-s24	13.9	41.6
9	6.0	25	19.8	s9-s25	13.8	41.5
10	6.0	26	19.8	s10-s26	13.9	41.6
11	6.0	27	19.8	s11-s27	13.8	41.5
12	6.1	28	19.8	s12-s28	13.8	41.3
13	6.0	29	19.9	s13-s29	13.9	41.6
14	6.0	30	19.9	s14-s30	13.8	41.5
15	6.0	31	19.8	s15-s31	13.8	41.4
16	6.0	32	19.9	s16-s32	13.8	41.5
average					13.9	41.6
σ					0.0	0.1
$D_{z,physical}$					15.9	47.7
Δ_{max}					2.1	6.4

Table 3.6 Distances between collinear seeds in the two seed planes in the B-FFE MR image volume.

Neighbouring seeds

String #	Seed #	Seed 1	Seed2	Dist _{meas} [pix]	Dist _{meas} [mm]
1	1 and 2	436.0	402.0	34.0	10.0
2	1 and 2	428.0	394.0	34.0	10.0
1	2 and 3	402.3	366.0	36.3	10.6
2	2 and 3	394.0	360.0	34.0	10.0
1	3 and 4	360.0	324.0	36.0	10.6
2	3 and 4	359.0	324.0	35.0	10.2
1	4 and 5	328.0	294.0	34.0	10.0
2	4 and 5	329.0	295.0	34.0	10.0
1	5 and 6	295.0	258.3	36.7	10.8
2	5 and 6	293.0	257.1	35.9	10.5
1	6 and 7	258.0	225.1	32.9	9.6
2	6 and 7	256.0	221.0	35.0	10.3
1	7 and 8	227.0	191.0	36.0	10.6
2	7 and 8	232.0	198.0	34.0	10.0
average					10.2
σ					0.3
Dist _{phys}					10.0

Non-neighbouring seeds

String #	Seed #	Seed 1	Seed 2	Dist _{meas} [pix]	Dist _{meas} [mm]	Dist _{phys} [mm]	Diff _{abs} [mm]	%Diff
1	1 and 8	434.0	193.0	241.0	70.6	70.0	0.6	0.9
2	1 and 8	428.0	190.0	238.0	69.7	70.0	0.3	0.4
1	2 and 8	395.0	191.0	204.0	59.8	60.0	0.2	0.4
2	2 and 8	392.0	189.0	203.0	59.5	60.0	0.5	0.9
1	3 and 7	362.0	226.0	136.0	39.8	40.0	0.2	0.4
2	3 and 7	369.0	230.0	139.0	40.7	40.0	0.7	1.8
1	4 and 6	329.0	260.2	68.8	20.2	20.0	0.2	0.8
2	4 and 6	335.0	266.1	68.9	20.2	20.0	0.2	0.9
average							0.4	0.8

Table 3.7 Sup-inf (Z direction) distances between seeds in ribbons (slice volume effects absent) measured in the B-FFE MR image volume.

Plate 1	Plate 2	Dist _{meas} [pix]	Dist _{meas} [mm]	Dist _{phys} [mm]	Diff _{abs} [mm]	%Diff
181.0	440.0	259.0	75.6	76.1	0.5	0.6
181.1	440.0	258.9	75.6	76.1	0.5	0.7
181.0	440.0	259.0	75.6	76.1	0.5	0.6
181.0	440.0	259.0	75.6	76.1	0.5	0.6
182.0	441.0	259.0	75.6	76.1	0.5	0.6
182.0	440.0	258.0	75.3	76.1	0.8	1.0
181.0	440.0	259.0	75.6	76.1	0.5	0.6
181.0	440.0	259.0	75.6	76.1	0.5	0.6
181.0	440.0	259.0	75.6	76.1	0.5	0.6
181.0	440.0	259.0	75.6	76.1	0.5	0.6
average					0.5	0.7

Table 3.8 Distances between the Lucite plates holding the seed ribbons measured in the B-FFE MR image volume.

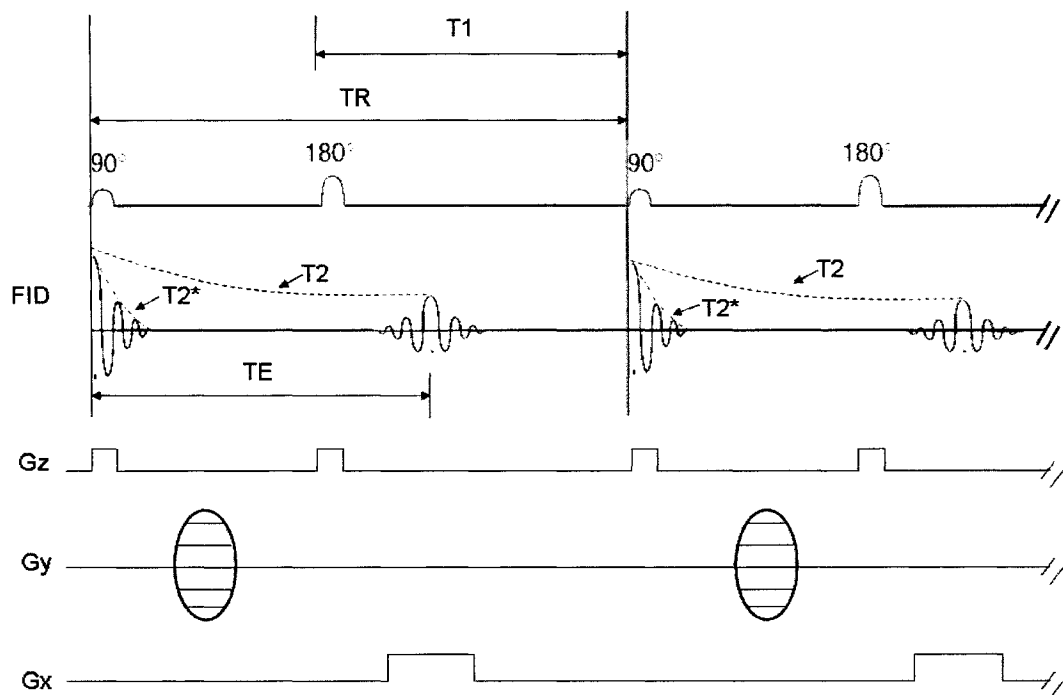


Figure 3.1 Typical spin-echo MR imaging timing diagram, illustrating the relationship between spin flip pulses, the FID signal, and the imaging gradients.

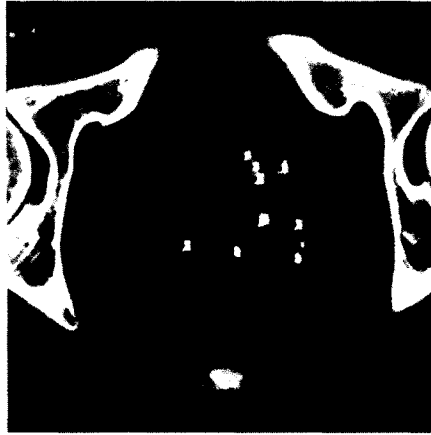


Figure 3.2 CT slice of a prostate implant near the base of the prostate gland. Note the difference in intensities of structures imaged: bones and implanted seeds appear brightest, air in the rectum darkest.

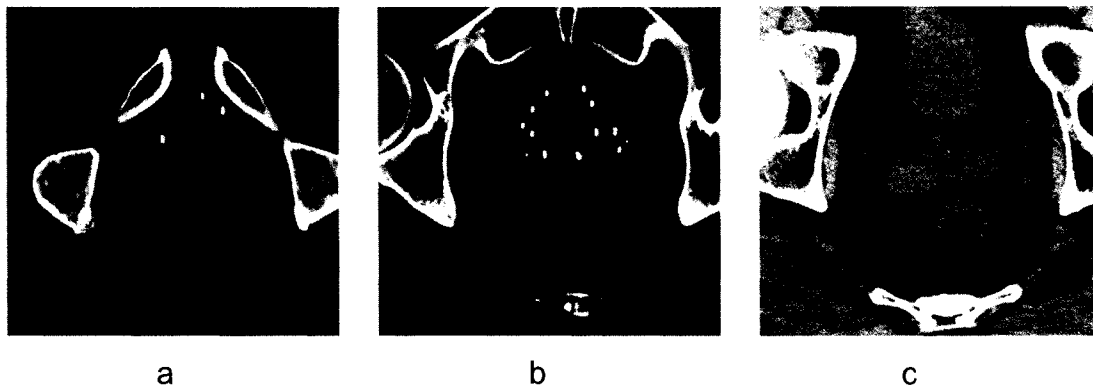


Figure 3.3 CT image volume of a prostate implant: a) caudal slice, b) mid-gland slice, c) cranial slice.

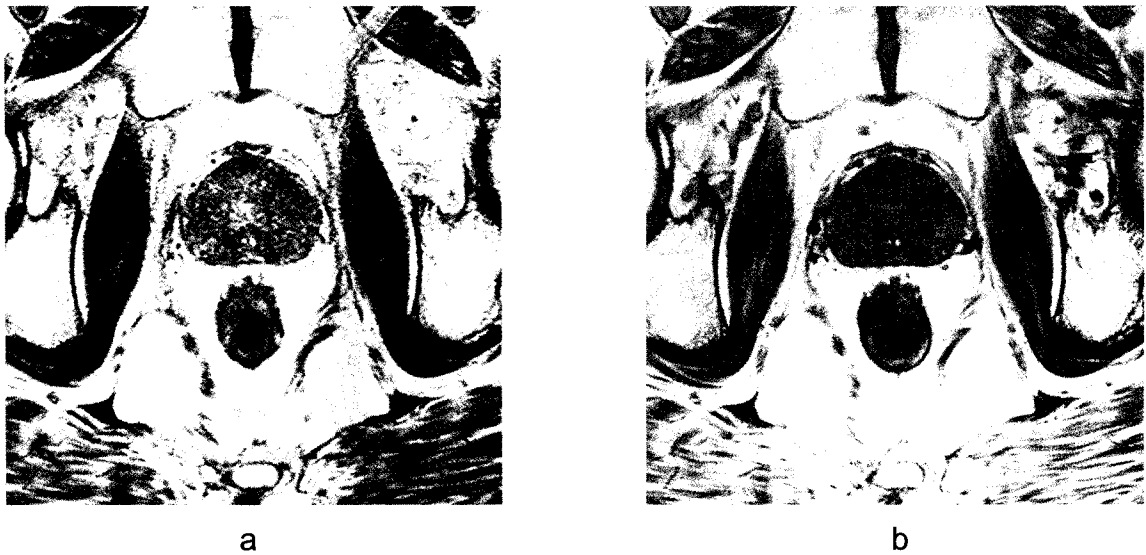


Figure 3.4 a) Axial slice from T2-weighted MR image volume depicting post-implant prostate near mid-gland; b) corresponding axial slice from B-FFE MR image volume.

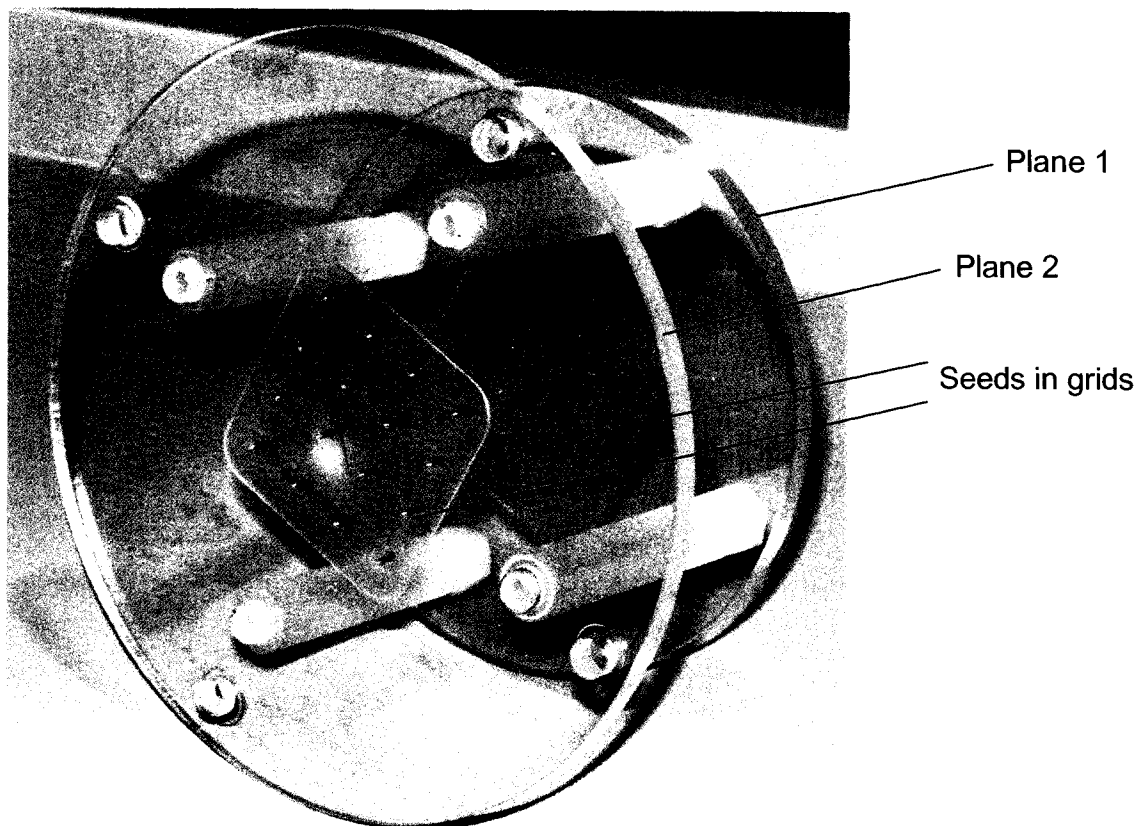


Figure 3.5 A photograph of the phantom insert consisting of two collinear seed grids separated by ~50 mm.

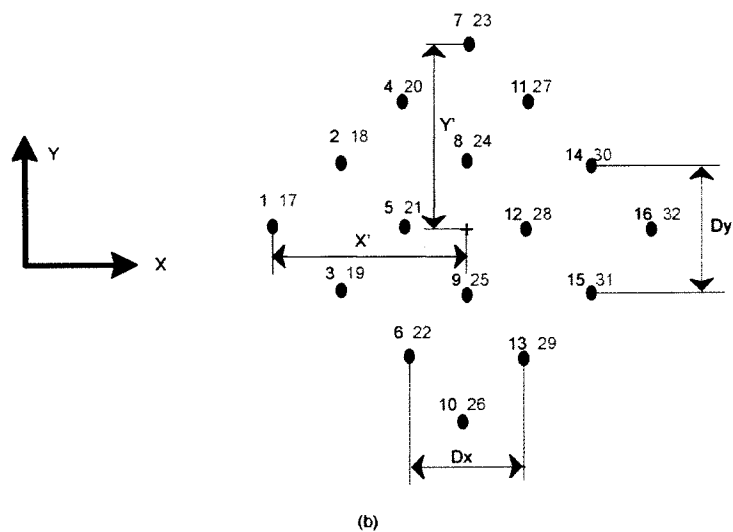
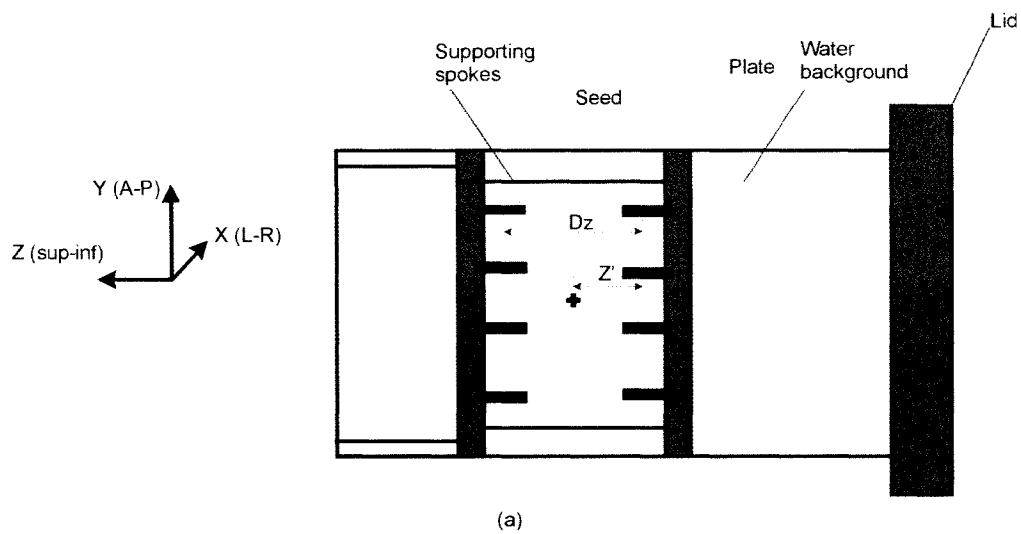


Figure 3.6 a) Sketch of the water-filled phantom used for spatial distortion measurements (note the orientation of the seed phantom insert); b) Grid illustrating seed locations in the two planes.

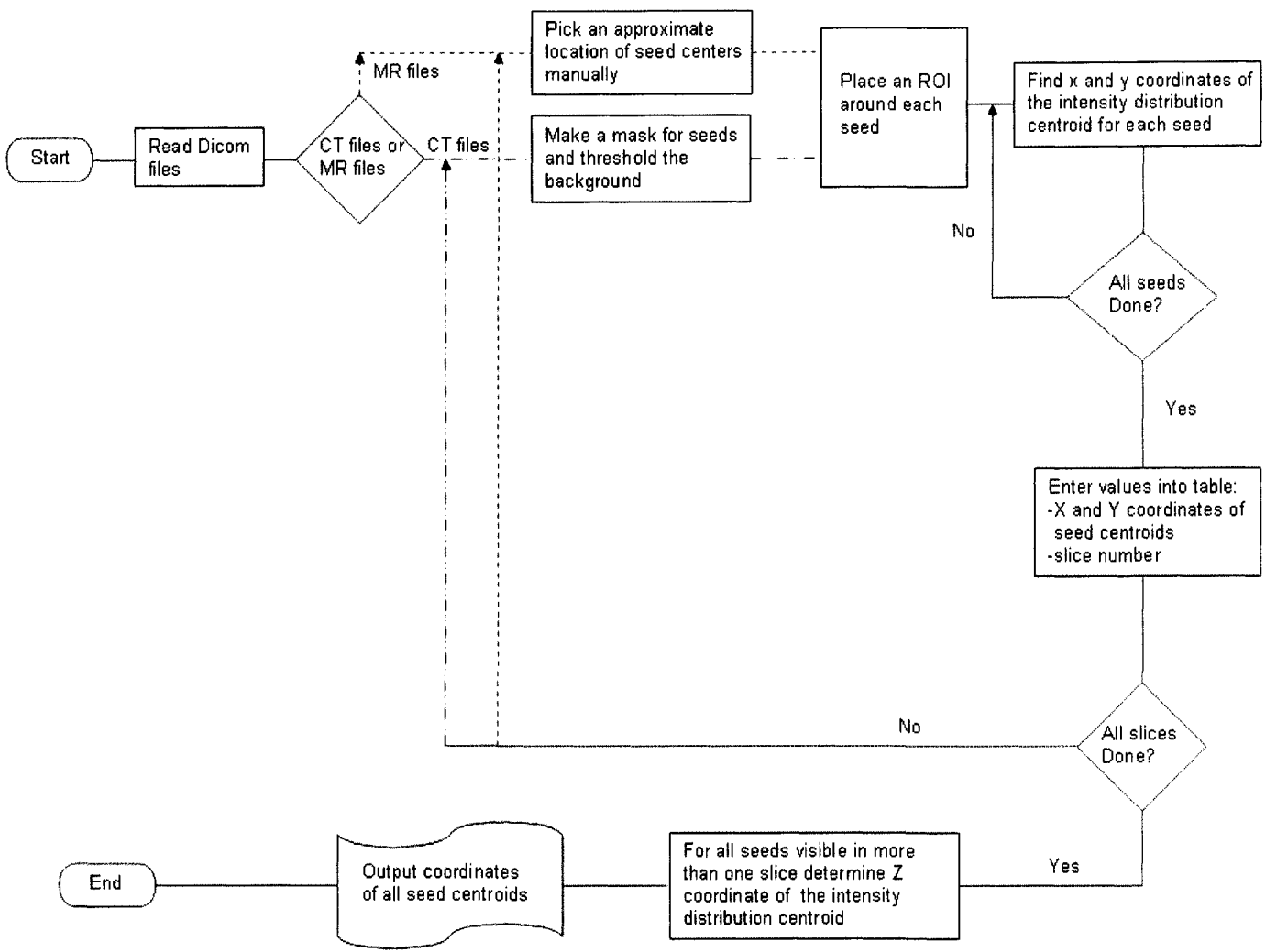


Figure 3.7 Graphical representation of the algorithm used for finding centroid locations of seeds in the grid inserted into the water phantom.

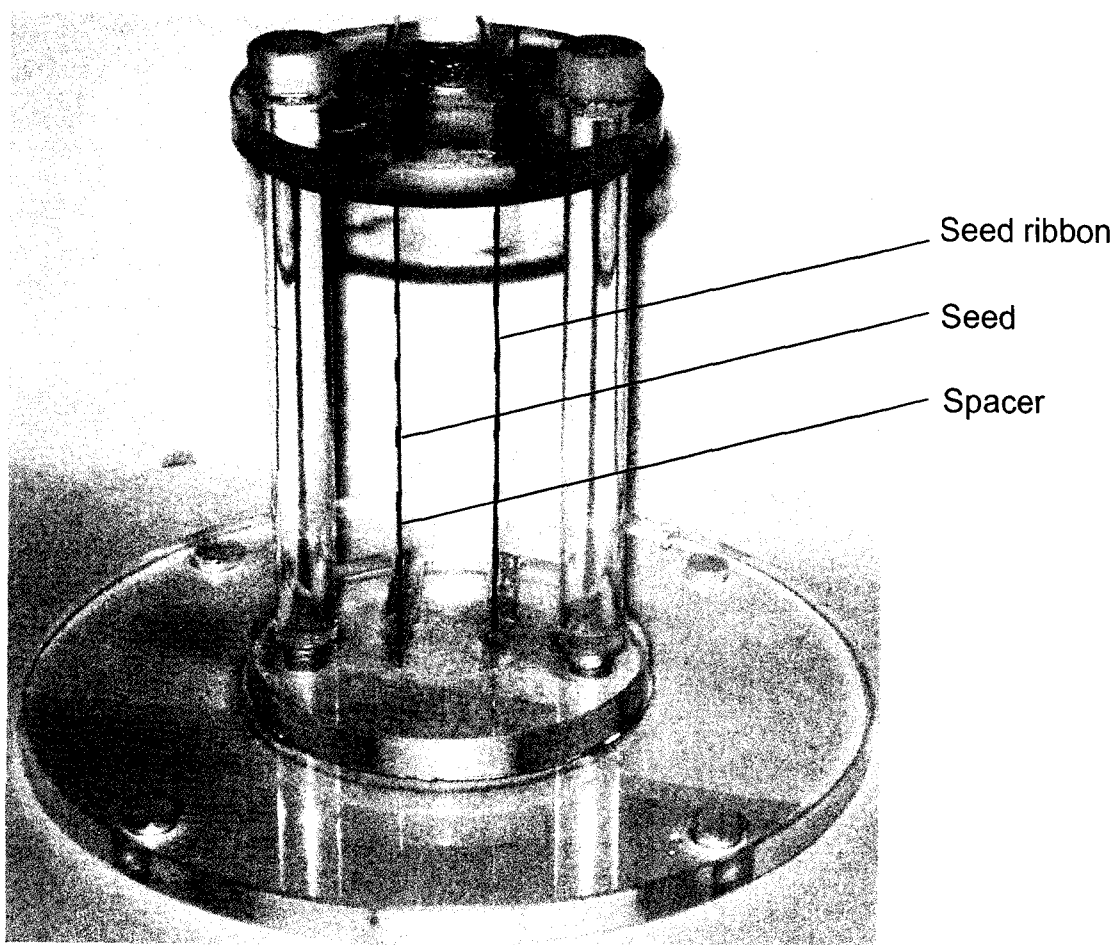


Figure 3.8 Photograph of a seed ribbon insert consisting of two parallel plastic tubes, containing evenly spaced seeds, used for assessing the partial volume effect along the MR scanning axis.

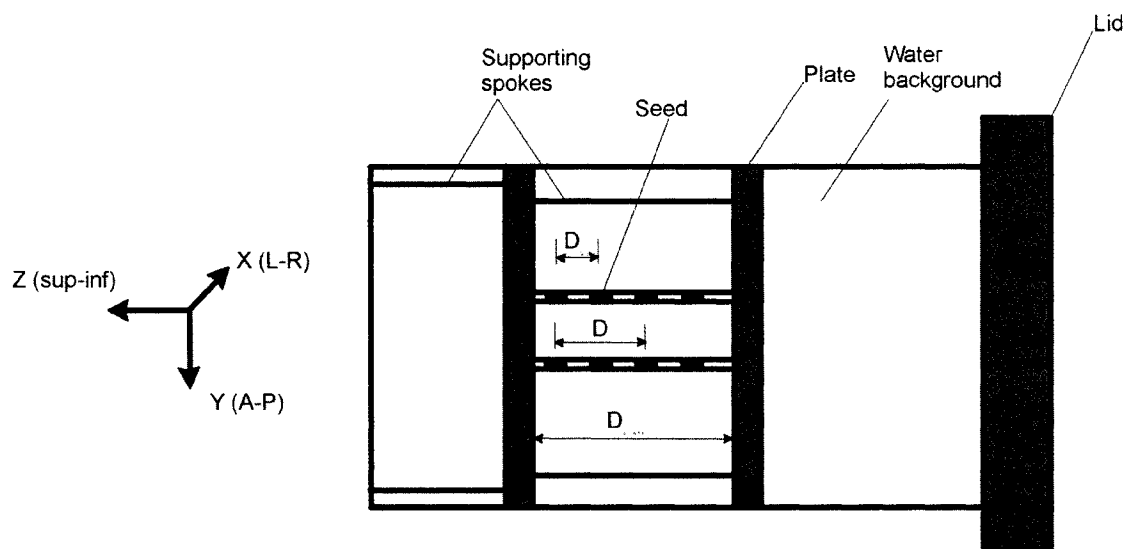


Figure 3.9 Sketch of the cylindrical container containing the seed ribbon insert immersed in the water background (note the orientation of the seeds with respect to the scanner axis).

3. 4 References

1. Bushberg J. T., Seibert J. A., Leidholdt E. M. Jr., Boone J. M., "The Essential Physics of Medical Imaging", 2nd ed., Lippincott Williams & Wilkins, Philadelphia, (2002)
2. Dubois D. F., Prestidge B. R., Hotchkiss L. A., Bice W. S., Prete J. J., Source localization following permanent transperineal prostate interstitial brachytherapy using magnetic resonance imaging, *International Journal of Radiation Oncology, Biology, Physics*, 39(5), 1037-1041 (1997)
3. Dubois D. F., Prestidge B. R., Hotchkiss L. A., Prete J. J., Bice W. S., Intraobserver and interobserver variability of MR-imaging and CT-derived prostate volumes after transperineal interstitial permanent prostate brachytherapy, *Radiology*, 207, 785-789 (1998)
4. Nag S., Bice W., DeWyngaert K., Prestidge B., Stock R., Yu Y., The American Brachytherapy Society recommendations for permanent prostate brachytherapy postimplant dosimetric analysis, *International Journal of Radiation Oncology, Biology, Physics*, 46(1), 221-230 (2000)
5. Seeram E., "Computed Tomography, physical principles, clinical applications and quality control", 2nd ed., W. B. Saunders Company, Philadelphia, (2001)

6. Stock R. G., Stone N. N., Importance of post-implant dosimetry in permanent prostate brachytherapy, *European Urology*, 41(4), 434-439 (2002)
7. Yu Y., Anderson L. L., Zuofeng L., Mellenberg D. E., Nath R., Schell M. C., Waterman F. M., Wu A., Blasko J. C., Permanent prostate seed implant brachytherapy: Report of the American Association of Physicists in Medicine Task Group No. 64, *Medical Physics*, 26(10), 2054-2073 (1999)
8. <http://www.mr-tip.com/serv1.php>

CHAPTER 4

4 REGISTRATION APPROACHES FOR CT - MR PROSTATE IMPLANT IMAGES

4.1 Introduction

Post-implant dosimetry for permanent prostate implants yields an estimate of the dose distribution delivered to the patient based on measured, rather than planned, radioactive source positions. To achieve meaningful post-implant dosimetry analysis, the sources must be clearly identifiable and their positions within the patient anatomy relative to the target volume and critical structures must be known precisely. As discussed in Section 1.2.2.3.1 neither CT nor MR images alone provide clear visualization of both the seeds and the anatomy, and therefore, neither modality is fully adequate for post-implant dosimetry. Registration of CT and MR datasets combines the information from both modalities, providing good visualization of all the structures of interest in a joint image set.

CT-MR registration of prostate implant images has been an increasingly active topic of research in the medical physics community during the past decade. Some of the methods that researchers have used to attempt registration of CT-MR post-implant datasets include:

- matching anatomical landmarks, such as bones [Kagawa *et al.*, 1997, Servois *et al.*, 2003] and bladder base and urethra [Amdur *et al.*, 1999];
- matching seeds [Servois *et al.*, 2003, McLaughlin *et al.*, 2004, Roberson *et al.*, 2005], and

- using the mutual information technique [McLaughlin *et al.*, 2004, Roberson *et al.*, 2005].

Prostate mobility with respect to other anatomical structures introduces problems in landmark-based registration [Servois *et al.*, 2003], while seed matching is a time-consuming process that requires identification of corresponding seed pairs in the CT and MR datasets [Roberson *et al.*, 2005]. By comparison, registration based on the mutual information technique is a largely automated procedure that allows efficient use of a relatively large amount of image data.

In their 2004 paper McLaughlin *et al.* reported on an MR-axial to CT-axial registration process based on mutual information and a 3D rigid-body transformation (3 translations and 3 rotations). Successful registration, with an average overall uncertainty of 1.4 mm, was consistently achieved only by cropping the MR images in such a way that the volume of interest included minimal pubic bone anteriorly and some rectum posteriorly. They found that “prostate-only registration did not result in a successful end point because the information in the prostate was not sufficient to prevent large rotation angles”.

Considering that the position of the prostate relative to adjoining anatomical structures (bones, rectum, etc.) may be different in CT and MR image sets due to the time interval between scans and the difference in scan environments [Van Herk *et al.*, 1995 and Parker *et al.*, 2003], it may be advantageous to find a method that will enable mutual information-based prostate-only registration. In this chapter we describe a novel hybrid registration algorithm that is completed in two stages. The first stage involves obtaining a transformation to parallelize straight lines fit to corresponding features running primarily in the sup-inf (Z) direction in the CT and MR image volumes. The second stage consists of applying a normalized mutual information (NMI) algorithm to obtain the remaining relative X, Y and Z

translations and Z-axis rotation required to complete the 3D rigid-body registration process. Limiting rotational degrees of freedom to rotation about the Z-axis only for NMI is expected to provide an improved opportunity to achieve automated prostate-only registration of CT and MR volume sets. Application and assessment of the new algorithm are illustrated here for three clinical cases.

4.2 Methods and Materials

Our initial attempts to register clinical CT and MR datasets with a rigid-body transformation using an NMI algorithm available in the Analyze 5.0 (AnalyzeDirect Inc., Lenexa, KS) biomedical imaging software package and allowing six degrees of freedom proved to be unreliable. To study this problem, we used MATLAB (MathWorks Inc., Version 7.1, Natick, MA) code to build simulated CT and MR (T2-weighted and B-FFE) image volumes of an implant, so that we could directly control image content and features. Furthermore, considering that it is possible to observe the positions of seeds (CT) and needle tracks (MR) in the axial slices of post-implant clinical images, we postulated that it may be possible to determine relative rotations about the X and Y imaging axes by independent means prior to NMI registration. Knowing these angles would eliminate two rotational degrees of freedom, which are associated with the lower information density sagittal (Y-Z) and coronal (X-Z) planes, from the NMI registration process. A proposed approach to this task is the feature lines method described in Section 4.2.4, wherein a clearly identifiable seed train/needle track is represented as a straight line along the average direction of the train/track. Such a line can be obtained as the best fit, in 3D space, to seed or needle track positions extracted from the axial slices comprising a CT or MR image volume, respectively. Determining the transformation that parallelizes a corresponding pair of feature lines yields the required relative rotations about the X and Y imaging axes.

4.2.1 Simulated Datasets

All simulated datasets consisted of thirteen 3 mm thick axial slices containing a geometrical solid prostate (~32 cc ellipsoid) centered in the volume, a uniform background, and blurred images of seeds (CT) or seed voids (MR). A total of 20 simulated seeds/seed voids were grouped into 4 trains (5 seeds per train), each running parallel to the Z axis, with seed lengths also oriented in the Z direction. The voxel dimensions of our simulated datasets, $(0.29 \times 0.29 \times 3.0) \text{ mm}^3$, corresponded to those of the clinical images. The intensities (pixel values) of objects in the simulated datasets were selected to correspond approximately to the average intensities of the same objects in the clinical datasets, and are given in Table 4.1. Poisson noise was optionally included in all simulated datasets. Figure 4.1 shows a volume rendering of a simulated CT dataset, for illustration purposes.

4.2.2 Clinical Datasets

Clinical CT and MR image volumes for three patients were acquired approximately 4 weeks post-implant using a 15.0 cm field of view. The CT volume set was acquired using a Picker PQ-5000 scanner (Philips Medical Systems, Bothell, WA) applying a standard, non-helical scan with 3.0 mm slice thickness and ~0.3 mm pixel pitch. Two different pulse sequences were used to acquire a set of axial MR images: a T2-weighted sequence with TE/TR=91/4750 ms and a B-FFE sequence with TE/TR=9.6/4.8 ms [Bushberg *et al.*, 2002]. Both MR volumes were obtained using a Philips Gyroscan Intera 1.5 T MRI system (Philips Medical Systems, Bothell, WA) with cardiac coil. In each case axial slices were 3 mm thick with no gap between them and pixel pitches were again ~0.3 mm. As illustrated in Figure 4.2, a B-FFE image provides better visualization of needle tracks and is less noisy than a T2-weighted image, in which needle tracks are hard to distinguish from blood

vessels. Therefore, we decided to use B-FFE MR volumes in our analysis of clinical datasets.

4.2.3 Normalized Mutual Information (NMI) Algorithm

The formulation of the NMI algorithm that we used for registration of both simulated and clinical datasets is described in Section 1.3.4.3 of this thesis. The registration process consists of two steps: transformation and fusion. During the transformation step the algorithm performs trial translations and rotations (and possibly other operations such as scaling) of the match image, in order to transform its coordinate system into the coordinate system of the base image. In the search process, the algorithm calculates the information content of each image and of the overlap region. It then uses these values to evaluate NMI in the transformed image. The algorithm does this iteratively, comparing the new value with the old one until it finds a maximum value of NMI, which ideally should occur when the images are well matched. In this circumstance the amount of shared information in the individual images is maximized, or equivalently, the information content in the combined image is minimized. To register image datasets according to the NMI measure we utilized Analyze 5.0 (AnalyzeDirect Inc., Lenexa, KS) software described in detail in Section 2.3.1 of this thesis.

4.2.4 Feature Lines Method

Given appropriate scaling of two image volumes to be registered, a general rigid-body transformation involves 3 translations and 3 rotations in Cartesian coordinates. For CT and MR image volumes acquired as axial slices having a thickness of several millimeters, determination of rotation angles

about the X and Y axes for registration purposes in the prostate implant application is problematic, because:

- i) voxel resolution in the Z direction is typically ~10 times poorer than it is in the X-Y axial plane (~ 3 mm slice thickness vs. ~0.3 mm pixel pitch); and
- ii) the seed-bearing prostate gland and surrounding soft tissues we wish to register in CT and MR do not present any large, high-contrast features that could facilitate the determination of these rotations.

Therefore, prior to attempting registration of these image sets using an intensity-based algorithm such as NMI, it may be advantageous to determine the required rotations about the Z and Y axes by independent means.

For implanted prostate glands, the X and Y axis rotation angles required for registration can in theory be determined from corresponding features in CT and MR datasets that run primarily in the Z direction. Suitable features might be visible needle tracks (MR) or seeds (CT), and one can determine their path in 3D space by finding the location of their centroids in the axial slices of the image volume. If features are identified as seed trains (CT) and needle tracks (MR), then feature lines can be obtained by fitting the points $(x_i(z_i), y_i(z_i))$ at the centroid locations to straight lines. Each feature line can be expressed by a pair of equations with independent variable z : $x^{\text{fit}} = m_x z + b_x$ and $y^{\text{fit}} = m_y z + b_y$. Rotation angle θ_y (see Figure 4.3 for illustration), which represents the Y-axis rotation of the feature line with respect to the Z direction of the imaging coordinate system, can be determined from the slope m_x , and similarly, rotation angle θ_x can be determined from the slope m_y , according to Equation 4.1.

$$\theta_{y,x}^{CT,MR} = \tan^{-1}(m_{x,y}^{CT,MR}) \quad 4.1$$

Applying a rotation $R_y(-\theta_y^{MR})$ to the MR (match) image volume will make a feature line in this volume parallel to the Y-Z imaging plane. A rotation $R_y(-\theta_y^{CT})$ will do likewise for the corresponding feature line in the CT (base) image volume. In matrix form, this rotation for the two modalities, $k = CT, MR$, can be written as:

$$R_y(\theta_y^{(k)}) = \begin{pmatrix} \cos \theta_y^{(k)} & \mathbf{0} & -\sin \theta_y^{(k)} \\ \mathbf{0} & \mathbf{1} & \mathbf{0} \\ \sin \theta_y^{(k)} & \mathbf{0} & \cos \theta_y^{(k)} \end{pmatrix} \quad 4.2$$

Subsequently applying a rotation $R_x(\Delta\theta_x)$ to the MR volume, with $\Delta\theta_x$ determined according to Equation 4.3, will set the feature lines from the two modalities parallel to each other. The matrix form of this rotation is given in Equation 4.4.

$$\Delta\theta_x = \tan^{-1}(m_y^{CT}) - \tan^{-1}(m_y^{MR}) \quad 4.3$$

$$R_x(\Delta\theta_x) = \begin{pmatrix} \mathbf{1} & \mathbf{0} & \mathbf{0} \\ \mathbf{0} & \cos \Delta\theta_x & -\sin \Delta\theta_x \\ \mathbf{0} & \sin \Delta\theta_x & \cos \Delta\theta_x \end{pmatrix} \quad 4.4$$

Finally, applying a rotation $R_y(\theta_y^{CT})$ to both image volumes will maintain the feature lines parallel to each other while restoring the CT volume to its original orientation. Therefore, the complete transformation (rotations only) that must be applied to points \vec{P}^{MR} in the match volume to make a pair of corresponding feature lines in the base and match volumes parallel to each other is an ordered product of elementary rotations, as follows:

$$(\tilde{P}^{MR})_{rot} = R_y(\theta_y^{CT}) \times R_x(\Delta\theta_x) \times R_y(-\theta_y^{MR}) \times \tilde{P}^{MR} \quad 4.5$$

By applying this transformation to the match volume prior to NMI registration, we can eliminate X and Y rotations from the NMI transformation matrix, and so limit the second stage of our hybrid registration process to 4 degrees of freedom (3 translations and Z rotation only).

4.2.5 Registration of Simulated Datasets

The simulated image data were designed to serve as test input to the Analyze 5.0 NMI algorithm, and were created as DICOM-compatible files. We first attempted automatic registration of simulated CT and MR datasets using a rigid-body transformation and allowing 6 degrees of freedom. Fully automatic registration is considered to be the process where no image pre-processing is done and no constraints are imposed on translational and rotational search parameter ranges. In Analyze 5.0, the X,Y, and Z search ranges vary from 0 – 1 by default, which corresponds to a percentage (from 0% – 100%) of the size of the X, Y and Z dimensions of the match volume. Rotational search parameters range from 0° - 180° by default. Allowing a full search range for all parameters (default settings), we attempted to register simulated CT with simulated T2-weighted and B-FFE MR image datasets. In addition, we attempted registration of these datasets after placing restrictions on some of the transformation search parameters. The ranges of restricted X and Y translations were limited to 40% and 30% of the image field of view, respectively. These limits were chosen based on the relative size of the simulated prostate in the image. The Z translation search range was not restricted as the prostate volume extends through all the slices, and such a restriction would not allow the algorithm to search through all meaningful

information. The X, Y and Z rotation ranges were limited to 0° - 10° , as we would not expect to see greater rotation in the clinical setting. Registration was also attempted allowing 4 degrees of freedom (X and Y rotations were not allowed) with the same restrictions imposed on the remaining search parameters. Datasets with and without Poisson noise added were processed to assess the algorithm's performance under such conditions.

The test procedure was performed as follows:

- The MR (match) image dataset was first translated by a known amount, between 0.87 mm (3 voxels) and 3.48 mm (12 voxels), in either the positive or negative X, or positive or negative Y, direction;
- The translated image dataset was registered to an original CT (base) image dataset;
- The differences between applied translation values and those obtained from the registration transformation matrix reported by Analyze were noted.

4.2.6 Feature Lines Method Applied to Simulated Datasets

The feasibility of the feature lines method was tested using simulated CT and T2-weighted MR datasets. We utilized a MATLAB program to apply a single rotation to a dataset about either the X or Y axis. The rotations applied were 2° , 5° , and 10° . We then used two different algorithms to determine the centroid coordinates of seeds (CT) or seed voids (MR) belonging to a single seed train that was visible in each slice. The first algorithm consisted of the following steps:

- The rotated dataset was read into a MATLAB program;

- The user visually picked the center of a corresponding seed/seed void in each slice using a cursor. The MATLAB program used this point as the center of a ROI constructed for further processing;
- The extent of the ROI in both the $\pm X$ and $\pm Y$ directions was chosen based on the size of the seed intensity profile;
- The program then fitted a 1D Gaussian function to the intensity profile across the full width of the ROI in both the X and Y directions;
- The location of the seed/seed void center in each slice was then obtained as the coordinates of the extremum of the fitted Gaussian.

For the second method we adapted a MATLAB program for edge detection written by a colleague, Hans S Jans. In this method the user first outlines an ROI surrounding the seed. The edge detection algorithm searches through this ROI to find the edges of the seed. The coordinates of the centroid of seed intensity are then determined from a weighted average of intensities within the region outlined by edge detection. The X and Y coordinates obtained from each image processing algorithm described above were plotted against their corresponding Z locations, and the lines of best fit were found. Subsequently, Equation 4.1 was used to calculate θ_x and θ_y for both simulated CT and MR image volumes. As well, differences ($\Delta\theta_x$ and $\Delta\theta_y$) between applied and calculated angles were determined. The performance of the two intensity peak finding algorithms was assessed based on these findings.

4.2.7 Registration of Clinical Datasets Using a Novel Hybrid Algorithm

After successful application of the feature lines method to the simulated datasets, we proceeded to apply this method to clinical CT and B-FE MR image volumes. In order to determine the relative X and Y rotations between the clinical CT and MR datasets, we first chose three pairs of corresponding feature lines (seed trains and corresponding needle tracks) in these volumes.

We then determined the centroid locations in each axial slice of seeds and associated needle tracks for each pair of feature lines. Centroid coordinates were determined using two different methods: visual inspection and automatic intensity peak finding. For the first method, clinical image volumes were imported into Analyze 5.0 and the user visually picked the center of a seed/seed void in each slice using a cursor. X and Y coordinates for each point were recorded. For the second method we utilized the MATLAB algorithm based on a 1D Gaussian fit to the intensity profile described in Section 4.2.6. The X and Y coordinates were plotted against their corresponding Z positions (taken to be at the centers of the slices), and the same graphical analysis as described in Section 4.2.6 was used to determine X and Y axis rotations. The procedure was repeated three times for each pair of feature lines to assess reproducibility, and the resulting rotation angles were averaged.

Using another MATLAB program, elementary rotations were applied to the clinical MR datasets for three patients according to Equation 4.5. Transformed match volumes were then imported into Analyze 5.0 where they were registered to corresponding base (CT) image volumes. Registration was limited to 4 degrees of freedom (X, Y and Z translations and Z rotation only), and was performed within a VOI that included minimal pubic bone anteriorly, extended to mid rectum posteriorly, and included no pelvic bones laterally. X and Y translation search ranges were limited to $\leq 20\%$ of the image size, and the Z rotation search range was limited to $\leq 10^\circ$. The Z translation search range spanned the full extent of the image volume. These limits were found by experience to allow the most efficient and accurate registration of clinical CT-MR volumes.

4.2.8 Registration Accuracy

To determine the accuracy of registration of the clinical datasets, we utilized measuring tools provided in Analyze 5.0 and calculated an RMS distance between corresponding points in base (CT) and transformed match (MR) image volumes according to:

$$RMS = \sqrt{\frac{\sum_{i=1}^n (c_i^{MR} - c_i^{CT})^2}{n}} \quad 4.6$$

where, c_i^{MR} and c_i^{CT} are the corresponding X, Y or Z coordinates of the i^{th} matching point in the transformed MR and original CT image volumes, respectively, and n is the number of point pairs picked.

The procedure for calculating RMS went as follows:

- The X, Y and Z coordinates of six to eight matching seed/seed voids in the original CT and B-FFE clinical volumes were selected using a cursor;
- The overall transformation matrix obtained after feature line parallelization and 4 DOF rigid-body registration of the CT and B-FFE MR datasets was applied directly to the original B-FFE volume;
- Using the original MR volume for guidance, the locations of the same points were selected on the transformed MR set also with the help of a cursor;
- The distance between the coordinates of matching points selected in the original CT and transformed MR volumes was determined in pixel units and converted into physical units;

- THE RMS distances for X, Y and Z coordinates were calculated according to Equation 4.6;
- A standard error propagation formalism was used to estimate the error associated with each calculated RMS value, according to Equation 4.7 below:

$$\Delta RMS = \frac{1}{\sqrt{n}} * \sqrt{(\delta c_i^{MR})^2 + (\delta c_i^{CT})^2} \quad 4.7$$

where δc_i^{MR} and δc_i^{CT} are the estimated errors in picking the X, Y and Z coordinates of matching points in the MR and CT image volumes, respectively.

Choosing the same matching points and following the same procedure we also calculated RMS distance values for clinical image volumes registered independently by a collaborator (Radiation Oncology resident) with the Procrustes algorithm implemented in VariSeed 7.1.

4.3 Results

4.3.1 Simulated Datasets

Simulated CT and MR prostate implant datasets were used to investigate the ability of the NMI algorithm implemented in Analyze 5.0 to reliably perform automatic (no image preprocessing) and semi-automatic (some image preprocessing) rigid-body registration when 6 DOF are allowed. Possibly due to a large difference between background intensities in the CT and B-FFE MR datasets (see Table 4.1), the algorithm initially failed to attempt the registration of these two volumes. To be able to proceed with the registration process, we inverted the intensities of structures in the B-FFE MR

datasets. Inverted intensities had values of 40, 315 and 0 for prostate, seeds and the background, respectively. Following the test procedure described in Section 4.2.5 we performed 6 DOF registration of CT and T2-weighted MR, and CT and B-FFE MR, simulated datasets. The results are reported in Table 4.2. The algorithm did not perform particularly well whether restrictions on search parameters in MR datasets were imposed or not. In all cases we found that although the average differences between applied and reported X and Y translations were lower than a clinically acceptable tolerance of 1 mm, the maximum differences exceeded this tolerance and were as high as ~8 mm. In addition, small rotations ($\sim 1.5^\circ$) about the Z axis, as well as Z translations of ~7 mm, were observed in some transformation matrices.

We proceeded to test NMI algorithm performance when X and Y rotational degrees of freedom are eliminated from the registration process (as they would be when determined by the feature line method). We used the same procedure and applied the same restrictions on search parameters as for 6 DOF registration. We also repeated the registrations after adding Poisson noise to our datasets. Table 4.3 summarizes the results of this exercise. We found that maximum differences between applied and reported translations now fell within a clinically acceptable tolerance of 1 mm for both noiseless and noisy images. Transformation matrices for images without noise did not contain any Z translations, however those for images with Poisson noise did contain small Z translations (≤ 0.4 mm). No rotations about the Z-axis were observed in either case.

4.3.2 Assessment of Feature Lines Method with Simulated Datasets

Considering the similar results we obtained from registration of simulated T2-weighted MR to CT and B-FFE MR to CT data, we assessed the

feature lines method only for simulated CT and T2-weighted MR. Following the procedure described in Section 4.2.6, we calculated the angles of rotation for each dataset and determined the differences between applied and calculated values. As shown in Table 4.4, both methods for finding the centroids of seed intensities gave acceptably accurate results, with the greatest difference between applied and measured angles being 0.28° , which is well below the clinically acceptable tolerance of 1.0° . However, the intensity peak finding algorithm based on a Gaussian fit yielded slightly more accurate results than the edge detection algorithm in all cases. Figure 4.4 shows a few examples of linear fits to simulated CT and MR dataset feature coordinates.

4.3.3 Registration of Clinical Datasets

Using graphical analysis of feature centroid data we determined rotation angles θ_x , θ_y and $\Delta\theta_x$ for three pairs of corresponding feature lines in CT and B-FFE MR image volumes for each of three patients. Plots shown in Figures 4.5 and 4.6 are examples of linear fits to CT and MR feature coordinates obtained using the automated intensity peak finding algorithm for a single pair of feature lines for patients A and B, respectively. Average angle values, as determined from the results of three separate centroid selection trials for each feature line pair for patients A, B and C, are reported in Table 4.5.

With sequential application of $-\theta_y^{MR}$, $\Delta\theta_x$ and θ_y^{CT} rotations to the MR image volume we parallelized MR feature lines with corresponding CT feature lines, and then followed with 4 DOF registration utilizing the NMI algorithm. This hybrid approach successfully registered clinical image volume pairs, as judged by visual inspection, provided that some anterior bony structures and anterior rectum were included in the VOI. The presence of motion artifacts in

the MR volume for patient B (see Figure 4.7) required a VOI that extended beyond mid-rectum posteriorly.

4.3.4 Error Analysis

The overall accuracy of registration of clinical CT and B-FFE MR volumes was estimated by visual inspection to be ≤ 1.5 mm for all three patients. We also determined registration quality in terms of RMS distances between X, Y and Z coordinates of several matching points in each pair of clinical volumes. We picked 7, 6 and 8 matching point pairs from the base (CT) and transformed (MR) volumes for patients A, B and C, respectively. The errors associated with manual picking of point coordinates were estimated to be 2 pixels (0.59 mm) in the X and Y directions and half a slice thickness (1.50 mm) in the Z direction, and the total error in the RMS distance was calculated according to Equation 4.7. Table 4.6 summarizes the results of the RMS distance calculations for patients A, B and C. RMS distances calculated for each dimension were added in quadrature to determine a total 3D RMS distance for each patient. Table 4.7 compares 3D RMS values calculated for volumes independently registered by the hybrid and Procrustes algorithms.

4.4 Discussion

Post-implant dosimetry plays an important role in the assessment of prostate implant quality and treatment outcome. No single imaging modality provides optimal visualization of both seeds and soft tissue structures, necessary for accurate calculation of dosimetric indices. However, registration of post-implant CT and MR image volumes combines the necessary information in a fused image set, and therefore, it is a promising approach for improving post-implant dose estimation accuracy. T2-weighted MR has been

the most commonly used MR imaging sequence in post-implant dosimetry [McLaughlin *et al.*, 2004, Roberson *et al.*, 2005, etc.]. Here we introduce B-FFE MR as an alternative that appears to provide better visualization of structures of interest.

4.4.1 Simulated Datasets

Our work indicates that the NMI algorithm implemented in Analyze 5.0 is not capable of reliable automatic and semi-automatic rigid-body registration of simulated CT and either T2-weighted or B-FFE MR prostate only datasets when 6 DOF are allowed. Placing reasonable restrictions on search parameters (see Section 4.2.5) did not seem to improve the algorithm's performance. We hypothesized that the algorithm's inability to successfully register simulated datasets when 6 DOF are allowed is due in large part to poorer image resolution in the Z direction, which renders the algorithm insensitive to small rotations in the Y-Z and X-Z image planes, and thereby prevents accurate determination of X and Y axis rotation angles. This ultimately leads to poor registration results. Due to the poor performance of Analyze 5.0 for 6 DOF registration of noiseless simulated datasets, we did not attempt 6 DOF registration of simulated images containing Poisson noise, as we would not expect improvement in the algorithm's performance under these circumstances.

The results of 4 DOF registration (X and Y rotation excluded) of simulated CT and MR prostate only datasets supported our hypothesis and indicated that reducing the degrees of freedom for rigid-body rotation from 3 to 1 (rotation about the Z-axis remaining) may allow a more accurate registration with an intensity-based algorithm because of the higher information density in the X-Y imaging plane. These results also suggested that the presence of Poisson noise in the images does not interfere with the ability of the NMI

algorithm to successfully perform 4 DOF registration within a clinically acceptable tolerance of 1 mm.

We assessed the feasibility of the feature lines method using simulated CT and T2-weighted MR datasets. Based on the results of this test, we felt that the feature lines method could potentially be used with clinical images to determine angles of rotation about the X and Y axes prior to NMI registration.

4.4.2 Clinical Volumes

Encouraged by the results from tests done on the simulated datasets, we proceeded to investigate the capability of the hybrid algorithm to perform semi-automatic 3D rigid-body registration of post-implant CT and MR prostate image volumes. The method consists of two steps. First, the feature lines method is utilized to achieve parallelization of corresponding features running primarily in the Z direction in the CT and MR image volumes. Parallelization of corresponding feature lines involves determining their relative rotations in the X-Z and Y-Z planes, and subsequently applying these rotations to the MR (match) image volume. With this step completed, we effectively eliminate two degrees of freedom from the NMI registration step that follows. The second step involves applying the NMI algorithm from Analyze 5.0 to register CT and MR volumes. Although T2-weighted MR volumes were also available, the B-FFE MR images were our preferred choice for completion of the first step of the hybrid registration algorithm, because they provided better visualization of needle tracks. In addition, the contrast between structures of interest was better in the B-FFE images, as intensity levels were higher relative to those in the T2-weighted images. This is reflected in the information content in the B-FFE images being higher (for patient A: $H(\text{B-FFE}) = 2.25$ and $H(\text{T2}) = 0.02$, on average, as calculated for the registration ROI in 2D slices), likely making

them more suitable for registration utilizing a voxel intensity-based algorithm such as NMI.

The three pairs of corresponding seed trains (CT) and needle tracks (MR) for each patient used in the analysis were chosen after careful consideration of several factors:

- the number of seeds delivered by each needle;
- the degree of correspondence between seeds (CT) and seed voids (MR) in axial slices;
- the ability to distinguish between seeds/seed voids originating from different needles;
- the relative placement of seeds within the prostate; and
- the presence of soft tissue edema and prostate deformation following implantation.

Although both methods used for finding seed/seed void centroids gave consistent centroid locations for CT volumes, the intensity peak finding algorithm did not work well for the MR image volumes. We believe the reason is that the needle tracks in the MR images have a broad, and not a well-defined profile, resulting in a fairly wide Gaussian fit. This makes it hard for the algorithm, which is sensitive to image data fluctuations, to determine the true centroid location accurately. Considering that in the case of CT volumes, the manual method provided centroid locations that were consistent with those determined by the Gaussian fitting algorithm, we were quite confident that it could be used for finding feature centroids in the MR volumes as well. Therefore, we performed our analysis of clinical CT and MR volumes using manually determined centroid data.

As shown in Figures 4.5 and 4.6, data points of features obtained from clinical volumes do not always closely follow a straight line. This is to be expected because of tissue flexibility and deformation subsequent to needle

insertion into the prostate, which leads to relative motion between the seeds belonging to a single needle. However, the data points are distributed along an average direction (feature line), which can be used to determine relative angles of rotation through graphical analysis.

The clinical results reported in Table 4.5 indicate that the relative prostate rotation about the Y axis between CT and MR scans was negligible. θ_y values for corresponding feature lines in CT and MR volumes for all three patients were within 0.5° of each other. Prostate rotation about the X axis between scans was on average $\sim 1.5^\circ$ in each case. In addition, the average $\Delta\theta_x$ value was consistent for all pairs of corresponding feature lines for patients A and B, having a standard deviation of 0.17° and 0.21° , respectively. $\Delta\theta_x$ values for corresponding needle pairs for patient C were more variable and had a standard deviation of 1.43° . This behaviour may stem from tissue deformation in a part of prostate, possibly caused by rectal or bladder filling. The trends observed here agree with the findings of van Herk and colleagues [van Herk *et al.*, 1995] who reported, based on analysis of EPID images of prostate markers, that the rotation of the prostate is largest around the left-right (X) axis, while rotations in other directions are much smaller.

We observed that the quality and efficiency of 4 DOF NMI-based registration of parallelized clinical CT and B-FFE MR prostate implant image volumes depends on the extent of the registration VOI and the limits imposed on search parameter ranges. Restricting the transformation parameter search to a small range improves the algorithm's efficiency and helps prevent it from finding local maxima of the cost function. The hybrid algorithm was not able to register volumes with a VOI limited to prostate only. Similarly to what was reported by McLaughlin *et al.* in 2004, we found that the VOI needs to include some anterior bony structures, as well as anterior rectum. The presence of motion artifacts in the MR images seems to hinder the NMI algorithm's ability

to achieve a good registration, and for one patient necessitated a VOI that extended beyond mid-rectum posteriorly. Motion artifacts caused by patient movement due to breathing or discomfort during scanning appear as blur on axial image slices and reduce image quality, which in turn affects the algorithm's performance. Figure 4.7 illustrates the effects of motion artifact on image quality. It should also be noted that the results obtained here with the NMI algorithm in the Analyze 5.0 software package may differ from those for other NMI registration algorithms. In particular, the Analyze implementation makes use of image data sampling to build the joint entropy histogram [Camp and Robb, 1999], and therefore might not fully utilize all of the information available in the registration VOI.

Matching points used for error analysis were chosen carefully with the aid of some image preprocessing such as magnification and window and level manipulation. By picking seeds that were centered in the middle of CT slices (in the Z direction), we ensured better visibility (definition and size) of matching seed voids in the corresponding MR slices. Picking error was estimated based on our experience with the manual method of picking feature centroids. We determined the average distances between matching point pairs along the X, Y and Z directions as well as the errors associated with these calculations. Results in Table 4.6 suggest that the algorithm performs registration with acceptable accuracy. We believe that lower registration quality in the case of patient B compared to the other two patients may be due to the presence of motion artifacts in the MR volume for this patient. Results of Procrustes-based registration also suggest that patient B data was the most problematic.

4.5 Conclusion

A novel hybrid algorithm described in this chapter shows promise in providing efficient and accurate 6 DOF rigid-body registration of CT and B-FFE

MR post-implant prostate image volumes. In comparison to Procrustes-based registration, 3D RMS distance measures indicate that the new algorithm achieves slightly more accurate registration (see Table 4.7). While the Procrustes method requires approximately 20 minutes of dedicated user's time, the hybrid algorithm could be streamlined by automation of the parallelization process (see Section 5.2) to provide semi-automatic registration in much less time. For the hybrid algorithm to achieve registration with acceptable transformation error, the registration VOI must include anterior rectum and some pubic bone. As well, care should be taken to minimize unnecessary movement during imaging to avoid motion artifacts which can decrease the accuracy of registration.

Structure	Intensity		
	CT	MR	
		T2-weighted	B-FFE
prostate	50	160	360
seed	2050	130	85
background	0	40	400

Table 4.1 Simulated implant image data – structure intensities.

Difference	No Restrictions			With Restrictions		
	ΔX [mm]	ΔY [mm]	ΔZ [mm]	ΔX [mm]	ΔY [mm]	ΔZ [mm]
	CT-MR T2					
Average	0.56	0.83	0.98	0.50	0.68	0.85
Maximum	7.18	7.78	7.92	6.86	6.02	7.14
Minimum	0.00	0.02	0.00	0.00	0.02	0.00
	CT-MR BFFE inverted					
	ΔX [mm]	ΔY [mm]	ΔZ [mm]	ΔX [mm]	ΔY [mm]	ΔZ [mm]
	CT-MR BFFE inverted					
Average	0.44	0.62	0.43	0.34	0.59	0.32
Maximum	3.64	4.31	3.39	2.05	3.41	2.40
Minimum	0.04	0.01	0.00	0.03	0.01	0.00

Table 4.2 Results of 6 DOF registration of simulated datasets with and without restrictions on search parameters. Restrictions placed on X and Y translation ranges and X, Y, and Z rotation ranges are described in Section 4.2.5.

Difference	No Noise			Poisson Noise		
	ΔX [mm]	ΔY [mm]	ΔZ [mm]	ΔX [mm]	ΔY [mm]	ΔZ [mm]
	CT-MR T2					
Average	0.13	0.20	0.00	0.19	0.24	0.23
Maximum	0.44	0.43	0.00	0.64	0.84	0.84
Minimum	0.00	0.01	0.00	0.00	0.00	0.10
	CT-MR BFFE inverted					
	ΔX [mm]	ΔY [mm]	ΔZ [mm]	ΔX [mm]	ΔY [mm]	ΔZ [mm]
	CT-MR BFFE inverted					
Average	0.20	0.27	0.00	0.22	0.31	0.14
Maximum	0.50	0.88	0.00	0.60	0.91	0.31
Minimum	0.00	0.00	0.00	0.02	0.00	0.00

Table 4.3 Results of 4 DOF registration of simulated datasets with and without Poisson noise. X and Y rotations were not allowed and restrictions were placed on X and Y translation and Z rotation search ranges as described in Section 4.2.5.

MR T2						
Method	X rotation [°]		Y rotation [°]		Difference [°]	
	applied	calculated	applied	calculated	$\Delta\theta_x$	$\Delta\theta_y$
Gaussian	2	1.98	2	2.03	0.02	0.03
Edge	2	2.23	2	2.06	0.23	0.06
Gaussian	5	5.01	5	4.97	0.01	0.03
Edge	5	5.25	5	4.72	0.25	0.28
Gaussian	10	9.98	10	9.92	0.02	0.08
Edge	10	9.95	10	9.72	0.05	0.28

a

CT						
Method	X rotation [°]		Y rotation [°]		Difference [°]	
	applied	calculated	applied	calculated	$\Delta\theta_x$	$\Delta\theta_y$
Gaussian	2	2.00	2	2.01	0.00	0.00
Edge	2	1.96	2	1.99	0.04	0.01
Gaussian	5	4.91	5	4.91	0.09	0.09
Edge	5	4.77	5	7.79	0.23	0.21
Gaussian	10	9.82	10	10.05	0.18	0.05
Edge	10	9.80	10	9.93	0.20	0.07

b

Table 4.4 Comparison of applied rotations with those calculated by the feature lines method for simulated datasets: a) T2-weighted MR dataset; b) CT dataset.

	$\theta_{y,ave}$ [°]		$\theta_{x,ave}$ [°]		$\Delta\theta_x$ [°]
Patient A	CT	MR	CT	MR	CT-MR
Line #1	-6.30±0.03	-6.59±0.24	3.05±0.14	4.63±0.27	-1.58
Line #2	2.27±0.27	2.01±0.07	8.47±0.16	10.13±0.15	-1.66
Line #3	2.16±0.30	1.98±0.10	1.97±0.15	3.31±0.14	-1.34
$\Delta\theta_{x,ave}$					-1.53
σ					0.17

a

	$\theta_{y,ave}$ [°]		$\theta_{x,ave}$ [°]		$\Delta\theta_x$ [°]
Patient B	CT	MR	CT	MR	CT-MR
Line #1	-4.39±0.00	-4.91±0.12	4.91±0.16	6.57±0.20	-1.65
Line #2	-6.13±0.56	-5.76±0.85	-6.69±0.0	-5.39±0.32	-1.30
Line #3	-5.00±0.33	-5.42±0.28	-7.82±0.62	-6.53±0.09	-1.27
$\Delta\theta_{x,ave}$					-1.41
σ					0.21

b

	$\theta_{y,ave}$ [°]		$\theta_{x,ave}$ [°]		$\Delta\theta_x$ [°]
Patient C	CT	MR	CT	MR	CT-MR
Line #1	4.17±0.31	4.38±0.63	20.81±0.40	20.64±0.37	-0.17
Line #2	-1.96±0.13	-2.45±0.33	13.92±0.26	16.92±0.44	-3.00
Line #3	-6.44±0.00	-6.81±0.32	0.92±0.14	2.13±0.18	-1.21
$\Delta\theta_{x,ave}$					-1.46
σ					1.43

c

Table 4.5 Relative rotation angles for three feature line pairs in the clinical image volumes for: a) patient A; b) patient B; and c) patient C.

Patient A	$(MR_{coord} - CT_{coord})$			$(MR_{coord} - CT_{coord})^2$		
matching point pairs	X [mm]	Y [mm]	Z [mm]	X [mm ²]	Y [mm ²]	Z [mm ²]
1	0.0	0.6	0.0	0.0	0.3	0.0
2	0.0	0.0	1.5	0.0	0.0	2.3
3	0.3	0.6	0.0	0.1	0.3	0.0
4	0.9	0.9	0.0	0.8	0.8	0.0
5	0.3	0.6	1.5	0.1	0.3	2.3
6	0.3	0.3	1.5	0.1	0.1	2.3
7	0.0	0.3	0.0	0.0	0.1	0.0
sum	1.8	3.2	4.5	1.0	2.0	6.8
RMS [mm]				0.4	0.5	1.0
Δ RMS [mm]				0.3	0.3	0.8

a

Patient B	$(MR_{coord} - CT_{coord})$			$(MR_{coord} - CT_{coord})^2$		
matching point pairs	X [mm]	Y [mm]	Z [mm]	X [mm ²]	Y [mm ²]	Z [mm ²]
1	1.2	1.5	1.5	1.4	2.1	2.3
2	1.5	1.5	1.5	2.1	2.1	2.3
3	0.3	0.9	1.5	0.1	0.8	2.3
4	1.5	1.2	0.0	2.1	1.4	0.0
5	1.2	1.8	1.5	1.4	3.1	2.3
6	1.2	1.8	0.0	1.4	3.1	0.0
sum	6.7	8.5	6.0	8.5	12.6	9.0
RMS [mm]				1.2	1.5	1.2
Δ RMS [mm]				0.3	0.3	0.9

b

Patient C	$(MR_{coord} - CT_{coord})$			$(MR_{coord} - CT_{coord})^2$		
matching point pairs	X [mm]	Y [mm]	Z [mm]	X [mm ²]	Y [mm ²]	Z [mm ²]
1	1.2	0.9	1.5	1.4	0.8	2.3
2	0.9	1.2	0.0	0.8	1.4	0.0
3	0.6	0.6	1.5	0.3	0.3	2.3
4	0.6	0.9	0.0	0.3	0.8	0.0
5	0.3	0.6	1.5	0.1	0.3	2.3
6	0.6	0.6	1.5	0.3	0.3	2.3
7	0.3	0.0	1.5	0.1	0.0	2.3
8	0.0	0.3	0.0	0.0	0.1	0.0
sum	4.4	5.0	7.5	3.3	4.0	11.3
RMS [mm]				0.6	0.7	1.2
Δ RMS [mm]				0.3	0.3	0.8

c

Table 4.6 RMS distances between X, Y and Z coordinates of corresponding points (seeds/seed voids) in registered clinical CT and MR volumes: a) for patient A; b) for patient B; and c) for patient C.

	RMS _{hybrid} [mm]	RMS _{Proc} [mm]
Patient A	1.2 ± 0.7	1.6 ± 0.6
Patient B	2.2 ± 0.6	2.3 ± 0.6
Patient C	1.5 ± 0.6	1.7 ± 0.5

Table 4.7 Comparison of 3D RMS distances for clinical volumes registered by the hybrid and Procrustes algorithms.

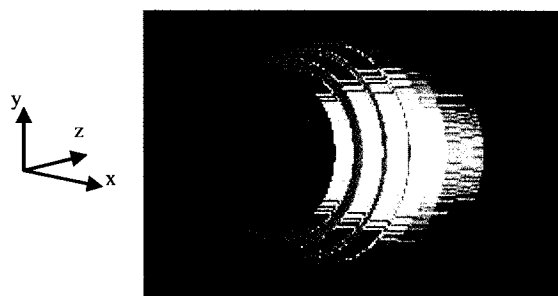


Figure 4.1 Volume rendering of a simulated CT prostate implant dataset.

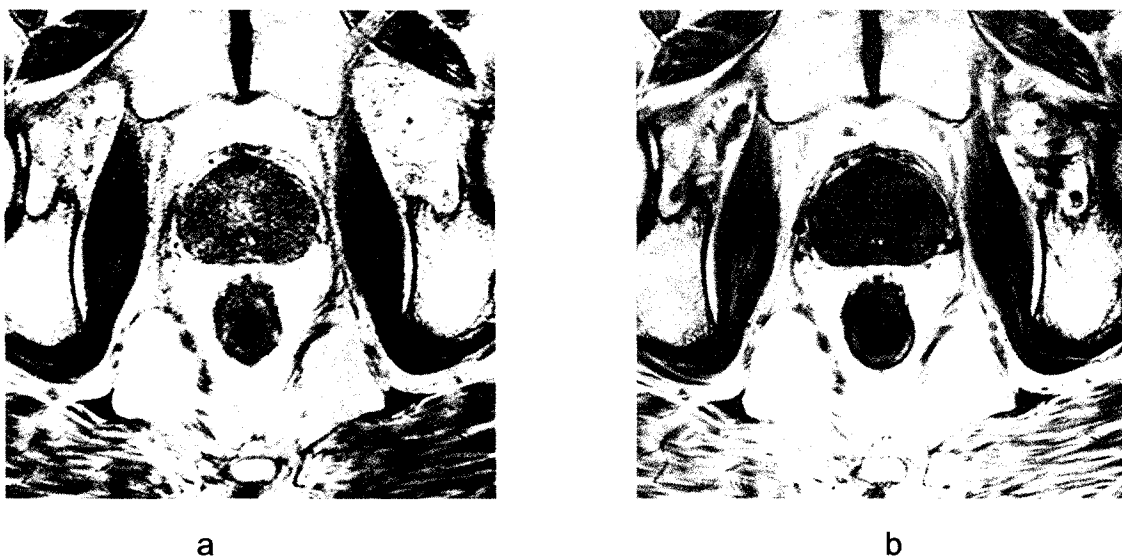


Figure 4.2 a) Axial slice of T2-weighted MR volume set of post-implant prostate; b) corresponding axial slice of B-FFE MR volume set.

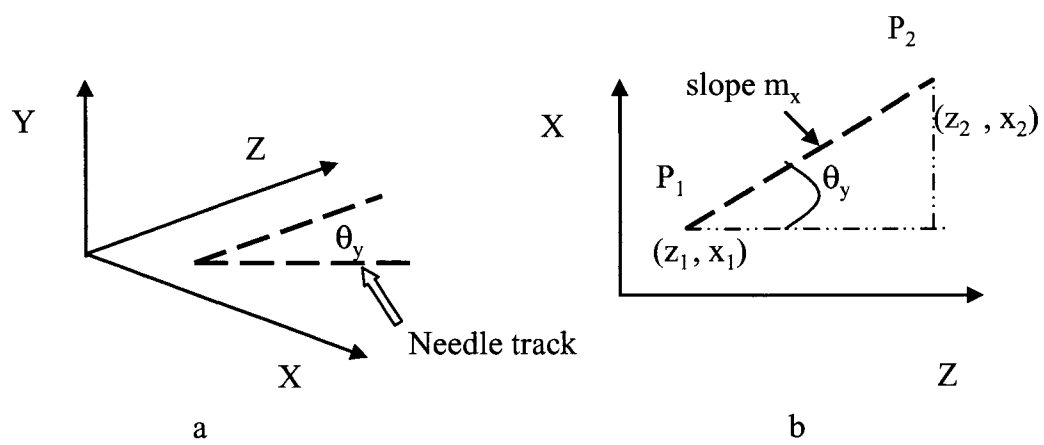


Figure 4.3 Orientation of a feature line in 3D space: a) rotation of a needle track about the Y – axis, b) θ_y , angle of rotation in the X – Z plane.

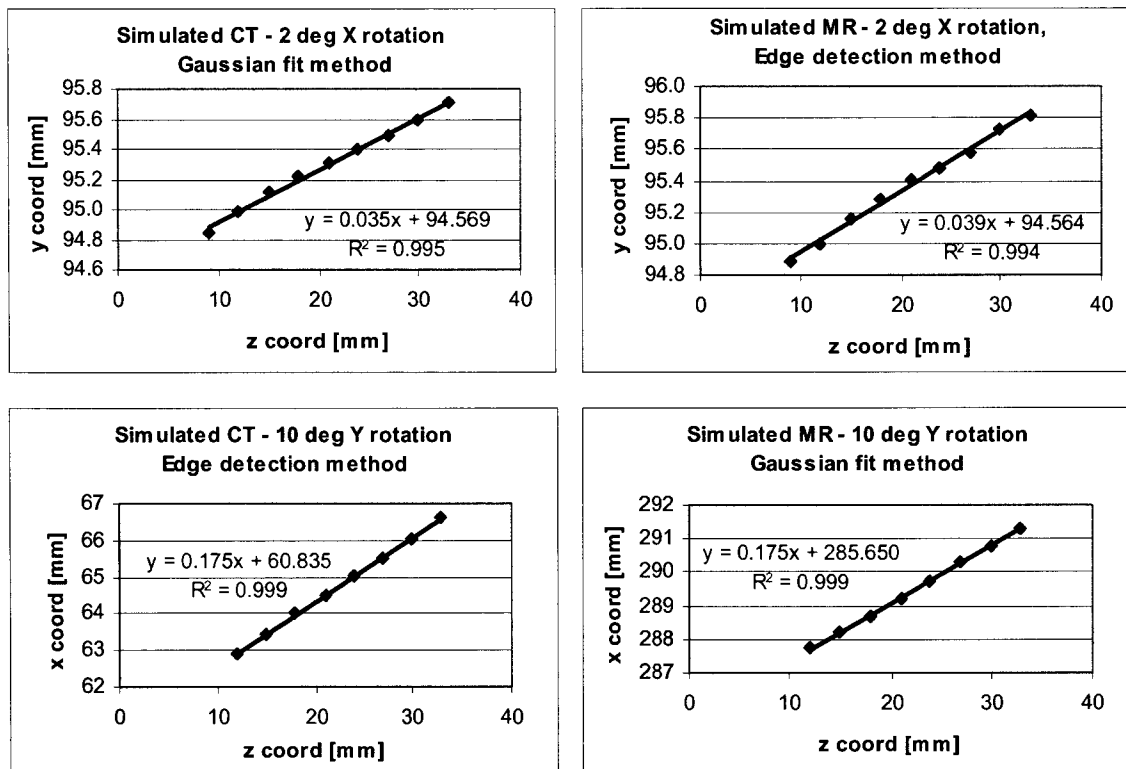


Figure 4.4 Examples of linear fits to simulated CT and MR image volume feature coordinates.

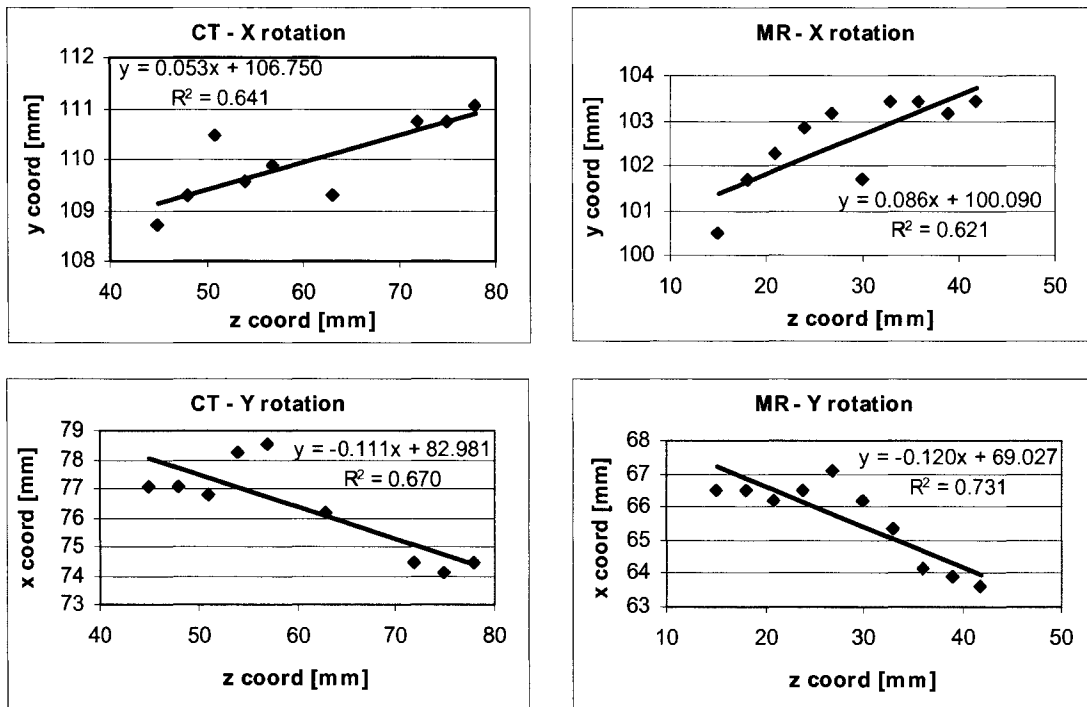


Figure 4.5 Sample plots used in graphical analysis for determination of θ_x and θ_y for a pair of feature lines in the set of clinical image volumes for patient A.

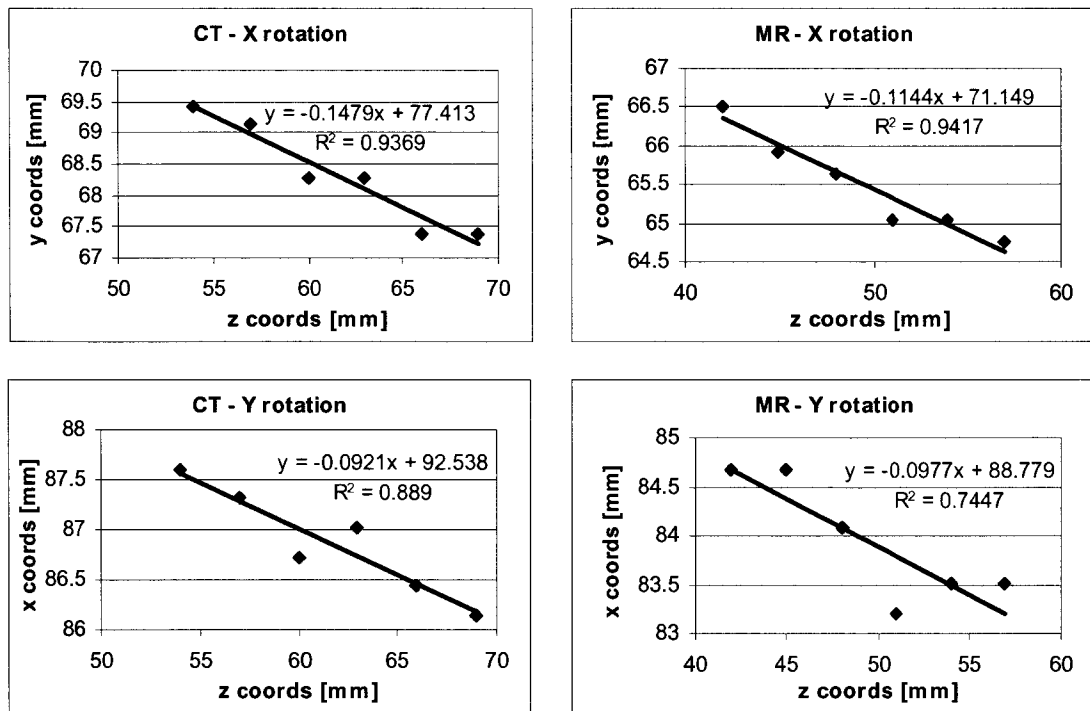


Figure 4.6 Sample plots used in graphical analysis for determination of θ_x and θ_y for a pair of feature lines in the set of clinical image volumes for patient B.

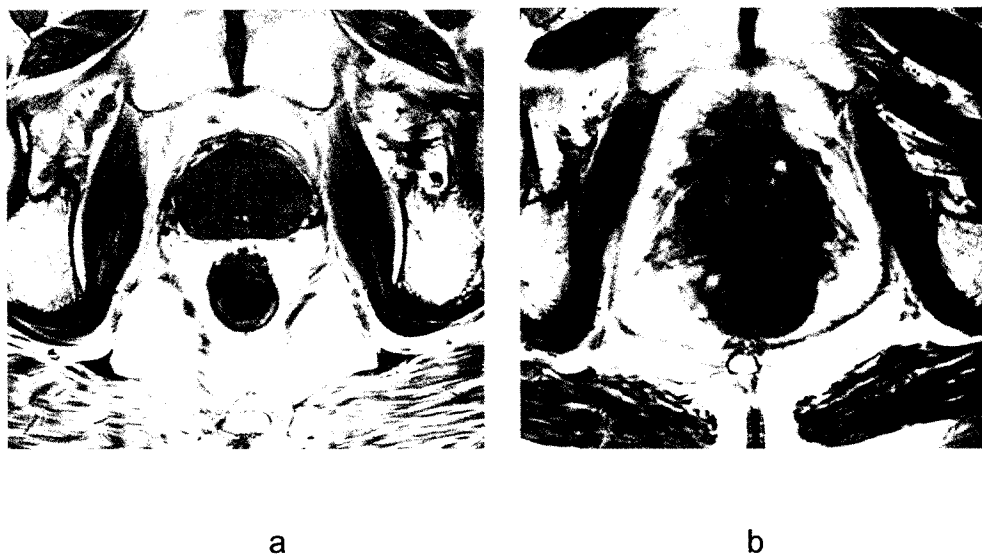


Figure 4.7 Clinical B-FFE axial MR slices of the prostate near mid-gland illustrating the dependence of image quality on the presence of motion artifact: a) no noticeable motion artifact present – image features appear sharp; b) considerable amount of motion artifact present – image features appear blurred.

4.6 References

1. Amdur R. J., Gladstone D., Leopold K. A., Harris R. D., Prostate seed implant quality assessment using MR and CT image fusion, *International Journal of Radiation Oncology, Biology, Physics*, 43(1), 67-72 (1999)
2. Bushberg J. T., Seibert J. A., Leidholdt E. M. Jr., Boone J. M., "The Essential Physics of Medical Imaging", 2nd ed., Lippincott Williams & Wilkins, Philadelphia, (2002)
3. Camp J., Robb R. A., A novel binning method for improved accuracy and speed of volume image co-registration using normalized mutual information, *Proceedings SPIE – The International Society for Optical Engineering*, 3661, 24-31 (1999)
4. Dubois D. F., Prestidge B. R., Hotchkiss L. A., Prete J. J., Bice W. S., Intraobserver and interobserver variability of MR-imaging and CT-derived prostate volumes after transperineal interstitial permanent prostate brachytherapy, *Radiology*, 207, 785-789 (1998)
5. Kagawa K., Lee R. W., Schultheiss T. E., Hunt M. A., Shaer A. H., Hanks G. E., Initial clinical assessment of CT-MRI image fusion software in localization of the prostate for 3D conformal radiation therapy, *International Journal of Radiation Oncology, Biology, Physics*, 38(2), 319-325 (1997)
6. McLaughlin P. W., Narayana V., Kessler M., McShan D., Troyer S., Marsh L., Hixson G., Roberson P. L., The use of mutual information in registration of CT and MRI datasets post permanent implant, *Brachytherapy*, 3(2), 61-70 (2004)

7. Parker C. C., Damyanovich A., Haycocks T., Haider M., Bayley A., Catton C. N., Magnetic resonance imaging in the radiation treatment planning of localized prostate cancer using intra-prostatic fiducial markers for computed tomography co-registration, *Radiotherapy and Oncology*, 66(2), 217-224 (2003)
8. Roberson P. L., McLaughlin P. W., Troyer S., Hixson G. V., Kessler M. L., Use and uncertainties of mutual information for computed tomography / magnetic resonance (CT/MR) registration post permanent implant of the prostate, *Medical Physics*, 32(2), 473-482 (2005)
9. Servois V., Chauveinc L., El Khoury C., Lantoine A., Ollivier L., Flam T., Rosenwald J. C., Cosset J. M., Neuenschwander S., CT and MR image fusion using two different methods after prostate brachytherapy: impact on post-implant dosimetric assessment, *Cancer Radiothérapie*, 7(1), 9-16 (2003)
10. Van Herk M., Bruce A., Kroes G. A. P., Shouman T., Touw A., Lebesque J. V., Quantification of organ motion during conformal radiotherapy of the prostate by three dimensional image registration, *International Journal of Radiation Oncology, Biology, Physics*, 33(5), 1311-1320 (1995)

CHAPTER 5

5 SUMMARY AND FUTURE DIRECTIONS

5.1 Summary

An important limitation of current practice for post-dosimetric analysis of prostate implants is poor visualization of the prostate boundary on CT images. This limitation often leads to overestimation of prostate volume [Dubois *et al.*, 1998] and consequently, the values of clinically important dosimetric indices such as D_{90} and V_{100} are often determined inaccurately. This in turn may lead to an incorrect assessment of implant quality and prediction of treatment outcome.

The work presented in this thesis was done with the intent of finding an improved and clinically practicable approach to prostate visualization that would allow for more accurate post-dosimetric analysis. Accurate post-implant calculations necessitate accurately outlined prostate contours and precise localization of implanted seeds. While prostate contour visualization in CT images is problematic, seeds locations are clearly visible. On the contrary, MR images provide excellent soft tissue delineation, while it is hard to determine exact seed positions with confidence and accuracy. Combining such complimentary information can be achieved through image registration of CT and MR images of prostate implants. We investigated the suitability of a normalized mutual information registration algorithm for registration of clinical CT and MR images. To register image datasets we utilized the Analyze 5.0 (AnalyzeDirect Inc., Lenexa, KS) software package.

Initial attempts to perform unrestricted 6 DOF rigid-body registration of clinical datasets were unsuccessful. We proceeded with preliminary tests using a simple water phantom to gain insight into the NMI algorithm performance. These tests helped us understand that image preprocessing such as intensity thresholding and careful choice of VOI could aid the registration process. Using the water phantom with an insert holding inactive seed sources we also determined the amount of distortion in CT and MR image volumes in the axial plane and along the scanning axis. We found that spatial distortions in both CT and MR images across a $\sim 45 \text{ cm}^3$ volume of interest in our phantom were minimal ($< 1 \text{ mm}$ on average).

We also investigated the ability of the NMI algorithm to reliably perform 6 DOF automatic and semi-automatic rigid-body registration of simulated CT and MR prostate implant datasets. Simulated datasets (CT, T2-weighted MR and B-FFE MR) were created using MATLAB code and contained the main features of clinical interest with intensities corresponding to those in clinical image volumes. We found that the algorithm did not perform well whether restrictions on search parameters for the match (MR) volume were imposed or not. The maximum errors greatly exceeded the clinically acceptable tolerance of 1 mm, reaching almost 8 mm in some cases.

Considering that it is possible to observe the position of needle tracks in the axial slices of post-implant clinical images, we postulated that it may be feasible to use this information to determine required rotations about the X and Y axes, prior to NMI-based registration. We developed a so-called feature lines method to determine out of plane rotations based on graphical analysis of coordinates of image features that run primarily in the Z direction. Applying this method to clinical images effectively reduces the number of degrees of freedom from 6 to 4 (X, Y and Z translations and Z rotation remaining).

In light of this, we performed more tests with simulated datasets, where we eliminated X and Y axis rotations from the registration process and imposed the same restrictions on search parameters for 6 DOF. Datasets with and without Poisson noise added were processed to assess the algorithm's performance. We found that the maximum registration error (0.9 mm) fell within the clinically acceptable tolerance of 1 mm for both noiseless and noisy images. Based on these results we were reasonably confident that the feature lines approach could be used to improve the NMI algorithm performance in registering clinical volumes.

The next step was to investigate the capability of a novel hybrid algorithm to perform semi-automatic (some operator guidance required, search parameters restricted) 3D rigid-body registration of post-implant CT and MR prostate volumes. This algorithm consisted of two stages. In the first stage, the feature lines method was used to parallelize corresponding image features running primarily in the Z direction. The second stage involved applying the NMI algorithm implemented in Analyze 5.0 to complete the registration of clinical image volumes.

We applied this algorithm to corresponding CT and B-FFE MR image volumes for three different patients. We found that both the accuracy and efficiency of the registration strongly depended on the choices of VOI and limits imposed on the transformation search parameters. In addition, we found that the presence of motion artifacts in the MR volume appears to hinder the quality of registration. To achieve registration with the desired ~ 1 mm accuracy, it was necessary to include minimal pubic bone and anterior rectum in the VOI and to place appropriate limits on the search parameters. The quality of registration was assessed using RMS differences calculated for several matching points picked in the volumes registered. According to these calculations, the highest 3D RMS value of ~ 2.2 mm was calculated for patient

B, where motion artifacts were present in the MR volume. RMS values for patients A and C were well below this, being (1.2 ± 0.7) mm to (1.5 ± 0.6) mm, respectively.

In conclusion, our work indicates that a hybrid algorithm consisting of parallelization of feature lines running primarily in the Z direction, followed by NMI-based registration as implemented in Analyze 5.0 software, can perform semi-automatic 6 DOF rigid-body registration of clinical CT and MR prostate post-implant volumes. The hybrid algorithm presented in this thesis is in its infancy, but shows good potential to provide the means for improving both the efficiency and accuracy of post-implant dosimetry.

5.2 Future Directions

Regarding results and findings reported herein, there are a couple of suggestions for future work on this project.

The first task to be completed should be automation of the hybrid algorithm. This could be accomplished by creating software that would perform all the steps in the parallelization procedure sequentially without the need for user input, which would improve both the efficiency and accuracy of this procedure. Such an algorithm would have to be capable of reliably performing the following tasks:

1. Find corresponding slices in CT and MR volumes;
2. Pick corresponding features (seed trains/needle tracks) and determine their centroid coordinates on each slice;
3. Perform graphical analysis of this data to determine X and Y axis rotation angles for each feature line;
4. Apply these rotations to the match image volume;
5. Output the rotated image volume.

Once parallelization is accomplished, semi-automatic registration can be done using the NMI algorithm provided in Analyze 5.0. It should be possible to pre-select the VOI and to pre-set the limits on search parameter ranges.

Secondly, considering the much better quality of clinical MR images acquired at 3T, we suggest that a study similar to ours should be done to investigate the performance of the NMI algorithm by itself, as well as the performance of the hybrid algorithm, at this higher magnetic field strength.

It seems likely that using the hybrid algorithm where the feature line parallelization and NMI registration processes are automated, along with acquisition of better quality MR image volumes, will improve the accuracy and efficiency of registration of CT and MR post-implant prostate images. This in turn is expected to ultimately lead to improvements in post-implant dosimetry accuracy.

5.3 References

1. Dubois D. F., Prestidge B. R., Hotchkiss L. A., Prete J. J., Bice W. S., Intraobserver and interobserver variability of MR-imaging and CT-derived prostate volumes after transperineal interstitial permanent prostate brachytherapy, *Radiology*, 207, 785-789 (1998)

BIBLIOGRAPHY

Amdur R. J., Gladstone D., Leopold K. A., Harris R. D., Prostate seed implant quality assessment using MR and CT image fusion, *International Journal of Radiation Oncology, Biology, Physics*, 43(1), 67-72 (1999) p: 83

Bushberg J. T., Seibert J. A., Leidholdt E. M. Jr., Boone J. M., "The Essential Physics of Medical Imaging", 2nd ed., Lippincott Williams & Wilkins, Philadelphia, (2002) p: 49, 54, 86

Camp J., Robb R. A., A novel binning method for improved accuracy and speed of volume image co-registration using normalized mutual information, Proceedings SPIE – The International Society for Optical Engineering, 3661, 24-31 (1999) p: 34, 35, 103

Chan J. M., Jou R. M., Carrol P. R., The relative impact and future burden of prostate cancer in the United States, *The Journal of Urology*, 172, S13-S17 (2004) p: 5

Dubois D. F., Prestidge B. R., Hotchkiss L. A., Bice W. S., Prette J. J., Source localization following permanent transperineal prostate interstitial brachytherapy using magnetic resonance imaging, *International Journal of Radiation Oncology, Biology, Physics*, 39(5), 1037-1041 (1997) p: 11, 57

Dubois D. F., Prestidge B. R., Hotchkiss L. A., Prette J. J., Bice W. S., Intraobserver and interobserver variability of MR-imaging and CT-derived prostate volumes after transperineal interstitial permanent prostate brachytherapy, *Radiology*, 207, 785-789 (1998) p: 11, 57, 120

Fitzpatrick J. M., West J., Maurer C. Jr., Predicting error in rigid-body, point-based registration, *IEEE Transactions on Medical Imaging*, 17(5), 694-702 (1998) p: 31

Hajnal J. V., Hill D. L. G., Hawkes D. J., "Medical Image Registration" CRC Press, New York, (2001) p: 11, 12, 15,16, 17, 20

Heintz B. H., Wallace R. E., Havezi J. M., Comparison of I-125 sources used for permanent interstitial implants, *Medical Physics*, 28(4), 671-682 (2001) p: 7

ICRU, ICRU Report 38: Dose and volume specification for reporting intracavitary therapy in gynecology, 1985 p: 6

Kagawa K., Lee R. W., Schultheiss T. E., Hunt M. A., Shaer A. H., Hanks G. E., Initial clinical assessment of CT-MRI image fusion software in localization of the prostate for 3D conformal radiation therapy, *International Journal of Radiation Oncology, Biology, Physics*, 38(2), 319-325 (1997) p: 83

Khan F. M., "The Physics of Radiation Therapy" , Lippincott Williams & Wilkins, Philadelphia, (2003) p: 5, 6, 7, 8, 23

Kunos C. A., Resnick M. I., Kinsella T. J., Ellis R. J., Migration of implanted free radioactive seeds for adenocarcinoma of the prostate using a Mick applicator, *Brachytherapy*, 3(2), 71-77 (2004) p: 9

Lee W., Moughan J., Owen J., Zelefsky M., The 1999 patterns of care survey of radiation therapy in localized prostate cancer – A comprehensive survey of prostate brachytherapy in the United States, *International Journal of Radiation Oncology, Biology, Physics*, 57(2), S256 (2003) p: 6

Maintz J. B. A., Viergever M. A., A survey of medical imaging registration, *Medical Image Analysis*, 2(1), 1-36 (1998) p: 12, 13

McLaughlin P. W., Narayana V., Kessler M., McShan D., Troyer S., Marsh L., Hixson G., Roberson P. L., The use of mutual information in registration of CT and MRI datasets post permanent implant, *Brachytherapy*, 3(2), 61-70 (2004) p: 83, 84, 99,102

Nag S., Bice W., DeWyngaert K., Prestidge B., Stock R., Yu Y., The American Brachytherapy Society recommendations for permanent prostate brachytherapy postimplant dosimetric analysis, *International Journal of Radiation Oncology, Biology, Physics*, 46(1), 221-230 (2000) p: 10, 11, 48

Parker C. C., Damyanovich A., Haycocks T., Haider M., Bayley A., Catton C. N., Magnetic resonance imaging in the radiation treatment planning of localized prostate cancer using intra-prostatic fiducial markers for computed tomography co-registration, *Radiotherapy and Oncology*, 66(2), 217-224 (2003) p: 84

Peschel R. E., Colberg J. W., Surgery, brachytherapy, and external-beam radiotherapy for early prostate cancer, *The Lancet Oncology*, 4(4), 233-241 (2003) p: 8

Pluim J. P. W., Maintz J. B. A., Viergever M. A., Mutual-information-based registration of medical images: a survey, *IEEE Transactions on Medical Imaging*, 22(8), 986-1004 (2003) p: 18, 19, 21, 35

Ragde H., Korb L. J., Elgamal A. A., Grado G. L., Nadir B.S., Modern prostate brachytherapy. Prostate specific antigen results in 219 patients with up to 12 years of observed follow-up, *Cancer*, 89(1), 135-141 (2000) p: 8

Roberson P. L., McLaughlin P. W., Troyer S., Hixson G. V., Kessler M. L., Use and uncertainties of mutual information for computed tomography / magnetic resonance (CT/MR) registration post permanent implant of the prostate, *Medical Physics*, 32(2), 473-482 (2005) p: 83, 84, 99

Roy J. N., Wallner K. E., Harrington P. J., Ling C. C., Anderson L. L., A CT-based evaluation method for permanent implants: application to prostate, *International Journal of Radiation Oncology, Biology, Physics*, 26(1), 163-169 (1993) p: 10

Seeram E., "Computed Tomography, physical principles, clinical applications and quality control", 2nd ed., W. B. Saunders Company, Philadelphia, (2001) p: 49

Servois V., Chauveinc L., El Khoury C., Lantoine A., Ollivier L., Flam T., Rosenwald J. C., Cosset J. M., Neuenschwander S., CT and MR image fusion using two different methods after prostate brachytherapy: impact on post-implant dosimetric assessment, *Cancer Radiothérapie*, 7(1), 9-16 (2003) p: 83, 84

Stock R. G., Stone N. N., Importance of post-implant dosimetry in permanent prostate brachytherapy, *European Urology*, 41(4), 434-439 (2002) p: 53

Stone N. N., Hong S., Lo Y., Howard V., Stock R. G., Comparison of intraoperative dosimetric implant representation with postimplant dosimetry in patients receiving prostate brachytherapy, *Brachytherapy*, 2(1), 17-25 (2003) p: 9

Studholme C., Hill D. L. G., Hawkes D. J., An overlap invariant entropy measure of 3D medical image alignment, *Pattern Recognition*, 32(1), 71-86 (1999) p: 19, 20, 21, 33, 34

Van Dyk J., "The Modern Technology of Radiation Oncology", Medical Physics Publishing, Madison, (1999) p: 4

Van Herk M., Bruce A., Kroes G. A. P., Shouman T., Touw A., Lebesque J. V., Quantification of organ motion during conformal radiotherapy of the prostate by three dimensional image registration, *International Journal of Radiation Oncology, Biology, Physics*, 33(5), 1311-1320 (1995) p: 84,102

Woods R. P., Mazziotta J. C., Cherry S. R., MRI-PET registration with automated algorithm, *Journal of Computer Assisted Tomography*, 17(4), 536-546 (1993) p: 18

Yu Y., Anderson L. L., Zuofeng L., Mellenberg D. E., Nath R., Schell M. C., Waterman F. M., Wu A., Blasko J. C., Permanent prostate seed implant brachytherapy: Report of the American Association of Physicists in Medicine Task Group No. 64, *Medical Physics*, 26(10), 2054-2073 (1999) p: 7, 10, 48, 51

